Journal of Electronic Materials (2025) 54:5087–5129
https://doi.org/10.1007/s11664-025-11756-3

TOPICAL COLLECTION: FRONTIERS IN MATERIALS SCIENCE 2024

Ferroelectric and Multiferroic Properties of Quasi-2D Organic Charge-Transfer Salts: A Review

Michael Lang[1] · Peter Lunkenheimer[2] · Owen Ganter[3] · Stephen Winter[3] · Jens Müller[1]

Received: 28 August 2024 / Accepted: 8 January 2025 / Published online: 2 April 2025

Abstract

In conventional ferroelectrics, the electric dipoles are generated by off-center displacements of ions or by the ordering of dipolar molecular units. In recent years, a new type of so-called electronic ferroelectrics has attracted great attention, where the polarization is driven by electronic degrees of freedom. Of particular interest are materials with strong electronic correlations, featuring a variety of intriguing phenomena and instabilities, which may interact with or even induce electronic ferroelectricity. In this review, we will focus on the class of strongly correlated charge-transfer salts, where electronic ferroelectricity was suggested by theory and has been confirmed by numerous experiments. The paper summarizes some basic physical properties of various relevant quasi-two-dimensional salts and gives some background on the experimental tools applied to establish ferroelectricity. We discuss the key experimental observations, including the exciting discovery of multiferroicity, and provide some theoretical considerations on the magnetoelectric couplings that are of relevance here.

Keywords Ferroelectricity · organic ferroelectricity · molecular solids · strongly correlated electrons · dielectric properties · fluctuation spectroscopy · multiferroicity · charge order

Introduction

Organic charge-transfer salts continue to be the subject of intensive investigations due to their rich phenomenology resulting from reduced dimensions and the combined effects of strong electron–electron and electron–phonon interactions in the presence of geometrical frustration.[1–5]

In addition, particular types of ferroelectricity, and even multiferroicity, have been theoretically predicted[6,7] and experimentally observed.[8] Here, the ferroelectric polar order is generated by electronic degrees of freedom in contrast to the off-center displacement of ions or the orientational ordering of dipolar molecular units in conventional ferroelectrics. Thus, organic charge-transfer salts represent prime examples of so-called electronic ferroelectrics[7]—a novel type of ferroelectric material which was first proposed in 2005.[9] A spontaneous polarization originating from the polar ordering of electrons rather than ions implies unique characteristics such as low coercive fields, very high durability, and an ultrafast response. These special properties open up new routes for high-speed and low-energy technical applications (see, e.g., Ref. 10 for a recent review). The research activities related to the intriguing dielectric properties of charge-transfer salts, building on the discovery of charge-order-driven ferroelectricity in the quasi-1D Fabre salts[11,12] in 2000, have gained momentum in recent years, as clear signatures for electronic ferroelectricity and even multiferroicity have been reported for various families of the quasi-two-dimensional (2D) charge-transfer salts. While we will briefly touch on the important early findings in the quasi-1D systems, the focus of our paper will be on the more recent

✉ Jens Müller
j.mueller@physik.uni-frankfurt.de

Michael Lang
michael.lang@physik.uni-frankfurt.de

[1] Institute of Physics, Goethe University Frankfurt, 60438 Frankfurt, Germany

[2] Experimental Physics V, Center for Electronic Correlations and Magnetism, University of Augsburg, 86159 Augsburg, Germany

[3] Department of Physics and Center for Functional Materials, Wake Forest University, Winston-Salem, NC 27109, USA

developments in the field of quasi-2D systems. Some aspects of electronic ferroelectricity for organic charge-transfer salts have been addressed in previous review articles.[13–16] See also Refs. 17–21 for recent reports of electronic ferroelectricity in inorganic materials and molecular metal complexes.

The paper is organized as follows. In "Quasi-1D and Quasi-2D Charge-Transfer Salts" section we summarize some basic properties of the relevant families of organic charge-transfer salts including their lattice and electronic structures, and give some theoretical considerations on the materials' symmetry and their magentoelectric coupling and phase diagrams. In "Experimental Techniques" section we provide a brief introduction into the experimental techniques used to probe the dielectric properties and to investigate the involvement of other degrees of freedom. Priority is given to the techniques employed in the authors' own investigations. In "Signatures of Ferroelectricity Revealed in Quasi-1D and Quasi-2D Systems" section we recall the rich variety of dielectric phenomena observed in the quasi-one-dimensional (1D) and quasi-2D salts. The experimental results on the κ-phase salts are discussed in more detail in Sect. "Beyond the Dimer-Mott Limit: The Case of κ-phase (BEDT-TTF)$_2X$" section with regard to the role of intra-dimer degrees of freedom and the nature of relaxor-type ferroelectricity. A short summary is given in "Epilogue" section.

Quasi-1D and Quasi-2D Charge-Transfer Salts

Crystallographic and Electronic Structure

Evidence for electronic ferroelectricity in organic charge-transfer (CT) salts was first observed in the family of the quasi-1D conductors (TMTTF)$_2X$,[12] where TMTTF stands for tetramethyltetrathiafulvalene and X for a monovalent anion. In these salts, planar organic molecules are stacked along the a axis, for which the intermolecular overlap of π orbitals is strongest (see Fig. 1), thus forming a quasi-1D band structure. Due to a dimerization, the strength of which depends on the anion X, there is one hole per dimer. Upon cooling to below $T_{CO} \sim$ 50–150 K, charge ordering sets in, where the TMTTF molecules within the dimer become nonequivalent. The charge disproportionation below T_{CO} and the accompanying loss of inversion symmetry are key for the formation of polar order in this family of CT salts.

Subsequently, electronic ferroelectricity has also been found in 2D salts of BEDT-TTF and BETS, where BEDT-TTF (or simply ET) stands for bis(ethylenedithio)tetrathiafulvalene, while BETS stands for bis(ethylenedithio)tetraselenafulvalene. In the BETS molecule, the four S atoms

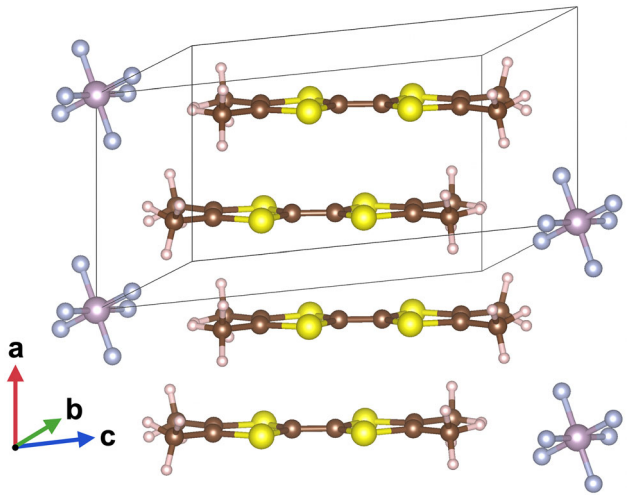

Fig. 1 Crystal structure of (TMTTF)$_2$PF$_6$ viewed from a somewhat tilted angle relative to the b direction. The TMTTF molecules pile up along the a direction, the axis of highest conductivity.

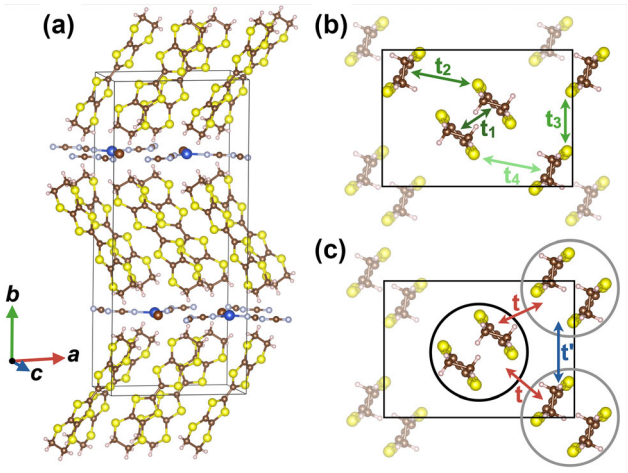

Fig. 2 (a) Crystal structure of κ-(ET)$_2X$ with thick layers of ET molecules separated by thin sheets of inorganic anions X. (b) Closer look on the ET layer viewed along the molecules' long axes, with $t_{1,2,3,4}$ referring to the hopping parameters between the highest occupied molecular orbitals. (c) For strong intra-dimer hopping t_1, pairs of ET molecules form a dimer (circles), arranged on an anisotropic triangular lattice with hopping terms t and t'.

in the inner TTF skeleton are replaced by Se. Prominent examples of this type of electron-driven ferroelectricity include some κ-(ET)$_2X$ salts (Fig. 2) as well as some θ-phase variants (see Fig. 3a for a cartoon of the various relevant (ET)$_2X$ polymorphs).

The κ-phase constitutes the most intensively studied class of (ET)$_2X$ salts due to its model character for exploring the behavior of correlated electrons in reduced dimensions. A plethora of intriguing phenomena have been reported, including the Mott metal-insulator transition[22–24] and its critical properties,[25–29] unconventional superconductivity,[3,5,30–32] strongly frustrated quantum

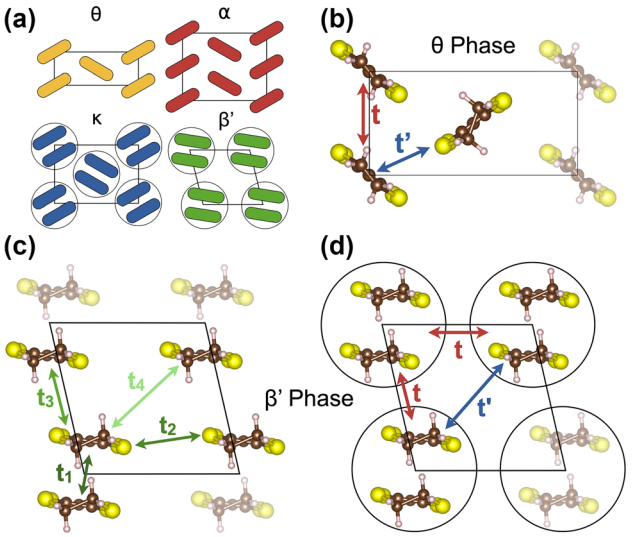

Fig. 3 (a) Cartoon depiction of four relevant polymorphs. (b) ET layer for θ-phase packing showing in-stack interaction t and out-of-stack interaction t'. (c) ET layer for β'-phase packing with intermolecular hopping integrals labeled t_{1-4}. (d) inter-dimer hopping integrals labeled as t and t'.

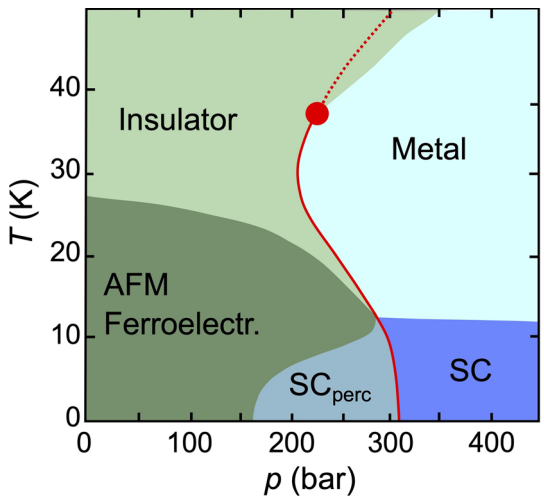

Fig. 4 Temperature–pressure phase diagram of κ-$(ET)_2Cu[N(CN)_2]Cl$. At ambient and small pressure, the system shows antiferromagnetic (AFM) order accompanied by ferroelectric order. The evolution of the ferroelectric order under pressure has not yet been investigated. With increasing pressure, the system undergoes a first-order Mott metal insulator transition (red solid line) which terminates in a second-order critical endpoint (red sphere). On the high-pressure side of the Mott transition, superconductivity (SC) occurs. Figure adapted from Ref. 15, under the terms of the Creative Commons CC BY license (Color figure online).

magnetism,[3,33–35] and ferroelectricity[36] as well as multiferroicity.[8] Figure 4 shows a temperature–pressure phase diagram for κ-$(ET)_2Cu[N(CN)_2]Cl$ (κ-Cl), highlighting a rich phenomenology by pressure-tuning the system across the Mott metal-insulator transition. At ambient pressure (p = 0), this system is a Mott insulator which orders

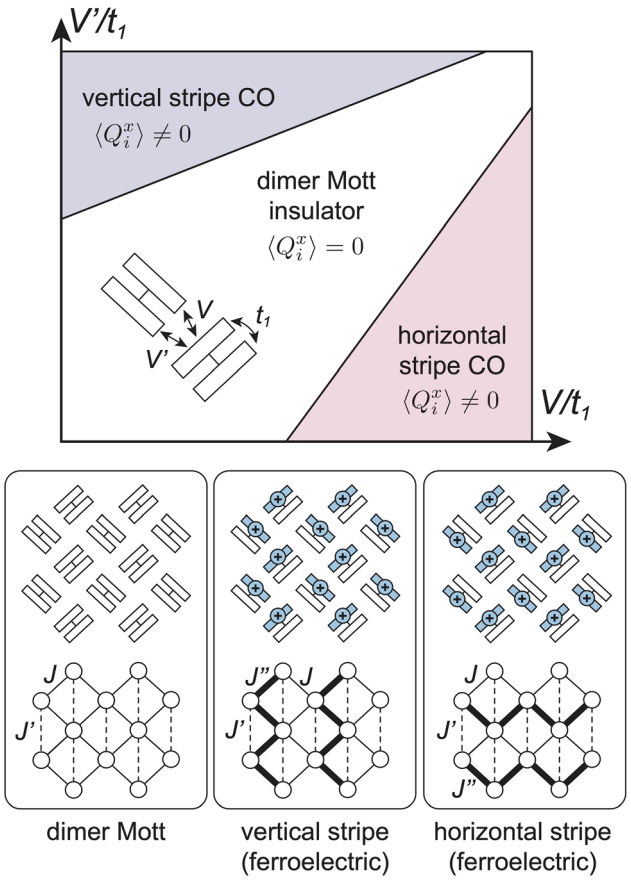

Fig. 5 Schematic phase diagram for κ-phase ET materials as a function of inter-dimer Coulomb repulsion V and V'. For detailed studies, see, e.g., Refs. 51–54. Local spin moments are associated with the sites having excess holes, indicated in light blue. Charge order alters the effective magnetic couplings between dimers, breaking the symmetry between different J-bonds (Color figure online).

antiferromagnetically below T_N = 27 K.[37]. Upon cooling, the magnetically ordered state was found to be accompanied by ferroelectric order,[8] making this system multiferroic, with $T_{FE} \approx T_N$ suggesting an intimate interrelation between the two types of ordering. By the application of moderate pressure of only 300 bar, the system undergoes a first-order Mott transition.[22–24,38] This first-order line terminates in a second-order critical endpoint at $(T_{Cr}, p_{Cr}) \approx$ (36.5 K, 234 bar).[25–29,39] On the metallic side of the Mott transition, superconductivity (SC) is observed below $T_c \approx$ 12 K.

In these κ-phase salts, the most common mode of charge order (CO) is intra-dimer charge disproportionation, pictured in Fig. 5. The propensity for this mode of CO can be considered as a competition between dimerization strength and inter-dimer Coulomb repulsion. By symmetry, there are four distinct hopping parameters $t_{1,2,3,4}$ (cf. Fig. 2b). For strong intra-dimer hopping t_1, the systems can be modeled by an effective-dimer model (Fig. 2c)

Table I Model parameters for relevant κ- and β'-type organic charge-transfer salts

Material	T	Ref	t_1	t_2	t_3	t_4	t	t'	$\lvert t'/t\rvert$	$\lvert t_1/t'\rvert$
κ-$(ET)_2Cu[N(CN)_2]Cl$	15	40	207	102	67	43	73	34	0.46	6.2
κ-$(ET)_2Cu_2(CN)_3$	293	41	176	78.0	81.4	18.7	48.4	40.7	0.84	4.3
κ-$(ET)_2Hg(SCN)_2Cl$	296	42	126.6	60.0	80.8	42.0	51.0	40.4	0.79	3.1
κ-$(BETS)_2Mn[N(CN)_2]_3$	RT	43	177	8	125	63	36	63	1.76	2.8
β'-$(ET)_2ICl_2$	12	40	251	−22	−36	102	40	−18	0.45	13.9

characterized by only two hopping terms t and t' given by $t = (t_2 + t_4)/2$ and $t' = t_3/2$.[44,45] In this limit, the materials can be viewed as effectively half-filled, with one electron per dimer occupying the anti-bonding combination of molecular orbitals, and shared equally between the two molecules. The appearance of intra-dimer CO represents a departure from this pure dimer-Mott limit. Table I summarizes the hopping parameters for κ-$(ET)_2Cu[N(CN)_2]Cl$ and related κ-phase salts. The strength of dimerization (and therefore the propensity to form intra-dimer CO) can be evaluated from the $|t_1/t|$ and $|t_1/t'|$. In general, κ-$(ET)_2Cu[N(CN)_2]Cl$ has relatively strong dimerization (quantified by a large value of t_1), while κ-$(ET)_2Hg(SCN)_2Cl$ has the weakest dimerization. The theoretical consequences for CO are reviewed in detail in "Theoretical Phase Diagrams" section.

The θ-phase (pictured in Fig. 3b) is the second crystallographic phase where ferroelectricity is prominently observed in 2D CT salts. In this case, the ET molecules form undimerized π-stacks, which occupy an anisotropic triangular lattice defined by two hopping integrals: t and t'. With one hole per two organic molecules, these are viewed as three-quarters-filled, and exhibit a variety of CO patterns resulting largely from the balance of inter-molecular Coulomb repulsion terms. The phase diagram is discussed in more detail in "Theoretical Phase Diagrams" section.

Finally, we also address the structure of compounds in the α- and β'-phases, discussed in "Signatures of Ferroelectricity Revealed in Quasi-1D and Quasi-2D Systems" section. The orientation of the organic molecules in these phases is shown schematically in Fig. 3a. The α-phase can be viewed as a variant of the θ-phase, in which the unit cell is doubled along the π-stacking direction, and half of the π-stacks are weakly dimerized. The phenomenology of α- and θ-phase materials is similar, and the two may be discussed together. The β'-phase materials exhibit moderate to strong dimerization analogous to the κ-phase, but dimers stack in a uniform fashion rather than a herringbone pattern, as shown in Fig. 3c and d. An example compound, discussed in "Quasi-2D β′-$(BEDT\text{-}TTF)_2ICl_2$" section, is β'-$(ET)_2ICl_2$, which exhibits strong dimerization ($|t_1/t'| \sim 14$). Similar to the κ-phase materials, the primary mode of CO is intra-dimer charge disproportionation, which competes with dimerization (see "Theoretical Phase Diagrams" section).

Symmetry Considerations for Ferroelectricity and Multiferroicity

Magnetic and polar charge orders can be discussed in terms of their corresponding order parameters, and the free energy governing their evolution. The form of this free energy is restricted by crystal symmetries.

The vast majority of organic CT salts are centrosymmetric in their paraelectric states, including the above-mentioned κ- and θ-phases. Magnetic order parameters M (both antiferromagnetic and ferromagnetic) are odd with respect to time reversal, while ferroelectric polarization P is even with respect to time reversal and odd with respect to inversion. For this reason, the free energy is restricted to the form $\mathcal{F} = aP^2 + bM^2 + cP^2M^2 + \cdots$[46–48] for temperature-dependent constants a, b, c, ... Since M and P represent symmetry-distinct order parameters, they are forbidden from coupling linearly, such that ordering of electric and magnetic dipoles typically occurs at distinct temperatures. This is true unless (i) the magnetoelectric coupling is weak, and the natural magnetic and charge-order transitions accidentally coincide, or (ii) the magnetoelectric coupling c is sufficiently negative as to merge the two into a single first-order transition.

The character of the magnetoelectric coupling depends on the microscopic details and the nature of the electronic and magnetic order parameters. For example, as detailed in "Dielectric Spectroscopy" section, it has been suggested that ferroelectric ordering of the intra-dimer dipole moments couples "attractively" ($c < 0$) to collinear two-sublattice antiferromagnetic order in κ-$(ET)_2Cu[N(CN)_2]Cl$,[8,49] due to relief of magnetic frustration with weak CO. In this case, since the antiferromagnetic order preserves inversion and translation symmetries, a weak ferromagnetic moment appears as a consequence of Dzyaloshinskii–Moriya interactions. κ-$(ET)_2Cu[N(CN)_2]Cl$ has thus been identified as a rare organic multiferroic, in which electronic and magnetic order parameters are mutually conducive. In contrast, κ-$(ET)_2Hg(SCN)_2Cl$ exhibits an apparent re-entrant charge liquid state[50] in which CO initially sets in at $T_{CO} \approx 30$ K but

subsequently melts below 10 K, recovering a paraelectric state. This has been discussed in terms of "repulsion" ($c > 0$) between CO and three-sublattice 120° magnetic order, which was previously anticipated theoretically.[51] In this view, the appearance of strong magnetic correlations suppresses CO. As discussed in the following sections, electronic CO tends to reduce the dimensionality of the magnetic couplings, resulting in an incompatibility of magnetic order with CO. These findings highlight the subtleties of magnetoelectric coupling, which can give rise to a variety of scenarios in which the magnetic and electric properties are coupled.

Theoretical Phase Diagrams

κ-phase The phase diagrams of κ-phase materials in regard to CO has been explored theoretically by various approaches including mean-field theory[51] and variational Monte Carlo.[52–54] As discussed in the previous sections, the most common mode of CO in κ-phase materials is intra-dimer charge disproportionation, in which one hole occupies each dimer, but the charge is unequally distributed across the two ET molecules. Similar considerations apply to the β'-phase, although the latter has not been studied in as much detail theoretically. Inter-dimer CO modes for κ-phase have been explored theoretically,[52,53] but do not appear in known materials, aside from catachol-based materials where proton dynamics strongly influence the CO patterns.[55] A range of theoretical studies[51,56–59] therefore adopt a pseudospin parameter $\mathbf{Q}_i$ to represent the charge degree of freedom of dimer i. $\langle Q_i^z \rangle = +1/2$ implies an equal charge distribution, in which the hole occupies the antibonding combination of ET molecular orbitals. $\langle Q_i^x \rangle = \pm 1/2$ implies complete localization of the hole to one molecule or the other (see Ref. 51). The most important terms in the coupled magnetoelectric Hamiltonian can then be written as[51,58–60]

$$\mathcal{H} = \sum_{\langle ij \rangle} J_{ij} \mathbf{S}_i \cdot \mathbf{S}_j - \Gamma \sum_i Q_i^z + \sum_{\langle ij \rangle} W_{ij} Q_i^x Q_j^x + \sum_{\langle ij \rangle} K_{ij} (Q_i^x - Q_j^x) \mathbf{S}_i \cdot \mathbf{S}_j \quad , \tag{1}$$

where J_{ij} is the bare antiferromagnetic coupling between spins in adjacent dimers; Γ is proportional to the intra-dimer hopping (denoted by t_1 in Fig. 5), and represents the energetic preference for the hole to delocalize across both molecules; W_{ij} describes the interaction of dipoles on different dimers, mostly due to Coulomb repulsion between electrons occupying molecules in adjacent dimers (denoted by V, V' in Fig. 5); and finally, K_{ij} describes the modulation of the inter-site magnetic couplings as a function of charge distribution. The sign of the coupling is such that the magnetic interaction between two holes is increased with increasing localization of those holes to near sides of their respective dimers. An extensive discussion of magnetoelectric couplings for κ-$(ET)_2X$ materials and their *ab initio* estimation can be found in Ref. 59.

In the context of CO patterns, the fate of the electric dipole moments is largely controlled by the transverse field Ising model defined by Γ and W_{ij}. The schematic phase diagram, derived from various studies, is depicted in Fig. 5. This model has three phases. The first is a dimer-Mott phase with no charge disproportionation ($\langle Q_i^x \rangle = 0$), which is favored at large $\Gamma \approx t_1$. The second and third phases are charge-ordered ferroelectric states ($\langle Q_i^x \rangle \neq 0$), favored at large $W_{ij} \sim V$.[56,57] The preferred orientation of the net dipole moment and pattern of CO (vertical vs. horizontal stripes) is determined by the specific details of inter-dimer Coulomb repulsion. The quantum critical point separating the CO and dimer-Mott phases is expected to be associated with enhanced relaxor-type dielectric susceptibility,[61] discussed in more detail in "Dielectric Response of Ferroelectrics" section. The CO breaks the symmetry of the magnetic interactions, weakening the J' coupling and one of the J couplings, while enhancing the second J coupling. As a consequence, the magnetic interactions become increasingly one-dimensional with increasing CO.

For weak CO, the enhancement of magnetic couplings along one axis of the crystal is compatible with the collinear Néel order observed in κ-$(ET)_2Cu[N(CN)_2]Cl$. For stronger CO, the increasingly one-dimensional magnetic interactions may instead suppress magnetic order. This has been considered as a scenario for κ-$(ET)_2Hg(SCN)_2X$ (X = Cl, Br),[36] where no sign of magnetic order is detected, yet the majority of spins are strongly antiferromagnetically coupled below T_{CO}. In these materials, defects in the charge-ordering pattern (domain walls) likely host quasi-free orphan spins, giving rise to a weak inhomogeneous paramagnetic response below T_{CO}, which is observed in nuclear magnetic resonance (NMR),[62–64] electron spin resonance (ESR),[65] and magnetic susceptibility/torque.[66,67] These effects may be enhanced by intrinsic glassiness of the CO.[68]

θ-phase For the undimerized θ-phase materials, the interplay between spin and charge degrees of freedom is comparatively less explored. The phase diagram as a function of intermolecular hopping and Coulomb repulsion has been addressed via a range of theoretical methods, including mean-field theory,[69,70] slave-boson approaches,[71] random phase approximation,[72] variational Monte Carlo,[73] exact diagonalization,[74] and density matrix renormalization group.[75] The α-phase materials (such as α-$(ET)_2I_3$) can be viewed as slightly modulated versions of θ-phase materials, with analogous modes of CO.

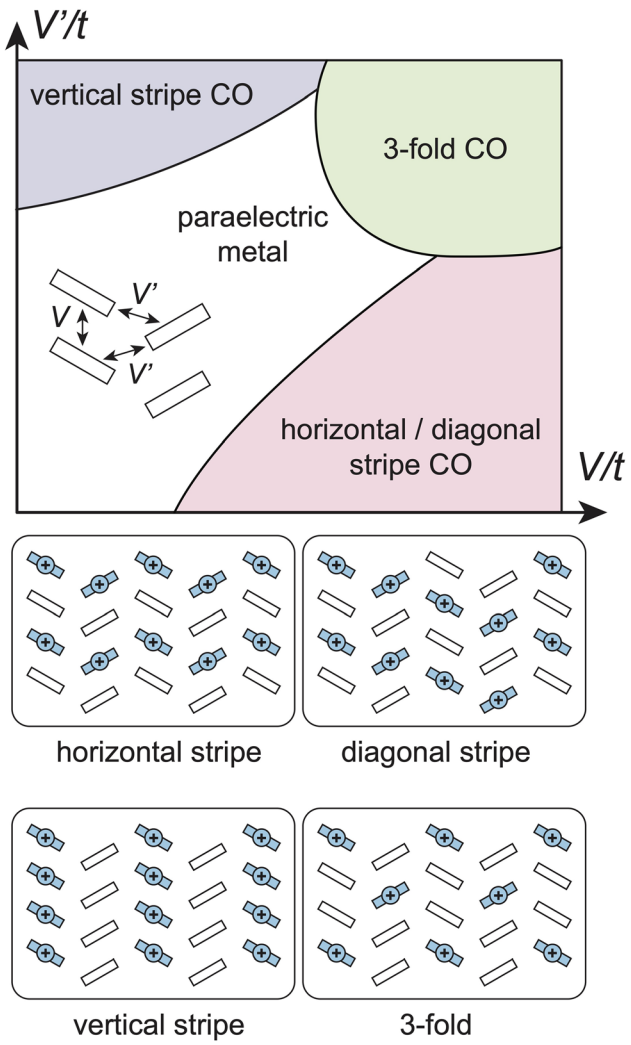

Fig. 6 Schematic phase diagram for θ-phase ET materials as a function of nearest-neighbor Coulomb repulsion V (within a π-stack) and V' (between π-stacks). For detailed studies, see, e.g., Refs. 69, 70, 73, and 75. Local spin moments are associated with the sites having excess holes, indicated in light blue (Color figure online).

With the inclusion of short-range (nearest neighbor) repulsion, the phase diagram features three prominent CO patterns, with (i) vertical charge stripes, (ii) diagonal/horizontal charge stripes, and (iii) a threefold pattern in which excess holes are localized to one third of the sites in a triangular lattice pattern (depicted schematically in Fig. 6). The latter region hosts a "pinball liquid" state, which remains metallic in conjunction with CO[76–78] due to the itineracy of the electrons associated with the electron-rich sites. The relative stability of the various phases can also be influenced by the details of electron-lattice coupling,[79–81] as the susceptibility of the crystal to local structural distortions coinciding with CO can play a role. The phase diagram becomes somewhat more complicated with consideration of longer-range Coulomb repulsion, which can stabilize CO patterns with longer period,[82,83] composed of mixed domains of diagonal, horizontal, and vertical stripes. This complex energy landscape is ultimately conducive to glassy charge dynamics,[84–87] which provides theoretical intuition for the properties of θ-$(ET)_2MM'(SCN)_4$ compounds, reviewed in "Quasi-2D β′-$(BEDT\text{-}TTF)_2ICl_2$" section.

Regarding the magnetic properties of θ-phase compounds, in the striped CO phases, mean-field studies find various magnetic orders coexisting with CO.[69,70] However, similar to the κ-phase materials, strong CO tends to result in magnetic connectivity that is low-dimensional: either 1D, in the case of perfect vertical or diagonal/horizontal stripes, or 0D when complicated (glassy) domain structures leads to many breaks in the spin chains. As a consequence, magnetic order tends to be suppressed by CO. For θ-$(ET)_2RbZn(SCN)_4$ (θ-RbZn) and θ-$(ET)_2CsZn(SCN)_4$ (θ-CsZn), magnetic susceptibility, ESR, and NMR have been employed to probe the magnetic response.[88–92] For $T < T_{CO}$, θ-RbZn forms a robust horizontal/diagonal CO pattern, in which the spins at the electron-poor sites form 1D chains. The susceptibility is well modeled by an antiferromagnetic Heisenberg chain[88] down to $T \sim 20$ K, at which point a spin gap opens, and the compound forms a singlet ground state. The precise nature of this singlet state is not completely settled, but it is thought to correspond to a spin-Peierls transition (with further distortion of the lattice). For θ-CsZn, the glassy charge state at low temperatures gives rise to an enhanced Curie tail in the magnetic susceptibility, and strongly inhomogeneous NMR relaxation. These effects can be understood analogously with the orphan-spin response in κ-$(ET)_2Hg(SCN)_2X$; due to the effective coupling of spins and charges, the homogeneity of the magnetic response is a direct probe of the homogeneity of the CO.

Experimental Techniques

In this chapter we briefly introduce some experimental techniques used to characterize the properties of the various CT salts. Preference is given to the methods applied by the authors' own investigations including, in particular, dielectric spectroscopy, fluctuation (noise) spectroscopy, and polarization measurements.

Dielectric Spectroscopy

Quantities and Experimental Methods

Dielectric spectroscopy measures the response of a material to alternating-current (AC) electric fields by recording

the real and imaginary parts of its dielectric permittivity, $\varepsilon^* = \varepsilon' - i\varepsilon''$ (the minus sign ensures that ε'' is positive), for varying frequencies of the applied field. The measurements are usually done for different temperatures, but other external parameters can also be varied, such as pressure or magnetic field. Dielectric spectroscopy simultaneously also provides information on the complex conductivity, $\sigma^* = \sigma' + i\sigma''$, which is related to the permittivity via $\sigma^* = i\varepsilon^*\varepsilon_0\omega$ (where ε_0 is the permittivity of free space and ω the circular frequency), resulting in $\sigma' = \varepsilon''\varepsilon_0\omega$ and $\sigma'' = \varepsilon'\varepsilon_0\omega$. In general, ferroelectric transitions lead to an anomaly in the temperature dependence of the dielectric constant, $\varepsilon'(T)$. Depending on the type of the ferroelectric state of a material, characteristic differences in $\varepsilon'(T)$, but also in the frequency dependence of this quantity, are found. The dielectric loss, $\varepsilon''(T, \nu)$, mainly provides information on relaxational processes arising from dipolar dynamics, a characteristic property of some classes of ferroelectric materials as will be explained below. The real part of the conductivity σ' in principle provides the same information as ε''. However, it is better suited for analyzing charge-transport contributions in the material as found in many organic CT salts. For example, plain direct-current (DC) conductivity leads to a frequency-independent contribution in $\sigma'(\nu)$ and hopping conductivity to a ν^s power law with $s < 1$.[13,93–95]

In standard dielectric-spectroscopy experiments, usually covering frequencies in the hertz–megahertz range, commercially available autobalance bridges or frequency-response analyzers are employed. They require the application of two metallic contacts to the samples, from which two or four wires (i.e., two attached to each contact) establish the electrical connection to the device. For dielectric spectroscopy at higher frequencies, from megahertz up to several tens of gigahertz, various experimental methods exist.[96–101] Among them, coaxial reflectometry is most commonly applied: There, an electromagnetic wave traveling along a coaxial line is reflected by the sample at the end of the line. A network or impedance analyzer at the other end of the line measures either the complex reflection coefficient or the voltage–current ratio, from which the complex capacitance and the admittance (the complex conductance) can be calculated. Using the sample dimensions (length and cross-section area), from these quantities then the permittivity and conductivity can be derived.[94,99] For this method, two metallic contacts have to be applied to the sample as well. At frequencies beyond about 50 GHz, methods analogous to optical experiments are typically used, with the electromagnetic wave propagating through free space. In the present work, such experiments are not discussed.

Contact Preparation and Electrode Effects

The metallic contacts at the samples, which are required for dielectric measurements from the lowest frequencies up to several tens of gigahertz, can be produced by sputtering, evaporation, or by applying conductive suspensions such as graphite, silver, or gold paints and pastes. When suspensions are used, one has to ensure that their solvent does not affect the sample material. This is especially relevant for the organic systems treated in the present work. In experiments performed in the Augsburg laboratory on various organic CT salts,[8,13,102–105] graphite paint with diethyl succinate solvent or gold paint with propylene glycol methyl ether was found to be suitable for contact preparation, avoiding any sample deterioration. Quasi-2D materials, as predominantly discussed in the present work, often form single crystals of platelike shape. Covering the opposite sides of such crystals with the contact material leads to a parallel-plate capacitor with well-defined geometry and field distribution. The electric field then is oriented perpendicular to the lattice planes. To achieve a field direction parallel to the planes, coplanar contacts can be applied, however, leading to ill-defined field distribution, which is partly also oriented perpendicular to the planes, resulting in some uncertainty concerning the absolute values of the permittivity and conductivity. As an alternative, cap-like contacts can be applied, "wrapping" opposite ends of the sample, thereby ensuring that the electrical current is flowing parallel to the planes, across the whole cross section of the sample.

It should be noted that ferroelectrics either are highly insulating or at least have rather low conductivity (otherwise, the polarization would be shielded by the conduction electrons). Thus, the conductivity of the employed metallic contact material can be neglected in light of the much higher sample resistance, and it is irrelevant whether graphite, silver, gold, or any other metal is used. However, especially for semiconducting samples, including various organic CT salts, at the contact–sample interface, insulating depletion zones can develop due to the formation of Schottky diodes.[95,106] This can affect the measured dielectric sample response considerably, leading to non-intrinsic frequency dependencies, and care has to be taken to avoid any misinterpretation of the detected effects. Measurements of samples of different thickness and/or using different contact materials can help to resolve such problems.[95] Moreover, an analysis of the experimental data in terms of equivalent circuits has proven very useful for the deconvolution of the intrinsic and non-intrinsic contributions to the dielectric spectra.[93,95,106] An elaborate example of such an analysis, performed for an organic CT salt revealing relaxor ferroelectricity, can be found in the Supplementary Information of Ref. 107.

Dielectric Response of Ferroelectrics

There are three main classes of ferroelectric order: displacive, order–disorder, and relaxor ferroelectricity. In the following, we give a brief overview of their main properties, by concentrating on their dielectric response. In fact, dielectric spectroscopy is best suited for assigning a material to one of these classes because each of them is characterized by specific frequency- and temperature-dependent dielectric properties. Moreover, in order–disorder and relaxor ferroelectrics, valuable information about the dynamics of the dipolar entities involved in the ferroelectric ordering can be obtained. It should be noted, however, that dielectric spectroscopy alone is insufficient to definitely prove whether a material is ferroelectric, because the definition of ferroelectricity also includes the switchability of the polarization,[108] not tested by this method. For further details, we refer the reader to Refs. 13 and 108–112. In displacive systems, above their ferroelectric phase transition no permanent dipole moments exist. Below the transition, the materials cross over into a structure with reduced symmetry, where (in the most common cases) local shifts of ions to an off-symmetry position give rise to permanent dipoles, revealing long-range polar order. Displacive ferroelectrics are expected to exhibit a well-defined peak in the temperature dependence of the dielectric constant at their phase transition temperature T_{FE}. At the high-temperature flank of this peak, their $\varepsilon'(T)$ should follow a Curie–Weiss law, $\varepsilon' \propto 1/(T - T_{CW})$. Often the Curie–Weiss temperature T_{CW} is similar in size to T_{FE}. In the typical hertz–megahertz frequency range of standard dielectric experiments, the dielectric properties of displacive ferroelectrics usually show no or only weak frequency dependence. This $\varepsilon'(T, \nu)$ behavior is schematically indicated in Fig. 7a.[113] One should be aware that the exact peak shape depends on the character of the transition, i.e., whether it is of first order or second order, which implies considerable variations; the curve shown applies to a second-order transition. It should be noted that displacive ferroelectricity has only rarely been reported for organic CT salts.[114] An experimental example of an inorganic displacive ferroelectric is provided in Fig. 7e. It shows $\varepsilon'(T)$ of $LiCuVO_4$, a multiferroic whose polar order is driven by magnetic ordering, leading to ion displacement due to the inverse Dzyaloshinskii–Moriya interaction.[115] This is an improper ferroelectric where the order parameter driving the phase transition is not the polarization. As revealed in Fig. 7e, ε' of this material exhibits a sharp peak at $T_{FE} \approx 2.5$ K and only a weak frequency dependence as expected for displacive ferroelectrics.

While in displacive ferroelectrics the dipoles involved in the polar order are only formed below T_{FE}, in order–disorder ferroelectrics they already exist above the transition, but with dynamically disordered orientations.[108,111] Their alignment below T_{FE} then gives rise to ferroelectricity. Depending on the material, the dipoles can be due to charged particles (ions, electrons, holes), oscillating between two (or more) polar sites, or can be caused by dipolar molecules that rotate at $T > T_{FE}$ but order in a parallel fashion at $T < T_{FE}$. Figure 7b schematically depicts the temperature dependence of the dielectric constant found in this class of ferroelectrics for different frequencies.[113] As in displacive ferroelectrics, here a peak at the transition shows up as well, but it exhibits significant frequency dependence, leading to a gradual suppression of the peak with increasing frequency. The peak temperature usually weakly shifts to higher temperatures with increasing frequency. An analysis of the frequency dependence of ε' and ε'' indicates that the observed frequency dispersion is due to reorientational fluctuations of the dipoles within double- or multi-well potentials, leading to a so-called dielectric relaxation process.[118] From the dielectric spectra the relaxation time τ can be deduced, characterizing the dynamics of the dipoles. In order–disorder ferroelectrics, its temperature dependence $\tau(T)$ often follows a critical slowing down upon approaching the ferroelectric transition from high or low temperatures, instead of simple thermally activated Arrhenius behavior expected for dipoles not involved in polar ordering. Further analysis of the spectra reveals a nearly monodisperse, Debye-type nature of this dynamics, i.e., there is only a narrow distribution of relaxation times in these systems.[119] This is expected for well-ordered crystalline materials, in contrast to dipolar systems undergoing glassy freezing, where these distributions can be very broad.[118–120] An experimental example of $\varepsilon'(T, \nu)$ for order–disorder ferroelectricity in an organic CT salt is given in Fig. 7f.[8] In κ-$(ET)_2Cu[N(CN)_2]Cl$ (abbreviated κ-Cl in the figure), holes fluctuating within molecular dimers were proposed to give rise to dipolar moments, which order below the transition. A detailed discussion of these data will be provided in "Dielectric Spectroscopy" section.

Finally, Fig. 7c schematically shows the $\varepsilon'(T)$ behavior at different frequencies as typically measured for relaxor ferroelectrics.[109,110,113] The peculiar dielectric behavior of this class of ferroelectrics is usually assumed to arise from the glasslike freezing of cluster-like short-range ferroelectric order.[109,110] Again, a peak in $\varepsilon'(T)$ is observed, but compared to the other classes of ferroelectrics, it is smeared-out and the peak temperature is strongly frequency-dependent. The behavior in Fig. 7c in some respects resembles that of materials with dipolar reorientations that do not undergo dipole order upon cooling but instead exhibit glassy freezing, finally resulting in a low-temperature state with static orientational disorder. The $\varepsilon'(T)$ of such materials is schematically shown in

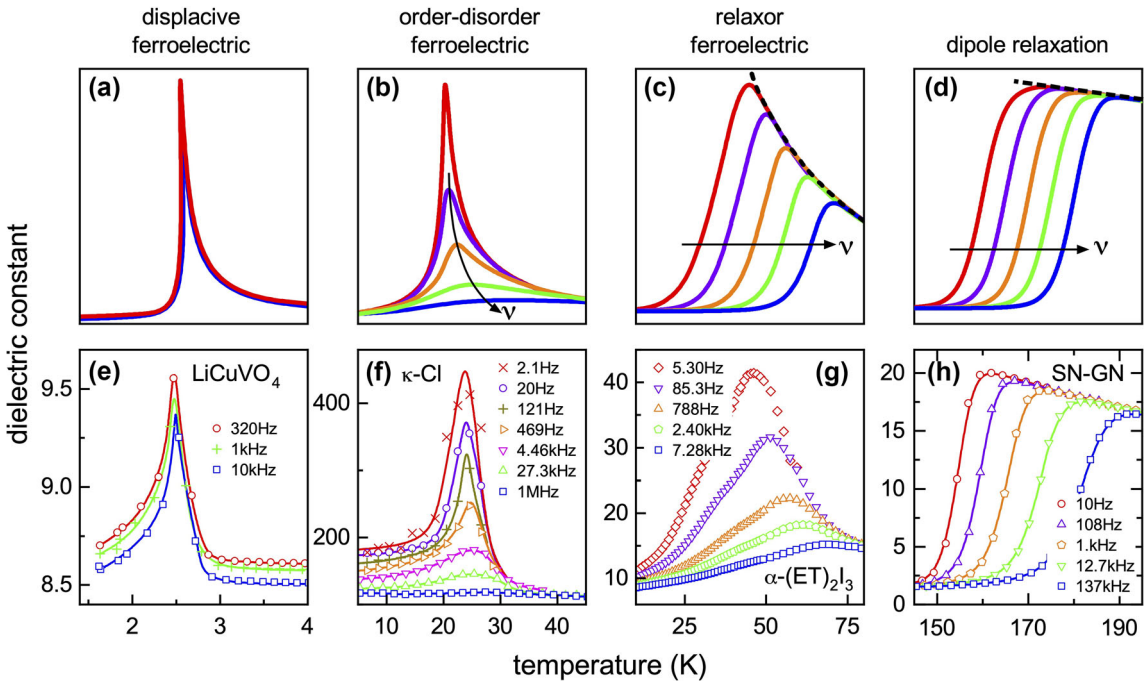

Fig. 7 (a)–(c) Schematic temperature dependence of the dielectric constant ε' for the three most common classes of ferroelectrics as measured at different frequencies. Frame (d) schematically shows $\varepsilon'(T)$ for a non-ferroelectric material with internal dipolar reorientational degrees of freedom, leading to a relaxation process. The main difference from $\varepsilon'(T)$ of a relaxor ferroelectric is revealed in the static dielectric constant $\varepsilon_s(T)$, indicated by the dashed lines in (c) and (d). Frames (e)–(h) show $\varepsilon'(T, \nu)$ of four materials representing experimental examples for the schematic plots in (a)–(d): (e) the inorganic multiferroic $LiCuVO_4$ (data from Ref. 115), (f) the quasi-2D organic multiferroic κ-$(ET)_2Cu[N(CN)_2]Cl$ (data from Ref. 8), (g) the quasi-2D organic relaxor-ferroelectric α-$(ET)_2I_3$ (data from Ref. 116), and (h) the plastic crystal SN-GN (the corresponding $\varepsilon'(\nu)$ spectra of this material were published in Ref. 117). The lines in (e), (f), and (h) are guides for the eye. Figure adapted with permission from Ref. 113.

Fig. 7d. It is revealed by many dipolar liquids undergoing a glass transition into an amorphous state[120] but also by certain crystalline systems, e.g., by plastic crystals, which are formed by dipolar molecules that can rotate even in the crystalline state.[121,122] An example of such a system is provided in Fig. 7h showing $\varepsilon'(T, \nu)$ of a mixture of 60% succinonitrile and 40% glutaronitrile (SN-GN) in its plastic-crystalline phase.[117] The main difference of relaxor ferroelectrics compared to such systems is the much stronger temperature dependence of their static dielectric constant ε_s as indicated by the dashed lines in Fig. 7c and d. For dipolar systems without order, a Curie law ($\varepsilon_s \propto 1/T$) is expected.[123] In relaxor ferroelectrics, this temperature dependence often (but not always) deviates from the typical Curie–Weiss behavior detected in canonical ferroelectrics. The strong increase of $\varepsilon_s(T)$ with decreasing temperature in relaxor ferroelectrics indicates increasing inter-dipolar correlations that lead to local polar order.

Analyzing the dielectric spectra of relaxor ferroelectrics often reveals deviations from monodisperse Debye behavior.[124] This points to disorder, leading to a distribution of relaxation times.[119] Indeed, relaxor ferroelectricity is often found in systems with substitutional disorder, a prominent example being the perovskite $PbMg_{1/3}Nb_{2/3}O_3$.[125] However, there are also nominally well-ordered materials for which relaxor ferroelectricity has been reported, including several organic CT salts.[102,103,116,126–128] The temperature dependence of the relaxation time $\tau(T)$ of relaxor ferroelectrics can usually be described[124,129–131] by the empirical Vogel–Fulcher–Tammann (VFT) law[132–134]:

$$\tau = \tau_0 \cdot \exp\left(\frac{B}{T - T_{VF}}\right). \quad (2)$$

Here, τ_0 is a pre-exponential factor, B is an empirical constant, and T_{VF} is the Vogel–Fulcher temperature where τ diverges. Instead of deriving the relaxation times from the spectra, for relaxor ferroelectrics, $\tau(T)$ is often approximated by evaluating the peak temperatures T_p in the $\varepsilon'(T)$ plots measured at different frequencies (Fig. 7c). Then, T in Eq. 2 is T_p, and τ is calculated from the measurement frequency ν of the evaluated $\varepsilon'(T)$ curve via $\tau = 1/(2\pi\nu)$. Notably, Eq. 2 is commonly applied to characterize the molecular dynamics in glass-forming liquids,[120,135,136] indicating that glassy freezing in some respects must play a role in relaxor ferroelectrics. Indeed, the latter are usually assumed to reveal the glasslike

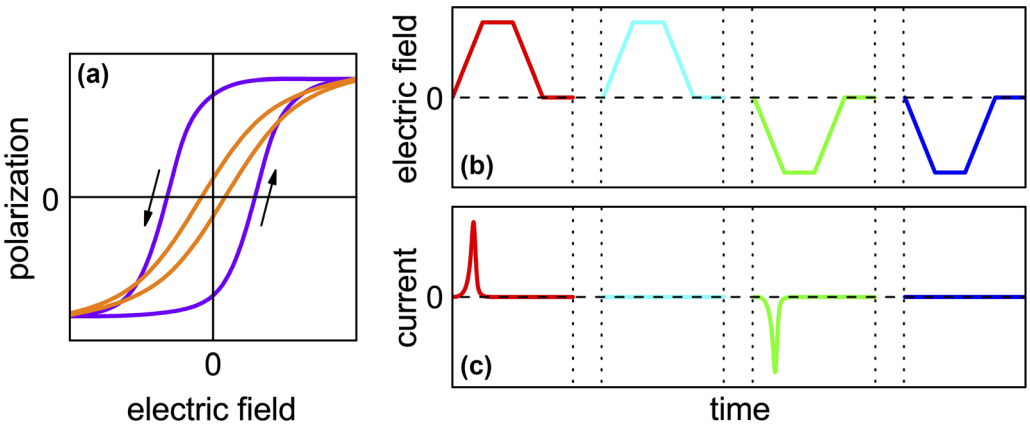

Fig. 8 (a) Examples of a wide and slim $P(E)$ hysteresis loop found in different ferroelectrics. Relaxor ferroelectrics exhibit slim loops. (b) Schematic plot of the time-dependent electric field as applied in typical positive-up/negative-down (PUND) measurements. (c) The current response to the field shown in (b) as expected for a ferroelectric. Figure adapted with permission from Ref. 113.

freezing-in of short-range, nanoscale ferroelectric order. In well-known relaxor ferroelectrics like $PbMg_{1/3}Nb_{2/3}O_3$ (PMN) or $Pb[Zr_xTi_{1-x}]O_3$ (PZT), ions are involved in the formation of the dipoles participating in this short-range order.[111] In contrast, the relaxor ferroelectricity reported for several CT salts is believed to be of predominantly electronic nature.[116,126,127] As an experimental example for the latter, Fig. 7g shows $\varepsilon'(T, \nu)$ of the organic CT salt α-$(ET)_2I_3$, which reveals the typical signature of relaxor ferroelectricity.[116] These data will be discussed in detail in "Quasi-2D α-$(BEDT\text{-}TTF)_2I_3$" section.

Polarization Measurements

A ferroelectric phase transition leads to the development of spontaneous electrical polarization P at $T < T_{FE}$. This can be investigated by measurements of P as a function of the electric field E, by so-called positive-up/negative-down (PUND) measurements and by pyrocurrent measurements. Strictly speaking, the definition of ferroelectricity not only involves the occurrence of spontaneous polarization below T_{FE} (signifying a pyroelectric material) but also requires that the polarization can be reversed by an external electric field.[108] This can be best checked by $P(E)$ or PUND measurements, while dielectric spectroscopy is better suited for gathering information about the type of the ferroelectric transition and the dipolar dynamics. Nowadays, various devices for such measurements are commercially available. In the Augsburg group, an aixACCT TF 2000 ferroelectric analyzer is used, partly in combination with a Trek 609C-6 amplifier. It allows for measurements of the time-dependent polarization in response to applied AC voltages up to 1.1 kV, with frequencies up to 1 kHz. As the applied voltages in such experiments are high, some care should be taken to avoid electrical breakthrough to metallic parts of the cryostat and sample holder, and the experiments should be performed under low pressure or in vacuum to prevent electric gas discharge.

For ferroelectrics, $P(E)$ measurements reveal typical hysteresis curves as schematically shown in Fig. 8a. Basically, they reflect the shift of polar domain walls, and the observed saturation at high fields indicates the approach of a mono-domain state. In principle, $P(E)$ measurements work best at temperatures somewhat below T_{FE}. At lower temperatures, the domains in ferroelectrics can be large, and the fields needed to induce domain-wall motions can be too high to avoid electrical breakdown.[108,111,137] However, many organic CT salts are semiconducting, and field-induced currents due to their enhanced DC conductivity at elevated temperatures can render the detection of hysteresis loops due to polarization-switching impossible. Therefore, in such systems the optimum temperature for such measurements has to be identified (usually by trial and error), but in some cases $P(E)$ measurements are simply not feasible. One should also be aware that non-intrinsic effects arising, e.g., from the above-mentioned depletion zones of Schottky diodes may lead to the erroneous detection of $P(E)$ hysteresis loops. This can be avoided by performing additional experimental checks.[138] Depending on the material, the width and saturation value of the loops can vary considerably. Relaxor ferroelectrics usually exhibit very slim hysteresis loops. Their small remanent polarization [detected at $E = 0$; cf. orange curve in Fig. 8a] implies that most polar nano-domains again become randomly oriented after switching off the field.[110]

For PUND measurements, a succession of time-dependent electric field pulses as schematically indicated in Fig. 8b is applied to the sample. Normally, such measurements can be done using the same state-of-the-art devices as for the $P(E)$ loops. If the field at the increasing flank of the first pulse becomes sufficiently high, polarization switching sets in, and the concomitant reorientation

of the electrical dipoles, involving the motion of charges, leads to a current-pulse which is detected by the device (Fig. 8c). If the time between the first and second pulse with the same field direction is sufficiently short to avoid a decay of the induced polarization, the current response to the second pulse should be featureless because all dipoles are already oriented. The third pulse with inverted field switches the polarization to the opposite direction, again leading to a current peak, while the fourth pulse does not trigger any current response. PUND measurements are an excellent way to distinguish between intrinsic and non-intrinsic polarization effects, as the latter should lead to identical current response for the first and second pulses as well as for the third and fourth ones.[137]

Pyrocurrent measurements also make use of the motion of charges associated with the reorientation of dipoles. In the most common form of these experiments, the sample is first brought close to a mono-domain polar state by cooling it to a temperature below T_{FE} while applying a high electric DC field. Afterwards, the sample is heated again through the transition without field. This leads to a pyrocurrent around T_{FE} when the dipoles reorient into disordered positions while crossing the transition. The polarization change at T_{FE} can be calculated by integrating the time-dependent current response. For the application of this method, the sample should be highly insulating. Otherwise, currents from ohmic charge transport superimpose the very small pyrocurrent.

Fluctuation (Noise) Spectroscopy

As this review will illustrate, conductance and resistance fluctuation (noise) spectroscopy can serve as a highly informative complementary technique for examining charge and polarization dynamics in dielectric and ferroelectric materials, particularly at temperatures where the sample's conductivity is too high for dielectric spectroscopy. For instance, at elevated temperatures where semiconducting or insulating materials still exhibit relatively high conductivity, or in materials that transition from metal to insulator upon cooling, often accompanied by some form of dipolar ordering, conductance or resistance noise spectroscopy can provide additional insights, capturing relaxation processes similar to those observed with dielectric spectroscopy. Ideally, there is overlap in temperature ranges where both techniques can be applied.

A specific example includes the use of noise spectroscopy to identify structural, glass-like ordering of ethylene end-group dynamics in various organic CT salts[139–141] at around $T \sim 100$ K, where the samples are too conductive for dielectric spectroscopy to effectively study relaxation processes.

The noise power spectral density (PSD) of the resistance (R) fluctuations (the discussion is fully analogous for fluctuations of the conductance G) $\delta R(t) = R(t) - \langle R(t)\rangle$, where $\langle R(t)\rangle$ is the time-averaged mean value that may be considered equal to zero, is defined as the time-averaged squared modulus of the Fourier-transformed fluctuating signal:

$$S_R(f) = 2 \lim_{T\to\infty} \frac{1}{T} \left| \int_{-T/2}^{T/2} \delta R(t) e^{-\mathrm{i}2\pi \mathrm{f}t} \mathrm{d}t \right|^2, \quad (3)$$

where the variance of the signal $\langle \delta R(t)^2 \rangle$ is normalized by $\langle \delta R(t)^2 \rangle = \int_0^\infty S_R(f) \mathrm{d}f$. The quantity S_R describes how much power is contributed by different parts of the frequency spectrum or simply answers the question of how strongly a certain frequency contributes to the system's noise.[142,143]

A simple description of the $1/f$-type fluctuations, which are ubiquitously observed in condensed-matter physics,[142–146] is achieved by the superposition of two-level fluctuations each contributing a Lorentzian spectrum with a certain weight given by the energetics of the two-level system (TLS), schematically shown in Fig. 9a, fluctuating between the ground state and an excited state. The simulated time train shown in (b) displays so-called random telegraph noise (RTN), and the corresponding power spectrum is a Lorentzian, where the corner frequency f_c is directly related to the energy diagram of the TLS, e.g. $f_c = f_0 \exp(-E_a/k_B T)$ for a thermally activated system, where f_0 is an attempt frequency and E_a the effective activation energy of the system. In Fig. 9c it is shown that an ensemble of different switching processes with a certain energy distribution may lead to $1/f$ noise, indicated by the superposition of four TLS each contributing a Lorentzian. Figure 9d displays a representative time-dependent measurement of the resistance of an organic CT salt in the metallic regime fluctuating about a mean value $\langle R(t)\rangle$. As shown in the inset, where $\langle R(t)\rangle$ (the long-term average that usually is of interest in a standard resistance measurement) is subtracted, the relative fluctuations $\delta R/R$ are usually small, i.e., on the order of 0.01% or less. However, the time trace clearly shows that both fast and rather random (uncorrelated) events and long-term correlations are present. The latter are of interest since they reflect the microscopic kinetics of the charge fluctuations. The calculated normalized PSD shown in Fig. 9e can be fitted by a spectrum $S_R/R^2 \propto 1/f^\alpha$ with $\alpha \approx 1$, where both the magnitude of the spectrum—either conveniently taken at 1 Hz or by considering the variance of the signal, i.e., the spectral weight in a given frequency interval over which the PSD is integrated—and the frequency exponent $\alpha(T) = -\partial \ln S_R(T)/\partial \ln f$ are evaluated. $\alpha = 1$ corresponds to a

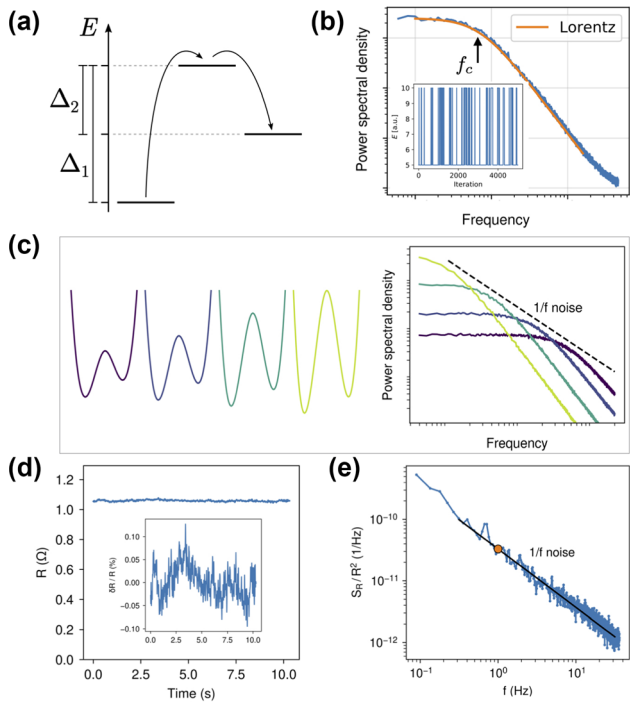

Fig. 9 (a) Schematics of a fluctuating two-level system (TLS) and (b) the simulated time series of the energy (inset) and the corresponding Lorentzian noise spectrum, where the corner frequency f_c is indicated. (c) A superposition of many Lorentzians with a distribution of activation energies gives rise to an overall $1/f$-type spectral behavior. (d) A measured time series of a fluctuating resistance with the relative resistance change shown in the inset. Note that $\delta R/R$ is rather small. (e) The corresponding normalized resistance noise PSD with a generic behavior $S_R/R^2 \propto 1/f^{\alpha}$ characterized by $S_R/R^2(f = 1\,\mathrm{Hz})$ (orange circle) and the frequency exponent $\alpha \approx 1$ (black line) (Color figure online).

homogeneous distribution of the energies of fluctuators contributing to the $1/f$-type noise, and $\alpha > 1$ and $\alpha < 1$ correspond to slower and faster fluctuations in comparison, respectively.[143]

An important theorem in time-dependent statistical physics is the Wiener–Khintchin theorem connecting the power spectrum $S_x(f)$ of any fluctuating quantity x to a time-like property of the statistically varying function $\delta x(t)$.[147] This time-like property is given by the system's autocorrelation function $\Psi_{xx}(\tau) = \langle x(t) \cdot x(t+\tau) \rangle$ describing the microscopic kinetics of the fluctuation process:

$$S_x(f) = 4 \int_0^{\infty} \Psi_{xx}(\tau) \cos(2\pi f \tau) \mathrm{d}\tau. \quad (4)$$

The Fourier transform can be inverted, i.e., measuring the noise PSD in principle provides access to the correlation function $\Psi_{xx}(\tau)$ which is a nonrandom characteristic of the microscopic kinetics of the system's random fluctuations,

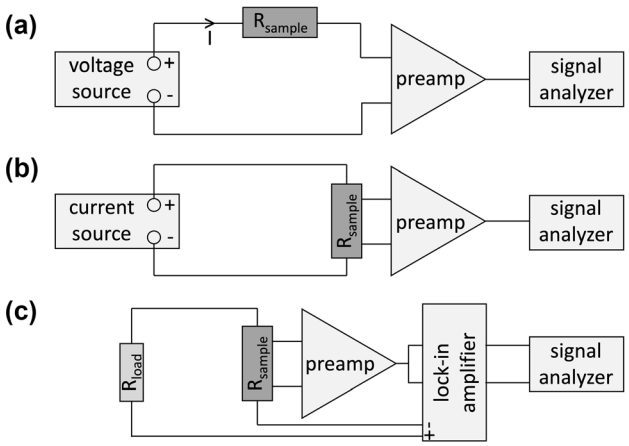

Fig. 10 Different setups for fluctuation spectroscopy. (a) Two-point DC setup for measurement of current (conductance) fluctuations in high-impedance samples. (b) Four-point DC setup and (c) four-point AC setup for measurement of voltage (resistance) fluctuations in more conductive samples. The fluctuating signal in each case is fed into a signal analyzer (e.g., SR785) to obtain the noise power spectral density (PSD). Figure adapted with permission from Ref. 155.

describing how the fluctuations evolve in time on average.[143,144]

For an advanced analysis of any random process $\delta x(t)$, it is possible to define the so-called *second spectrum* $S_x^{(2)}(f)$ as the power spectrum of the fluctuations of $S_x(f)$ with time, i.e., the Fourier transform of the autocorrelation function of the time series of $S_x(f)$, allowing us to access higher-order correlation functions. In practice, an additional frequency f_2 related to the time over which $S_x(f)$ fluctuates is thereby introduced. The second spectrum $S_x^{(2)}(f_2, f)$ probes deviations from Gaussian behavior since it is independent of the frequency f_2 if the fluctuations are uncorrelated, i.e., caused by independent TLS. In contrast, a distinct frequency dependence $S^{(2)} \propto 1/f_2^{\beta}$ with $\beta \approx 1$ is observed for correlated (interacting) fluctuators.[148,149] A frequency-dependent second noise spectrum indicates ergodicity breaking which, e.g., occurs in spin glasses.[150] When the slowing down of carrier dynamics is observed at a metal-insulator transition, a frequency-dependent second spectrum often is interpreted as glassy freezing of the fluctuations due to spatial correlations.[151–154]

As shown in Fig. 10, fluctuation spectroscopy measurements discussed in this review article were performed with a four-point AC (low impedance) or four-point DC method (high impedance) by using a preamplifier and a signal analyzer (see Ref. 155 for detailed information), which provides the PSD of the voltage fluctuations by computing the fast Fourier transform. For measurements of the second spectrum, we employed a fast data acquisition card instead of the signal analyzer in order to determine the power spectral densities from the recorded time signal by a

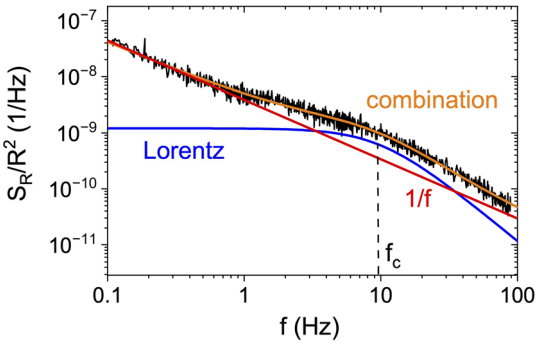

Fig. 11 Typical noise PSD $S_R/R^2(f)$ where a Lorentzian contribution (blue line) is superimposed on the underlying $1/f^{\alpha}$ noise (red line). Orange line is a fit to Eq. 5 (Color figure online).

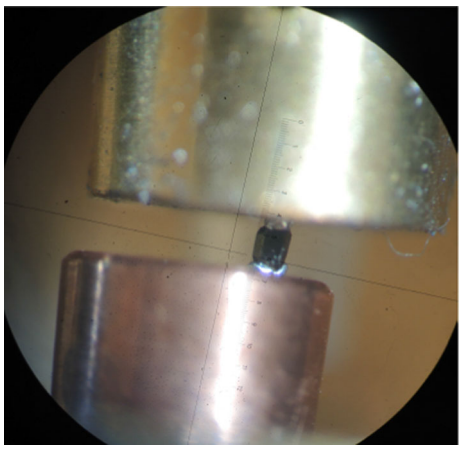

Fig. 12 A single crystal of κ-(BEDT-TTF)$_2$Mn(CN)$_4$ (black color) with a length along the c axis of L_c = 0.708 mm mounted in the dilatometer cell between a (gold-plated) Cu piston above the sample and a Cu block below the sample. The crystal is embedded from above and below in gallium (silver color), serving as a mechanical fit: in mounting the crystal, gallium spheres heated to above their melting temperature were placed above and below the crystal. The piston is then screwed down, thereby deforming the spheres, and the gallium is cooled below its solidification temperature. Figure reprinted with permission from Ref. 159 (Color figure online).

software program. In many conducting systems (like the ones discussed here) the measured PSD of the voltage noise above the equilibrium one increases with the current I as $S_V \propto I^2$ (or the current noise with the voltage V as $S_I \propto V^2$). This is usually interpreted as the modulation noise caused by fluctuations (random modulation) of the sample's resistance $\delta R(t)$ (or conductance $\delta G(t)$). According to Kirchhoff's law, the spectral densities of current noise at fixed voltage and voltage noise at fixed current are simply given by $(S_I/I^2)_V = \text{const.} = S_G/G^2 = (S_V/V^2)_I = \text{const.} = S_R/R^2$, where R is the differential resistance and $G = R^{-1}$ the conductance.[144] Thus, it is common to consider the resistance or conductance noise PSD normalized to the resistance or conductance squared in order to address the relative change in the fluctuation properties.

In general, noise measurements, albeit a macroscopic probe, are suitable for inferring microscopic information, since (i) the noise scales inversely with the system size and (ii) the signature of a single fluctuating TLS may be enhanced over the 1/f-type contribution in the corresponding "noise window" (given by the present temperature, electric and magnetic field, and frequency). Figure 11 shows a typical example of such behavior where the measured spectrum can be described by

$$\frac{S_R(f,T)}{R^2} = \frac{a}{f^{\alpha}} + \frac{b}{f^2 + f_c^2}, \tag{5}$$

where $a(T)$ and $b(T)$ are the amplitudes of the 1/f-type and Lorentzian noise contributions, respectively, and $\alpha(T)$ and $f_c(T)$ their frequency exponent and corner frequency. When analyzing the shift in fluctuating TLS with temperature, electric field, or magnetic field superimposed on underlying $1/f^{\alpha}$ noise with $\alpha \approx 1$, it is convenient to plot $f \times S_R/R^2$ versus f (cf. Figs. 22 and 23 below). This often allows one to estimate the size of switching entities (single particles or clusters), thus gaining information not only on the ground state, but also on the fluctuations to the excited state, as well as the time and length scales at which the fluctuations occur. This is of fundamental importance for nonuniform electronic or magnetic states in condensed-matter systems.[156,157]

Thermal Expansion

Measurements of the relative length changes, $\Delta L_i(T)/L_i$, along the different crystal axes $i = a, b, c$, can provide important information on the involvement of lattice degrees of freedom for the various types of orderings. In addition, it is a very sensitive tool for detecting phase transitions and for identifying their character, i.e., to distinguish a first-order transition from a second-order one. These measurements were performed by using an ultra-high-resolution capacitive dilatometer (built after Ref. 158) with a resolution $\Delta L_i/L_i \geq 10^{-10}$, where L_i is the sample length along the i axis. The obtained $\Delta L(T)/L$ data were differentiated numerically to determine the thermal expansion coefficient $\alpha(T) = 1/L\ \mathrm{d}L/\mathrm{d}T$ using the following procedure: The data for $\Delta L(T)/L$ were divided into equidistant intervals of typically ΔT = 0.15 K for low temperatures (typically $T \leq$ 12 K) and ΔT = 0.35 K for high temperatures (typically $T \geq$ 12 K). In each of the intervals, the mean slope was determined from a linear regression. In a standard experiment, the length changes were measured upon heating with a slow sweep rate $q \leq$ 1.5 K/h to ensure thermal equilibrium. Figure 12 shows an example of a single crystal of κ-(ET)$_2$Mn(CN)$_4$ with

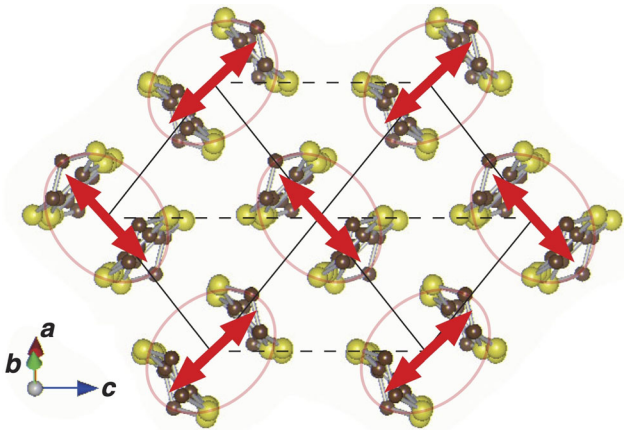

Fig. 13 Top view of the ET layer of κ-$(ET)_2Cu[N(CN)_2]Cl$ (a) with the ellipses indicating the ET dimers. The thick red arrows schematically show the breathing mode with the polarization vector ξ. A wave vector $\mathbf{Q} = (603)$ was chosen for phonon measurements in the $(h0l)$ scattering plane to maximize the scattering intensity. Figure adapted with permission from Ref. 160 (Color figure online).

typical dimensions in the sub-millimeter range and how this crystal is mounted in the dilatometer cell.

Inelastic Neutron Scattering

Fluctuations in the electronic channel accompanying the formation of ferroelectricity may also give rise to phonon renormalization effects. The latter can be sensitively probed by inelastic neutron scattering. Comparing the so-derived excitation spectra with model calculations enables one to identify those phonon modes which couple most strongly to orderings in the electronic channel. For these experiments, deuterated single crystals of κ-$(D_8\text{-}ET)_2Cu[N(CN)_2]Cl$ were used.[160] To improve the signal-to-noise ratio, a composite sample consisting of several co-aligned single crystals with a total mass of 7–9 mg was used. In order to minimize disorder related to the freezing of orientational degrees of freedom of the ET molecules' terminal ethylene end groups,[139,140] the crystals were slowly cooled with $q = -1$ K/min around the freezing temperature T_{glass} = 75 K. In order to study renormalization effects of the intra-dimer breathing mode (red arrow in Fig. 13) in response to ordering phenomena in the spin and charge channel, a momentum transfer between the initial and final state of the neutron of $\mathbf{Q} = (603)$ was selected. Since this wave vector is practically parallel to the polarization vector $\boldsymbol{\xi}$ of the breathing mode, it ensures high scattering intensity which is proportional to $(Q \cdot \boldsymbol{\xi})^2$. Constant-$Q$ scans, performed at various temperatures, reveal clear phonon modes at energies E = 2.6 meV, 6 meV, 8 meV, and 11 meV, which were fitted using damped harmonic oscillator (DHO) functions

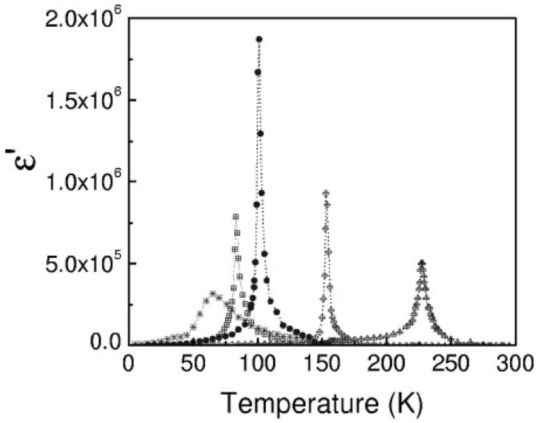

Fig. 14 Temperature dependence of the dielectric constant taken at a frequency of 100 kHz for $(TMTTF)_2X$, with X = PF_6 (stars), AsF_6 (circles), SbF_6 (diamonds), BF_4 (squares), and ReO_4 (triangles). Figure reprinted with permission from Ref. 161.

$$\mathrm{DHO_i}(Q,\omega) = \frac{\Gamma_i \hbar\omega}{[\hbar^2(\omega^2 - \omega_i{}^2)]^2 + (\Gamma_i \hbar\omega)^2}, \qquad (6)$$

where Γ_i and $\hbar\omega_i$ denote the damping factor and phonon energy of the ith mode, respectively. The fits were convolved with the experimental resolution of 0.5 meV.[160] From these fits, the phonon damping Γ_q, i.e., the inverse of the lifetime, and its variation with temperature could be determined. Results are discussed in "Inelastic Neutron Scattering" section.

Signatures of Ferroelectricity Revealed in Quasi-1D and Quasi-2D Systems

Quasi-1D $(TMTTF)_2X$

Dielectric Spectroscopy

Clear signatures for ferroelectricity as a consequence of charge ordering were observed for the quasi-1D $(TMTTF)_2X$ salts for a variety of anions X including PF_6, AsF_6, SbF_6, BF_4, and ReO_4.[12,161] These salts undergo a charge-order transition at T_{CO} = 60–160 K, accompanied by a charge disproportionation 2δ between neighboring TMTTF molecules, as evidenced by NMR[162–164] and infrared vibrational spectroscopy.[165,166] At T_{CO}, the dielectric constant ε' shows a pronounced peak (cf. Fig. 14), reflecting the ferroelectric character of the charge-ordered state. Upon approaching T_{CO} from both sides, the $\varepsilon'(T)$ data follow to a good approximation a Curie–Weiss-like temperature dependence $\varepsilon'(T) = A/|T - T_{CO}|$[161] with a Curie–Weiss constant A for $T < T_{CO}$ which is twice that at $T > T_{CO}$. This behavior is in fact expected for a second-order ferroelectric transition.[111] Detailed investigations of the

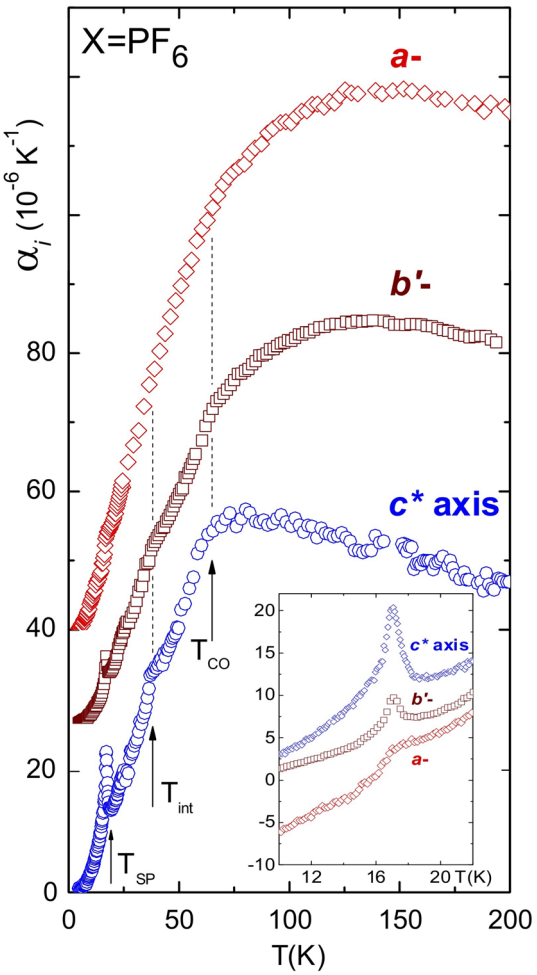

Fig. 15 Uniaxial thermal expansion coefficients α_i measured along three orthogonal axes of $(TMTTF)_2PF_6$. The curves have been offset for clarity. Arrows at T_{SP} and T_{CO} mark the spin–Peierls and charge-ordering transition temperatures, respectively. The arrow at T_{int} marks an anomaly of unknown origin. The inset shows details of the thermal expansion anomalies at the Peierls transition. Figure reprinted with permission from Ref. 168.

frequency dependence of the dielectric response for $(TMTTF)_2AsF_6$[161,167] showed the typical behavior for order–disorder-type ferroelectrics (cf. Fig. 7b), where the electric dipoles that are disordered at high temperatures order with a net overall polarization below a phase-transition temperature T_{FE}[111]. The data revealed a sharp peak in $\varepsilon'(T)$ at low frequencies of 30 kHz and 100 kHz, the amplitude of which is reduced with increasing frequency into the megahertz regime, while the peak position remains nearly unchanged.

Thermal Expansion

The charge-order transition in these salts, which for a long time was labeled the mysterious "*structureless transition*" due to a lack of clear structural signatures, has been

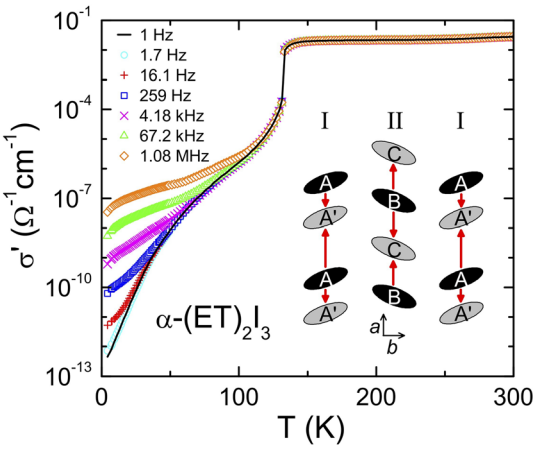

Fig. 16 Temperature dependence of the AC conductivity of α-$(ET)_2I_3$ measured along the out-of-plane c axis at varying frequencies. Inset: Sketch of the ET plane with view along the long axis of the molecules. Black molecules indicate a higher charge value. The dimerization in stack I is strongly exaggerated. The thick red arrows indicate the dipolar moments resulting from the charge disproportionation, summing up to a nonzero polarization. Figure reprinted with permission from Ref. 116 (Color figure online).

attributed to the combined effect of strong on-site, U, and inter-site, V, Coulomb interactions.[169] Hence, these systems have been considered prime examples for electronic ferroelectricity. However, as demonstrated by high-resolution thermal expansion measurements, there are distinct lattice effects accompanying the transition at T_{CO}[168] (cf. Fig. 15). Surprisingly, the strongest effects were observed along the c^* axis, which is perpendicular to the stacking axis of the TMTTF molecules. In fact, finite lattice effects are expected given that atomic displacements, breaking the system's inversion symmetry, are prerequisites for ferroelectricity to occur. Based on the observed thermal expansion anomalies, a scheme was proposed where the CO within the TMTTF stacks gives rise to a uniform (q = 0) displacement of the anions X^-. The proposed shift of the anions lifts the inversion symmetry, thereby creating the ferroelectric character of the transition. For further details on the rich phenomenology revealed for these quasi-1D molecular conductors, see, e.g., the reviews in Refs. 13, 14, and 161.

Quasi-2D α-$(BEDT\text{-}TTF)_2I_3$

AC Conductivity

In α-$(ET)_2I_3$, the ET molecules are arranged in herringbone fashion, with two crystallographically different stacks I and II along the a axis (see inset of Fig. 16).[116] In stack I, the ET molecules denoted by A and A′ are weakly dimerized, whereas the molecules B and C in stack II are not dimerized. Charge ordering, giving rise to a metal–insulator

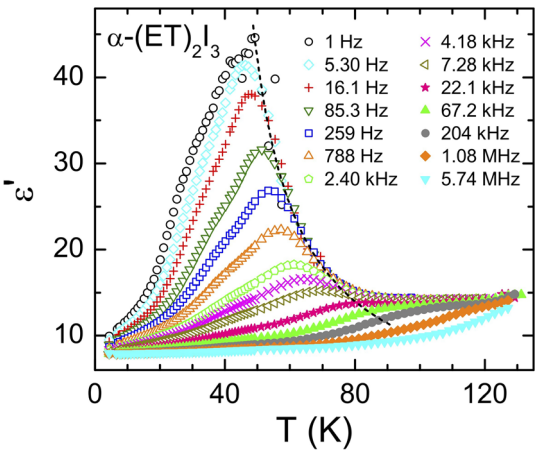

Fig. 17 Temperature dependence of the dielectric constant $\varepsilon'(T)$ of α-$(ET)_2I_3$, measured for electric field perpendicular to the ET planes at varying frequencies. The dashed line indicates Curie–Weiss behavior with a Curie–Weiss temperature Θ_{CW} = 35 K. Figure reprinted with permission from Ref. 116.

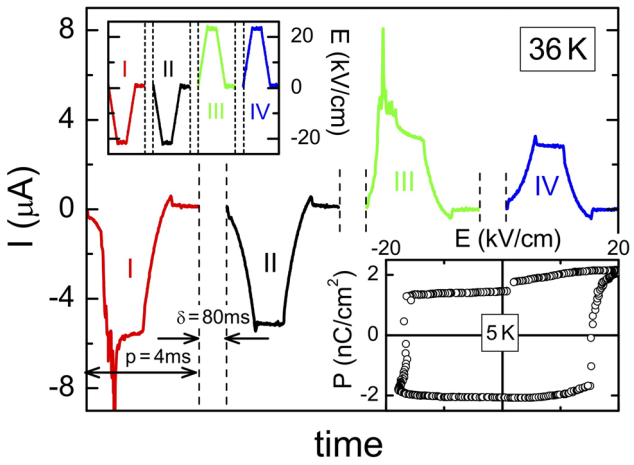

Fig. 18 Time-dependent current as detected in α-$(ET)_2I_3$ by PUND measurements at 36 K. δ denotes waiting time and p the pulse width. Left inset shows the excitation signal whereas the right inset shows the polarization-field hysteresis curve at 5 K. Figure reprinted with permission from Ref. 116.

transition,[170] was observed at T_{CO} = 135 K[171,172] (cf. the conductivity data in Fig. 16), revealing a rapid drop below T_{CO}. In fact, a charge-ordered ground state was predicted theoretically for this salt with a quarter-filled hole band based on the combined effect of on-site and inter-site Coulomb interactions.[1,69] The pattern of CO can be viewed as analogous to the horizontal stripe patterns of the θ-phase compounds (Fig. 6). While a nonuniform charge distribution was observed already in the metallic state above T_{CO},[173] the charge disproportionation becomes more pronounced below T_{CO}. Based on optical second-harmonic generation (SHG) measurements,[174,175] providing evidence for a non-centrosymmetric crystal structure—a prerequisite for ferroelectricity—this salt was indeed shown to be a candidate for electronic ferroelectricity.

Dielectric Spectroscopy

Measurements of the dielectric constant $\varepsilon'(T)$ for electrical field E aligned perpendicular to the ET planes (Fig. 17) revealed clear signatures for relaxor-type ferroelectricity[116] (cf. Fig. 7c). The data exhibit a pronounced peak in $\varepsilon'(T)$ around 40–50 K at low frequencies, which shrinks in size and is shifted to higher temperatures with increasing frequency. The variation in the peak position with frequency was found to be in accord with a VFT law (Eq. 2)[132–134] which is well established in glass physics[135] and often seen in relaxor ferroelectrics.[129,130] The high-temperature flank of the $\varepsilon'(T)$ peaks can be described by a Curie–Weiss law (broken line in Fig. 17) with a Curie–Weiss temperature Θ_{CW} = 35 K, providing at least a rough estimate of the freezing temperature. Notably, dielectric measurements for fields E parallel to the ET planes failed to reveal a peak in $\varepsilon'(T)$.[176,177] The reason for that is likely related to the distinctly higher in-plane conductivity even in the charge-ordered state, making dielectric measurements difficult. It should be noted that the dipolar polarization in α-$(ET)_2I_3$ should be predominantly oriented parallel to the ET planes. However, in Ref. 116 it was argued that the dipolar moment in this and related materials should also have a component oriented perpendicular to the planes, detected by the dielectric measurements performed in that work.

Polarization Measurements

Further evidence for ferroelectric order was provided by probing the macroscopic polarization using PUND measurements (see "Polarization Measurements" section for details on the technique). Upon the application of a sequence of trapezoid electrical field pulses (left inset of Fig. 18), a current was observed with characteristic peaks in response to the first and third pulse when the electric field $|E|$ exceeds a threshold level of the order of 20 kV/cm, indicating the switching of the macroscopic polarization (cf. Fig. 8b and c). In contrast, no such peaks were observed for the second and fourth pulse, as the polarization was already switched by the preceding pulse.

The results on the dielectric response and polarization provided clear evidence for ferroelectricity in α-$(ET)_2I_3$. The dielectric response was found to be typical for relaxor-type ferroelectricity. In contrast to the findings for the various $(TMTTF)_2X$ salts discussed above, where ferroelectricity sets in at T_{CO}, here it appears to occur deep in the charge-ordered state. In Ref. 116 it was argued that this decoupling of polar and CO and the occurrence of relaxor ferroelectricity in α-$(ET)_2I_3$ arises from the alteration of undimerized and dimerized stacks in the α-type structure

which could counteract the formation of canonical long-range ferroelectricity directly below T_{CO}. Instead, between T_{CO} and about 80 K, in Fig. 17, conventional dipolar relaxation behavior is found (cf. Fig. 7d). In Ref. 116 it was proposed to arise from the relaxation of single dipoles or several ferroelectrically correlated dipoles within one chain.

Quasi-2D θ-(BEDT-TTF)$_2$RbZn(SCN)$_4$

In the θ-polymorph, the ET molecules form a quarter-filled electron system on a triangular lattice implying some degree of (charge) frustration. This salt shows CO, as predicted theoretically,[178,179] accompanied by a structural transition at T_{CO} = 200 K.[88,91,180–183] Interestingly, through rapid cooling the charge-order transition was avoided, and instead, glasslike charge dynamics were observed, which were assigned to a novel charge-glass state.[184]

Dielectric Spectroscopy

Measurements of the dielectric constant revealed gradual growth upon cooling from room temperature, followed by a sharp peak at T_{CO}, with an almost divergent behavior in the immediate vicinity of T_{CO}.[185] The observed smooth increase in $\varepsilon'(T)$ in the metallic regime is likely related to the observation of slowly fluctuating charge disproportionation in this temperature regime.[186] It was found that on the low-temperature side, a jump-like drop occurs within a narrow temperature window, below which $\varepsilon'(T)$ levels off at low values. Interestingly, in Ref. 185, the amplitude of the $\varepsilon'(T)$ peak was found to decrease with increasing frequency. This points to order–disorder type of ferroelectricity where fluctuating dipoles already exist above the transition (see "Dielectric Response of Ferroelectrics" section), in accord with the suggested formation of short-range charge disproportionation already above T_{CO}.[186]

Thermal Expansion

Although the behavior of $\varepsilon'(T)$ reported in[185] reveals clear signatures of ferroelectricity associated with the charge-order transition, there are distinct differences to the phenomenology observed in the (TMTTF)$_2X$ and α-(ET)$_2$I$_3$ salts. This can be attributed to the strong first-order character of the structural transition in θ-(BEDT-TTF)$_2$RbZn(SCN)$_4$ accompanied by a lattice modulation, which is also reflected in pronounced discontinuous changes of the c-axis lattice parameter (Fig. 19) and the hysteresis upon cooling and warming in ε'[185] and $\Delta l/l$.[183]

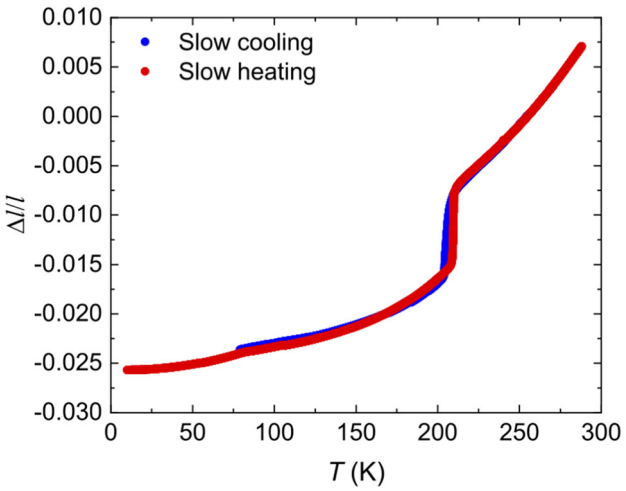

Fig. 19 Relative length change for θ-(ET)$_2$RbZn(SCN)$_4$ measured along the in-plane c axis upon cooling and heating. Figure reprinted with permission from Ref. 183.

Quasi-2D β'-(BEDT-TTF)$_2$ICl$_2$

Dielectric Spectroscopy

Measurements of the dielectric constant $\varepsilon'(T)$ of this material for electric fields perpendicular (Fig. 20a) and parallel (Fig. 20b) to the ET layers revealed clear anomalies in the temperature range 80–150 K, with a strong frequency dependence, characteristic of relaxor-type ferroelectricity (see "Dielectric Response of Ferroelectrics" section).[109,110,187] By analyzing the high-temperature flank of the anomaly, yielding a Curie–Weiss-like temperature dependence, a Curie–Weiss temperature of 67 K was obtained.[126] Further evidence for ferroelectricity in this salt came from studies of the electric polarization obtained by measurements of the pyrocurrent for poling fields parallel to the b axis (cf. Fig. 21). A small but clearly resolvable polarization was obtained below a critical temperature T_{FE} = 62 K, which is close to the above-mentioned Curie–Weiss temperature of 67 K. Measurements with poling fields up to 3 kV/cm aligned along the out-of plane a^* axis failed to detect a pyrocurrent, consistent with the notion that the electric dipoles originate from the ET dimers. The observed phenomenology, i.e., the strong frequency-dependent dielectric response alongside the small polarization, indicates the formation of glassy polar domains in this salt, typical for relaxor ferroelectrics. As it exhibits antiferromagnetic ordering below $T_N \approx 22$ K[188] but only short-range polar order, the spin and dipolar degrees of freedom in β'-(ET)$_2$ICl$_2$ obviously are not closely coupled.

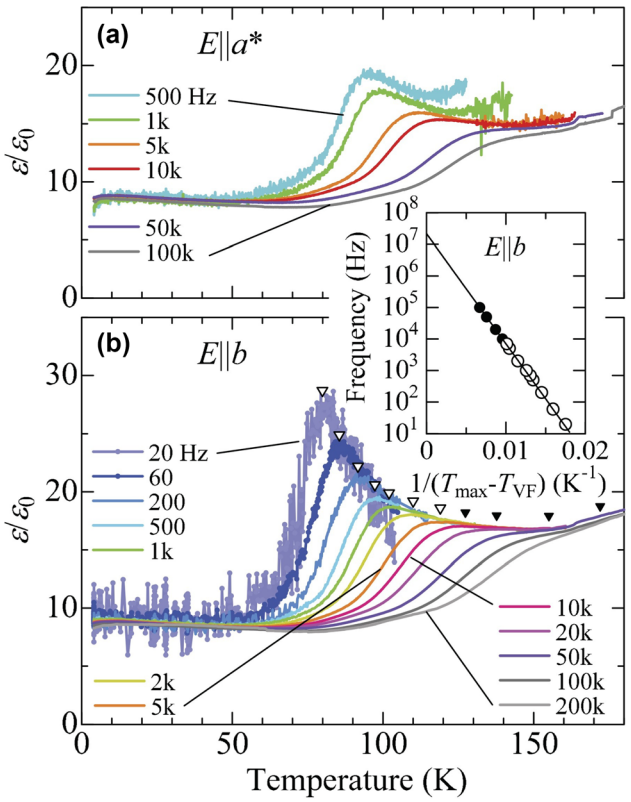

Fig. 20 Temperature dependence of the dielectric constant $\varepsilon'(T)$ of β'-$(ET)_2ICl_2$ for electric field perpendicular (a) and within (b) ($E\|b$) the ET layers. Data were taken for frequencies between 500 Hz and 100 kHz. Figure reprinted with permission from Ref. 126.

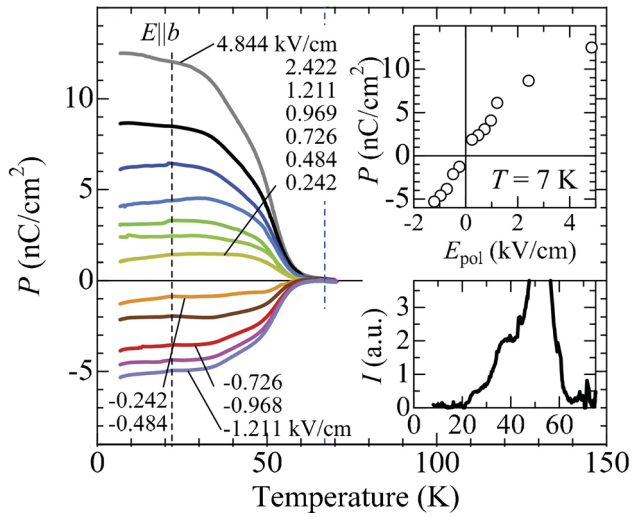

Fig. 21 Temperature dependence of the electric polarization of β'-$(ET)_2ICl_2$ for $E\|b$ and a poling electric field from -1.211 to $+4.844$ kV/cm obtained by pyrocurrent measurements. Figure adapted with permission from Ref. 126.

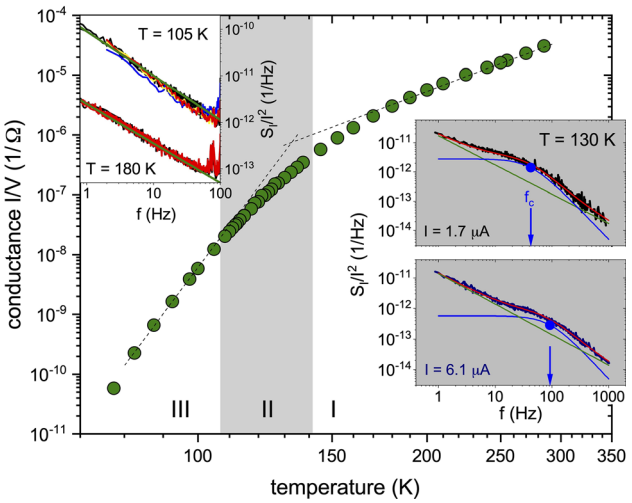

Fig. 22 Conductance of β'-$(ET)_2ICl_2$ versus temperature. (Dashed lines indicate a crossover to more insulating behavior upon cooling.) In the areas labeled I and III, the normalized current noise PSD is $1/f$-like and independent of the applied electric field (left inset, green lines are fits to $S_I/I^2 \propto 1/f^\alpha$; for $T = 180$ K and 105 K, two and four different currents, respectively, are shown). In the gray shaded temperature regime II (110–140 K), a single Lorentzian is superimposed on the underlying $1/f$-type noise, and $S_I/I^2(f)$ depends on the external electric field. Right insets show representative spectra for regime II. Lines are fits to Eq. 5 with $\alpha = 1$. Figure reprinted with permission from Ref. 190 (Color figure online).

Conductance Fluctuation (Noise) Spectroscopy

The system β'-$(ET)_2ICl_2$ is a strong dimer-Mott insulator, where electric-field-induced charge disproportionation has been demonstrated by charge-sensitive Raman scattering.[189] The material is well suited for complementary studies of dielectric and conductance noise spectroscopy, where the latter method also aims to probe the effects of collective fluctuations at temperatures far above the Curie–Weiss temperature and the onset of electric polarization at 67 K and 62 K, respectively, a regime where samples are too conductive for performing the former technique. As will be discussed below, the conductance fluctuations provide evidence for an important consequence of large dielectric fluctuations, namely, the formation of polar nano-regions (PNR) and electronic (e.g., paraelectric–ferroelectric) phase separation,[60] which may help to explain the heretofore puzzling occurrence of either long-range ferroelectric order or relaxor-type ferroelectricity in the class of quasi-2D organic CT salts.[8,49,127]

Figure 22 shows the DC conductance $G = V/I$ vs. T of β'-$(ET)_2ICl_2$, where V is the voltage applied across the sample and I the measured electric current flow. The $\log G$ vs. $\log T$ representation indicates a crossover to more insulating behavior (stronger decrease in the conductance) below about 130–140 K (see dashed lines).

At discrete temperatures, the current noise PSD $S_I(f, T)$ measured for various excitation voltages V allows one to identify three distinct temperature regimes (see also Fig. 24a below): For temperatures $T \gtrsim 140$ K (regime I)

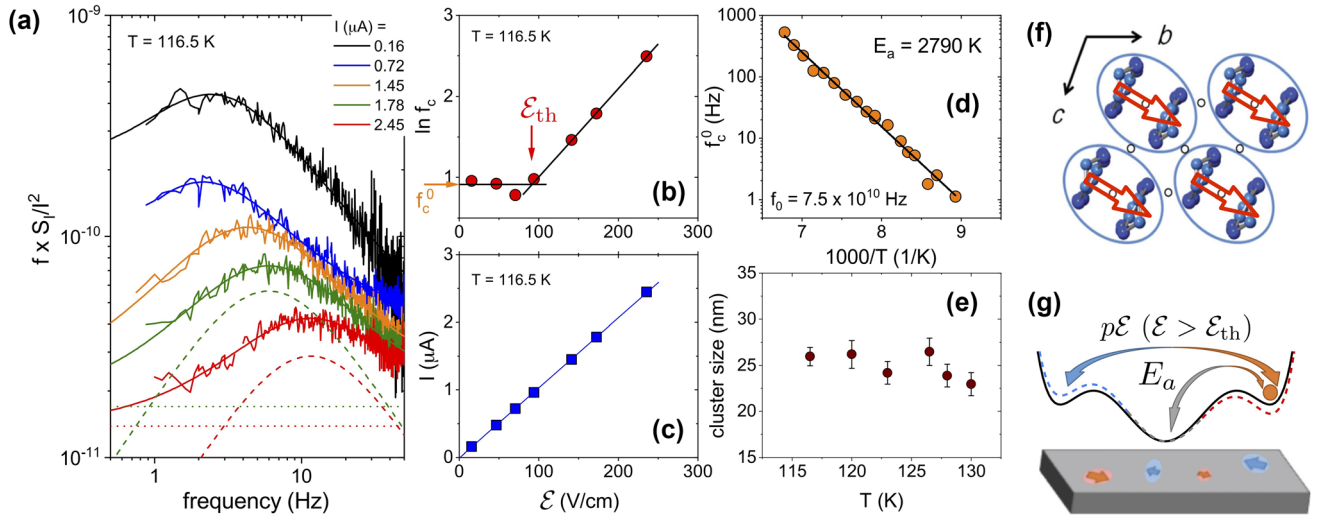

Fig. 23 (a) Representative noise spectra of β'-$(ET)_2ICl_2$ as $f \times S_I/I^2$ vs. f in temperature regime II at fixed $T = 116.5$ K and different sample currents as indicated. Smooth solid lines are fits to Eq. 5. For two selected currents, the $1/f$ and Lorentzian contributions are shown (dotted and dashed lines, respectively). (b) Electric field dependence of the corner frequency f_c. Lines are guides for the eyes indicating the threshold field $\mathcal{E}_{th}$ and the zero-field value $f_c^0 \equiv f_c(\mathcal{E} \to 0)$. (c) The linear I–V regime. (d) Arrhenius plot of f_c^0 vs. $1/T$ revealing an activation energy $E_a/k_B = 2790$ K. (e) Cluster size calculated from p estimated from Eq. 8; see text. (f) Arrangement of ET dimers in the conducting planes and orientation of the electric dipoles. (g) Schematics of the suggested zero-field/electric field-induced dielectric/ferroelectric fluctuations; see text for details. Figure adapted with permission from Ref. 190.

and $T \lesssim 110$ K (regime III), the normalized noise spectra are of generic $1/f^{\alpha}$-type and independent of the applied electric field $\mathcal{E} = V/l$ (with l being the distance between the electric contacts along the sample's c axis), i.e., the expected scaling $S_I \propto I^2$ is obeyed; see representative noise spectra in these regimes in the left inset of Fig. 22. In between, for $110\,\text{K} \lesssim T \lesssim 140$ K (regime II), we find a single Lorentzian spectrum—characteristic for a fluctuating TLS—superimposed on the underlying $1/f^{\alpha}$ noise (cf. Fig. 11 and Eq. 5 in "Fluctuation (Noise) Spectroscopy" section above).

Strikingly, in regime II, the observed normalized noise spectra depend on $\mathcal{E}$, i.e., the $S_I \propto I^2$ scaling is not valid. The corner frequency f_c is related to the characteristic energy of the two-level fluctuator, and for thermally activated states of a double-well potential, one has

$$f_c = f_0 \exp\left(-\frac{E_a}{k_B T}\right), \tag{7}$$

with an activation energy E_a, an attempt frequency f_0, and Boltzmann's constant k_B.[146]

The anomalous current dependence of the noise spectra in regime II is shown exemplarily in the right inset of Fig. 22. Clearly, f_c, and hence the characteristic energy of the fluctuation process, shift with I, i.e., depend on the electric field $\mathcal{E}$, with f_c increasing from 42 Hz at $T = 130$ K for a sample current of $I = 1.7$ μA to $f_c = 93$ Hz for $I = 6.1$ μA (blue arrows).

This unusual current/electric field dependence of the noise spectra in the temperature regime II is illustrated in greater detail in Fig. 23a for a representative temperature of $T = 116.5$ K in regime II. Solid lines are fits to Eq. 5. Note that in the representation $f \times S_I/I^2$ vs. f, the $1/f$-term is a constant (for $\alpha \approx 1$) and the Lorentzian term exhibits a peak centered at f_c; see the respective dotted and dashed curves representing these contributions for two selected currents. An important finding is a threshold behavior of the corner frequency f_c, shown Fig. 23b, which stays roughly constant for small values of the electric field $\mathcal{E}$ (orange arrow) until it increases exponentially above a threshold field $\mathcal{E}_{th}$ (red arrow). Thus, distinct low-$\mathcal{E}$ and high-$\mathcal{E}$ behavior is observed. Phenomenologically, we describe the characteristic frequency of the two-level fluctuations by Eq. 7 for $\mathcal{E} \le \mathcal{E}_{th}$ and by an additional term (see also Ref. 191), resulting in

$$f_c = f_0 \exp\left(\frac{p(\mathcal{E} - \mathcal{E}_{th}) - E_a}{k_B T}\right) \quad \text{for} \quad \mathcal{E} \ge \mathcal{E}_{th}. \tag{8}$$

Importantly, for all applied electric fields shown here, the I–V characteristics (see Fig. 23c) remain linear, which excludes a trivial heating effect to account for the shift of f_c. For the subthreshold value $f_c^0 \equiv f_c(\mathcal{E} \to 0)$, we find an excellent fit to an Arrhenius behavior (Eq. 7), yielding $E_a/k_B = (2790 \pm 70)$ K (see Fig. 23d), an energy very close to the intra-dimer transfer integral and optical charge gap of ~ 2900 K,[40,192,193] which indicates that the observed switching processes in temperature regime II are

of electronic origin. We suggest that the competing inter- and intra-dimer Coulomb interactions[51,57] cause coherent fluctuations of electrons within a cluster of dimers (i.e., the gravity center of the hole), switching between the unpolarized dimer-Mott state and a charge disproportionated state; see scheme $[E_a]$ in Fig. 23g.

The above-threshold behavior can be described by Eq. 8, yielding a constant slope p that can be determined from a linear fit to the data in Fig. 23b. This indicates a *discrete* value of a fluctuating dipole moment that corresponds to a cluster of a certain size. At $T = 116.5$ K, we find $p = 1.73 \times 10^{-23}$ C · cm and a threshold field of $\mathcal{E}_{\rm th} \sim 92$ V/cm. With the dipole moment $p_{\rm d} = 0.13\,ed$ parallel to the b axis estimated in Ref. 126 (e and d = 3.6 Å are the electron charge and distance between the ET molecules in a dimer, respectively, see Fig. 23f), we find that the total number N of elementary dipoles within the cluster—taking into account the projection onto the measured c axis—amounts to $N = p/p_{\rm d}^{c-\rm axis} \approx 9 \times 10^4$ dimers. Assuming a spherical object, this corresponds to a fluctuating cluster volume with radius $r_{\rm cluster} \approx 26$ nm. Thus, the observed low-frequency dynamics below ~ 140 K are caused by the formation of fluctuating PNR, which above a threshold field $\mathcal{E}_{\rm th}$ undergo switching between two states of polarization $+p$ and $-p$; see scheme $[p\mathcal{E}]$ in Fig. 23g.

This dipole-dimer picture has the two polar states ($+p$ and $-p$) and one nonpolar state (n) whose energies and corresponding lifetimes are modified in a finite electric field $\mathcal{E} > \mathcal{E}_{\rm th}$. A simple estimate[190] shows that $f_{\rm c}$ does not change due to the lifetime of the nonpolar dimer Mott state but rather *always increases* with an increasing electric field due to a second-order effect related to the lifetimes $\tau_{+\rm p}$ and $\tau_{-\rm p}$. This can be viewed as a transition between the $+p$ and $-p$ states and determines the origin of the threshold field $\mathcal{E}_{\rm th}$. Figure 23e shows the estimates of the cluster size for other temperatures, revealing a roughly constant or slightly increasing size of the PNR with decreasing temperature.

Here, it is important to note that very similar coupling of two-level excitations to the electric field indicating the presence of fluctuating PNR has been observed for the relaxor ferroelectrics κ-$(ET)_2Cu[N(CN)_2]Cl$ and κ-$(BETS)_2Mn[N(CN)_2]_3$ (see "Fluctuation Spectroscopy" section and "Electrical Resistivity" section below).

A more complete picture of the charge carrier dynamics coupled to the dielectric behavior in β'-$(ET)_2ICl_2$ probed by current noise arises when also considering the underlying 1/*f*-type fluctuations. At high temperatures (regime I), the frequency exponent $\alpha(T \gtrsim 140\,\text{K}) \approx 0.8$,[190] i.e., there is considerably more spectral weight at higher than at lower frequencies. As discussed above, at about 140 K, upon entering regime II, fluctuating PNR are formed, with one such fluctuator being enhanced in our "noise window," i.e., it strongly couples to the conductance fluctuations, which become a sensitive probe to changes in the *dielectric* properties. The fluctuating electrical polarization potentials of the PNR act on the transport channel as small capacitor gates that locally modulate the conductance of the underlying resistor network.[194,195] The superposition of many fluctuating PNR then constitutes part of the underlying 1/*f*-type. This picture of an enhanced localization of charge carriers and increasingly slow dynamics due to the formation of dimer units that fluctuate coherently as

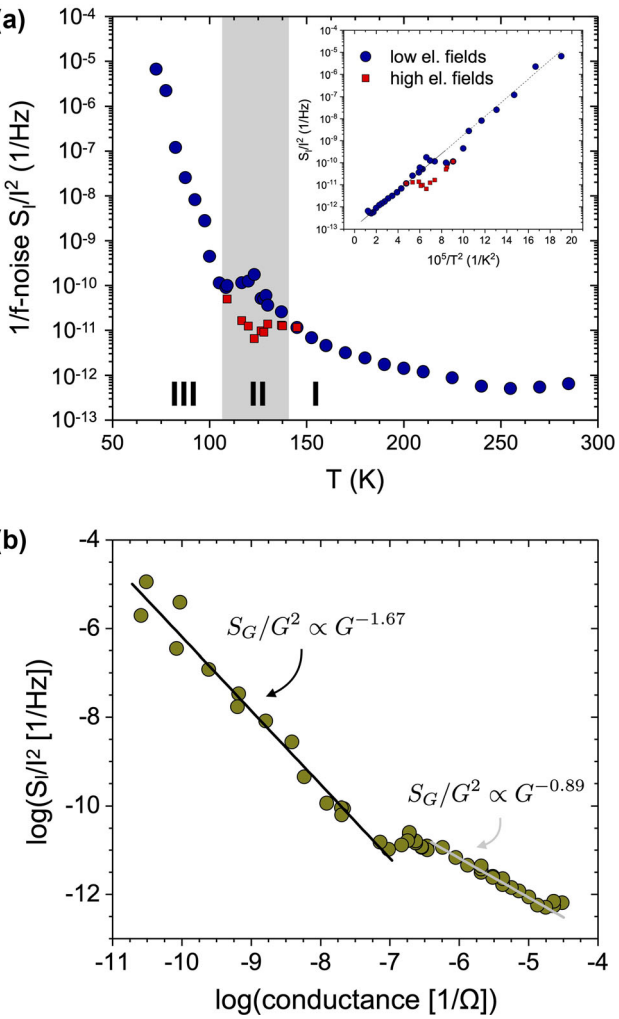

Fig. 24 (a) Normalized current noise PSD S_I/I^2 of β'-$(ET)_2ICl_2$ at 1 Hz vs. T. Shown is only the term $a(T)$ in Eq. 5. Blue and red symbols denote the asymptotic low- and high-electric-field behavior, respectively, in regime II. Inset: Scaling plot of the same data suggesting variable-range hopping (VRH) transport.[194] Blue and red symbols denote the low- and high-electric field limit. (b) Scaling of the normalized conductance noise S_G/G^2 with the conductance G (temperature here is an implicit parameter). The scaling exponents w differ in the different temperature regimes I and III, reflecting the change in transport mechanism. Figure adapted with permission from Ref. 190 and Supplementary Information of Ref. 190 (Color figure online).

extended clusters is corroborated by the rather abrupt increase in the frequency exponent $\alpha(T)$ from almost constant values of $\alpha(T) \approx 0.8$ in temperature regime I to values of $\alpha \gtrsim 1$ below about 140 K,[190] implying a substantial shift of the current fluctuations' spectral weight to low frequencies below this temperature, which may indicate some clusters merging and possibly switching cooperatively.

As shown in Fig. 23a, the 1/*f*-noise magnitude decreases with increasing electric field, with a tendency for saturation at high fields (not shown), with α approaching values of 1 indicating the stabilization of an increasing number and/or size of PNR that increases the total volume of slow fluctuators, thereby reducing the 1/*f*-type noise in regime II, which may be viewed as the superposition of many independently fluctuating clusters with a broad energy distribution.[146]

Upon further decreasing the temperature, in regime III the slow dynamics of the now stabilized PNR dominate the 1/*f*-noise, which below about 110 K shows a drastic increase (see Fig. 24), which is consistent with fluctuations remaining localized due to the strong Coulomb interaction and the fluctuating electric dipole potential modulating the conductance of neighboring elements in a conducting resistor network with variable-range hopping (VRH). This, in turn, corresponds to a change in the electronic transport mechanism, which can be inferred from the scaling behavior (same data) S_I/I^2 vs. G (see Fig. 24b). A linear behavior in such a plot is obeyed at high temperatures (regime I) and low temperatures (regime II) and implies a power-law scaling $S_G/G^2 \propto G^{-w}$ as expected for a percolation scenario in a random resistor network. The scaling exponent w depends on the details of the network/percolation scenario and is usually determined numerically,[144,196] from which in some cases the mechanism of percolative transport can be deduced (see, e.g., Ref. 157). A roughly linear scaling is observed for both temperature regimes I and II, however with a significantly different slope indicating a drastic change in the electronic transport mechanism in accord with the analysis of the low-frequency charge carrier dynamics discussed in Ref. 190.

Regime II ($110\,\mathrm{K} \lesssim T \lesssim 140\,\mathrm{K}$) marks the transformation to the ergodic relaxor state, in which polar regions on nanometer scale with randomly distributed directions of dipole moments, the PNR, appear. (In relaxor ferroelectrics, this temperature can be twice as high as their freezing temperature, giving rise to the peak in permittivity.[187]) This corresponds to the transformation from conductive to dielectric behavior, which is in agreement with the experimental observation that the dielectric response begins to appear in regime II,[126] being accompanied by a slowing down of the charge fluctuations seen in the conductance noise. In β'-$(ET)_2ICl_2$, the low-frequency noise due to switching of PNR (in regime II) and the low-frequency dispersion of the dielectric response (in regime I) may have the same origin.

Quasi-2D β'-(cation)[Pd(dmit)$_2$]$_2$

Dielectric Spectroscopy

Figure 25 shows results for the dielectric constant $\varepsilon'(T)$ measured along the out-of-plane direction of β'-(cation)[Pd(dmit)$_2$]$_2$ salts for different cations (dmit denotes 1,3-dithiol-2-thione-4,5-dithiolate).[197] The dielectric response is similar for all compounds investigated, yielding an anomaly in ε' which is strongly frequency-dependent and shows a Curie–Weiss-like increase upon cooling, similar to the response found in relaxor-type ferroelectrics (Sect. "Dielectric Response of Ferroelectrics").[109,110,187] The Me_4P and Me_4Sb salts (Me = CH_3; left and middle frame of Fig. 25) are known to exhibit antiferromagnetism below $T_N = 40$ K and 18 K, respectively,[198] and thus can be formally regarded as multiferroic, albeit with short-range polar order only. In contrast, β'-$EtMe_3Sb$[Pd(dmit)$_2$]$_2$ (Et = C_2H_5; right frame of Fig. 25) was reported to be a quantum spin liquid, avoiding any magnetic order due to quantum fluctuations.[199] In Ref. 199, this spin-liquid state was suggested to be stabilized by the random freezing of dipolar degrees of freedom within the $[Pd(dmit)_2]^-$ dimers in this compound, as indicated by its dielectric behavior. Indeed, cluster-like, short-range relaxor ferroelectricity as evidenced by $\varepsilon'(T, \nu)$ of this material (Fig. 25) is usually assumed to involve glasslike freezing of dipole motions.[109,110,187] However, one should be aware that the dielectric behavior of all three materials in Fig. 25 is qualitatively similar, but only one of them was considered to exhibit a quantum spin-liquid ground state. In this respect, β'-Me_4P[Pd(dmit)$_2$]$_2$ and β'-Me_4Sb[Pd(dmit)$_2$]$_2$ resemble β'-$(ET)_2ICl_2$, revealing long-range spin but only short-range polar order (Sect. "κ-$(BEDT\text{-}TTF)_2Cu_2(CN)_3$").

Beyond the Dimer-Mott Limit: The Case of κ-phase (BEDT-TTF)$_2$X

The observation of ferroelectric signatures in the κ polymorph, which began in 2010 with Abdel-Jawad and collaborators[197] reporting a relaxor-type dielectric response in the spin-liquid candidate system κ-$(ET)_2Cu_2(CN)_3$, came as a surprise. Until this observation, the key aspects of these κ-phase salts, such as their magnetic properties and proximity to the Mott metal–insulator transition, could be

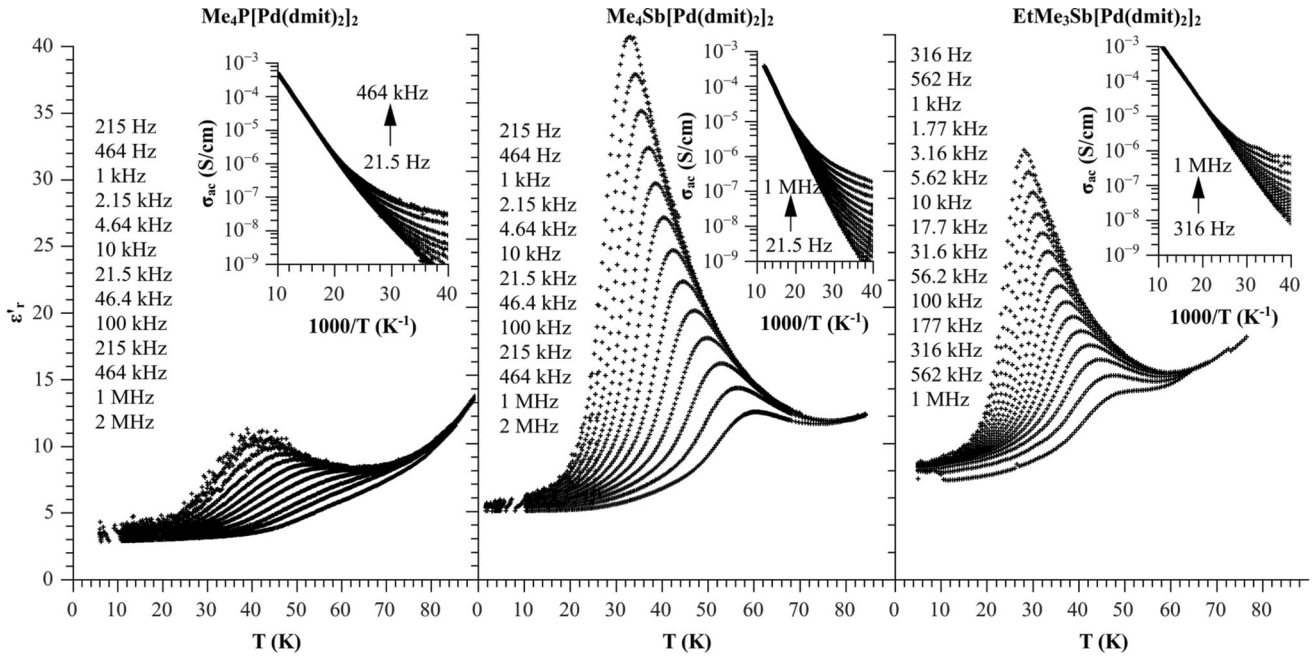

Fig. 25 Temperature dependence of the out-of-plane dielectric constant of β'-(cation)[Pd(dmit)$_2$]$_2$ salts measured at varying frequencies. The insets show the corresponding data for the AC conductivity. Figure reprinted with permission from Ref. 197.

well understood by treating the systems in the dimer-Mott limit.[2,3,22,200] As discussed in Sect. "Theoretical phase diagrams", this limit corresponds to the case of strong dimerization, i.e., a dominant intra-dimer hopping term t_1 being much larger than inter-dimer hoppings t and t' (see Fig. 5). In such a scenario, no ferroelectric response would be expected, as the intra-dimer degrees of freedom are completely frozen.

κ-(BEDT-TTF)$_2$Hg(SCN)$_2$Cl

We start the discussion with κ-(ET)$_2$Hg(SCN)$_2$Cl, where strong evidence was provided for electronic ferroelectricity. Based on density functional theory (DFT) calculations,[36] this salt has moderate strength of dimerization $t_1/t' \approx 3$, placing it in between the quarter-filled charge-ordered systems such as θ-(ET)$_2$RbZn(SCN)$_4$ (undimerized) and half-filled dimer-Mott systems such as κ-(ET)$_2$Cu[N(CN)$_2$]Cl ($t_1/t' \approx 6$).

Infrared Conductivity

The κ-(ET)$_2$Hg(SCN)$_2$Cl salt is known to undergo a metal–insulator transition around 30 K.[201–203] By measurement of the infrared reflectance, probing the charge-sensitive $B_{1u}(\nu_{27})$ mode,[204] this transition was shown to be accompanied by CO.[203] Figure 26 shows conductivity spectra in the frequency range around the $B_{1u}(\nu_{27})$ mode, which is associated with the out-of-phase vibrations of the C=C bonds of the inner rings of the ET molecule. At room

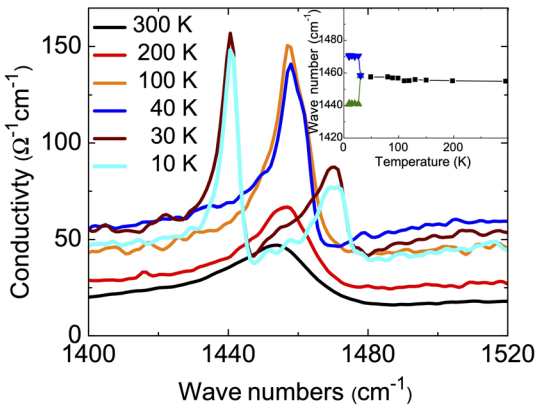

Fig. 26 Temperature dependence of the infrared conductivity spectra of κ-(ET)$_2$Hg(SCN)$_2$Cl measured perpendicular to the ET planes in the region of the $B_{1u}(\nu_{27})$ mode. The inset shows the temperature dependence highlighting a single mode above 30 K which splits into two components below 30 K. Figure reprinted with permission from Ref. 203.

temperature, a single $B_{1u}(\nu_{27})$ mode is found at 1454 cm^{-1}, which splits into two components at 1441 and 1470 cm^{-1} upon cooling through the metal-insulator transition (cf. inset of Fig. 26), indicating the appearance of two differently charged ET molecules. Based on an empirical relation between the ν_{27} frequency and the molecule's charging state,[204] a charge disproportionation of 0.2 e was obtained.[203]

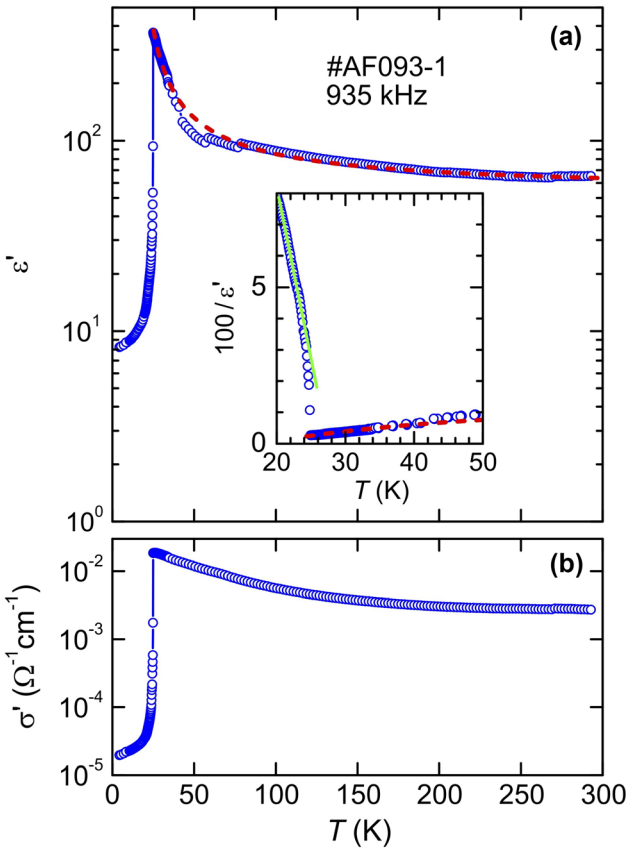

Fig. 27 Temperature dependence of the dielectric constant $\varepsilon'(T)$ (a) and AC conductivity $\sigma'(T)$ (b) of κ-$(ET)_2Hg(SCN)_2Cl$ measured at 935 kHz. The red dashed line in (a) is a Curie–Weiss fit with some offset. The inset shows the inverse dielectric constant with the lines corresponding to Curie–Weiss behavior above and below the phase transition. Figure reprinted with permission from Ref. 36 (Color figure online).

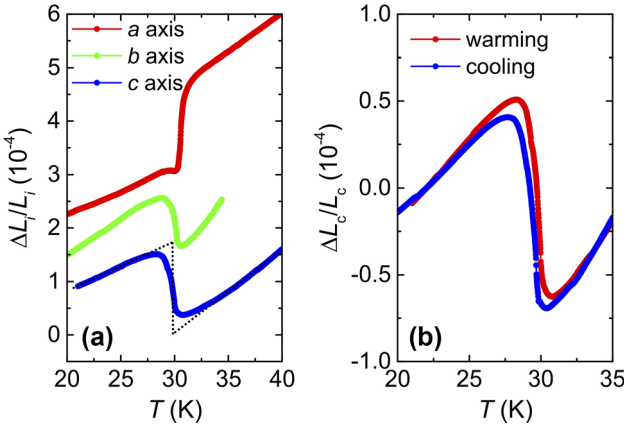

Fig. 28 (a) Relative length change $\Delta L_i/L_i$ as a function of temperature along the $i = a, b, c$ axis of κ-$(ET)_2Hg(SCN)_2Cl$ around the charge-order metal–insulator transition. The individual datasets were shifted for clarity. Dotted line indicates an idealized sharp jump for the c-axis data. (b) Relative length change along the c axis measured upon warming and cooling. Figure reprinted with permission from Ref. 36.

Dielectric Spectroscopy

Measurements of the dielectric constant $\varepsilon'(T)$ of this salt, performed with the electric field applied along the out-of-plane a axis, show an increase upon cooling and a sharp peak at $T_{FE} \approx 25$ K, indicative of a ferroelectric transition (Fig. 27a).[36] Corresponding data for AC conductivity on the same crystal (Fig. 27b) revealed metallic behavior at higher temperatures, followed by a rapid drop at the metal–insulator transition T_{MI} around 25 K by about three orders of magnitude. These data demonstrate the coincidence of the metal–insulator and ferroelectric transitions, i.e., $T_{MI} = T_{FE}$, for this salt. The data for the dielectric constant, after correcting for a background contribution, were found to follow a Curie–Weiss behavior $\varepsilon' - \varepsilon'_{off} = C/(T - T_{CW})$, with a Curie–Weiss temperature of $T_{CW} \approx 17$ K and a Curie constant $C \approx 2500$ K (dashed line in Fig. 27a). Measurements of $\varepsilon'(T)$ at high frequencies up to about 1 GHz (Supplementary Information of Ref. 36) revealed a progressive reduction of the ε' peak amplitude with increasing frequency. This behavior, along with the rather small Curie constant, is consistent with order–disorder ferroelectricity (cf. Fig. 7b).

Within a simple model,[205] the Curie constant is related to the size of the dipoles by

$$\varepsilon' = \frac{C}{(T - T_{CW})} = \frac{1}{3\varepsilon_0} n \left[\frac{p^2}{k_B (T - T_{CW})}\right] \times \left[1 + \left(\frac{T_{CW}}{C}\right) \times (\varepsilon_L - 1)\right], \quad (9)$$

where C is the Curie constant, T_{CW} the Curie–Weiss temperature, ε_0 the dielectric permittivity of vacuum, n the dipole density, p the dipole moment, k_B the Boltzmann constant, and ε_L the low-temperature dielectric constant. This yields $p \approx 0.4\, ed$, with e the electronic charge and $d \approx 4.0$ Å the distance between two ET molecules within the dimer.[36] In light of the simplifications leading to Eq. 9 and the uncertainties of the absolute value of ε', this value compares reasonably well with an expected out-of-plane dipole moment of 0.13 ed, corresponding to the observed charge disproportionation of $\pm 0.1\, e$[203] and the inclination of the ET molecules away from the a axis, resulting in a tilt of the dipole moment by about 50°.[42] It is worth mentioning that for the related κ-$(ET)_2Hg(SCN)_2Br$ salt which shows a metal–insulator transition at $T_{MI} = 90$ K, the situation is less clear. Here, relaxor-type ferroelectricity[206] together with indications for a dipole liquid,[207] effects of disorder,[62] a spin-glass type ground state,[65] and weak ferromagnetic signatures[65,208] was reported.

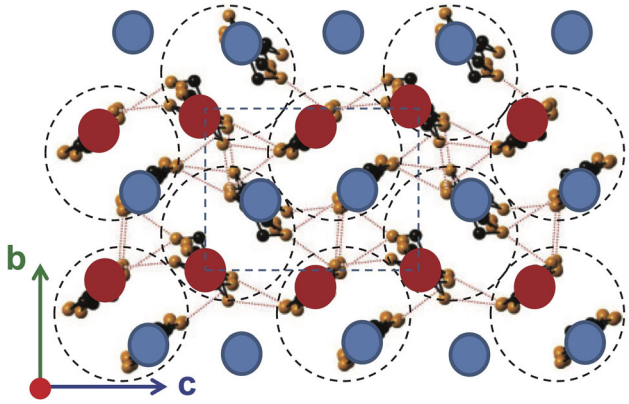

Fig. 29 Favored charge-order pattern for κ-$(ET)_2Hg(SCN)_2Cl$ below $T_{MI} = T_{FE}$ based on the anisotropy of infrared optical conductivity data[203] and consistent with thermal expansion data.[42] Red (blue) spheres indicate charge-rich (charge-poor) ET molecules. Figure adapted with permission from Ref. 203 (Color figure online).

Thermal Expansion

Measurements of the relative length change $\Delta L_i/L_i$ along the out-of-plane *a* axis and the in-plane *b* and *c* axes revealed slightly broadened jumps at $T_{MI} = T_{FE}$ (Fig. 28a), with a small hysteresis between warming and cooling (Fig. 28b), demonstrating the first-order character of the phase transition. This is consistent with the dielectric response yielding a Curie–Weiss behavior both above and below T_{FE} with strongly different slopes $|d(1/\varepsilon')/(dT)|$ (cf. inset of Fig. 27a) together with a Curie–Weiss temperature $T_{CW} < T_{FE}$.[111]

Proposed Charge-Order Pattern

The observed lattice effects at the phase transition highlight a particularly strong effect along the out-of-plane *a* axis, indicating an involvement of the anion layer in the formation of the charge-ordered state. In fact, given the ionic character of these salts, a change in the charge distribution within the ET layers will inevitably be accompanied by shifts of the counter ions in the anion layers. Based on the observed anisotropic lattice effects, a charge-order pattern was suggested where the charge-rich molecules are arranged in stripes along the *c* axis and alternate with charge-poor stripes along the *b* axis (cf. Fig. 29).[203] This is the horizontal stripe pattern depicted in Fig. 5. This pattern, which is consistent with the infrared-conductivity spectra in Ref. 203, breaks inversion symmetry both within and between the layers, and thereby enables three-dimensional ferroelectricity to form.

Interaction of Charge Order with Magnetic Degrees of Freedom

The presence of spin degrees of freedom in the related dimerized salts β'-$(ET)_2ICl_2$ and κ-$(ET)_2Cu[N(CN)_2]Cl$, giving rise to antiferromagnetic order, raises the question about the interaction of CO with the magnetic degrees of freedom in κ-$(ET)_2Hg(SCN)_2Cl$. In fact, based on previous electron spin resonance (ESR) measurements,[202] it was suggested that antiferromagnetic order accompanies the CO below T_{FE} in κ-$(ET)_2Hg(SCN)_2Cl$. However, detailed ESR studies together with specific heat measurements performed in Ref. 42 failed to detect any signatures for a magnetic transition around T_{MI}. It was suggested in Ref. 42 that as a consequence of the CO, the magnetic interactions are modified, thereby promoting a quasi-1D spin liquid state. See Sect. "Theoretical phase diagrams" for a further discussion on this issue.

Fluctuation (Noise) Spectroscopy

Fluctuation spectroscopy measurements of κ-$(ET)_2Hg(SCN)_2Cl$[209] revealed a strong change in the magnitude of resistance fluctuations of at least three orders of magnitude coinciding with the charge-ordering transition, in agreement with intrinsic electronic inhomogeneities inherent to the first-order transition. Entering the ferroelectric phase upon cooling is accompanied by a shift of spectral weight to lower frequencies. Only below the metal–insulator transition do the normalized noise spectra exhibit an anomalous current dependence, where with an increasing electric field, a discrete shift of the 1/*f*-type spectra or a change in the amplitude and corner frequency of Lorentzian spectra were observed, similar to the findings on other κ-phase compounds discussed in this review. Also, the second spectrum shows a frequency dependence only for temperatures below T_{MI}, implying non-Gaussian, spatially correlated fluctuations.

κ-$(BEDT\text{-}TTF)_2Cu_2(CN)_3$

Dielectric Spectroscopy

First indications for a ferroelectric response in dimerized quasi-2D organic CT salts were observed in κ-$(ET)_2Cu_2(CN)_3$ by Abdel-Jawad *et al.*[127] in measurements of the dielectric constant (see Fig. 30). This salt had long been considered as a candidate system for the realization of a quantum spin liquid.[33] This notion was initially supported by this salt being a weak dimer-Mott insulator, i.e., electronic states which are close to the metal–insulator transition, featuring a triangular lattice with a high degree of frustration $t'/t = 0.84$, which increases to 0.86 at 5 K[210]

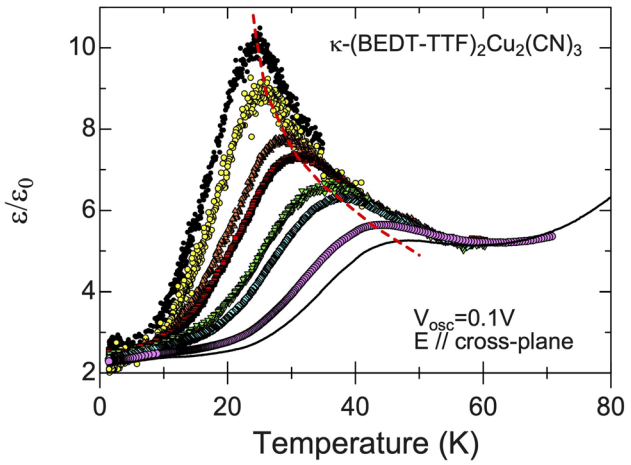

Fig. 30 Normalized dielectric constant of κ-$(ET)_2Cu_2(CN)_3$ measured with electric field aligned along the *a* axis, i.e., perpendicular to the ET planes for varying frequencies. The broken line connects the maximum positions. Figure adapted with permission from Ref. 127.

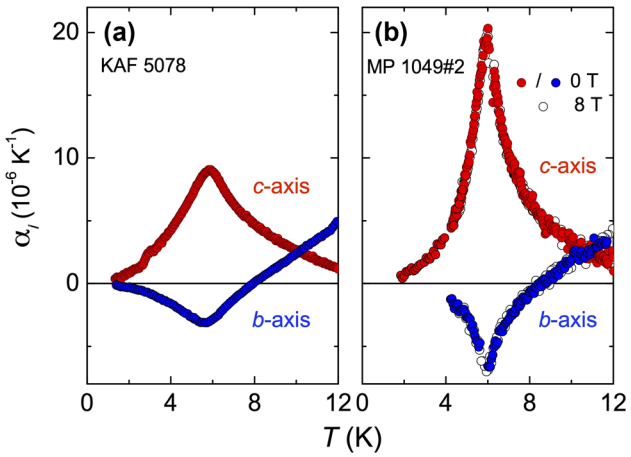

Fig. 31 Thermal expansion coefficients for two different crystals of κ-$(ET)_2Cu_2(CN)_3$ measured along the in-plane *b* and *c* axes around the 6 K phase transition anomaly. The data in (a) were reported in Ref. 214; the data in (b), where the anomalies are most strongly pronounced, were reported in Ref. 215. Figure reprinted with permission from Ref. 215.

(see Table I). However, the ultimate zero-temperature ground state of this salt has been challenged recently on the basis of new experimental and theoretical insights,[34,211] indicative of the formation of spin singlets in an ordered or glassy manner at low temperatures (see Ref. 212 for a recent comprehensive review).

Measurements of the dielectric constant along the out-of plane *a* axis (Fig. 30)[127] revealed a peak anomaly below about 60 K, the position and height of which showed a pronounced frequency dependence typical for a relaxor-type ferroelectric; see also Ref. 213 for fields aligned parallel to the ET planes. The peak anomaly was found to follow to a good approximation a VFT law $\nu = \nu_0 \exp[-B/(T_{max} - T_{VFT})]$, corresponding to Eq. 2 for

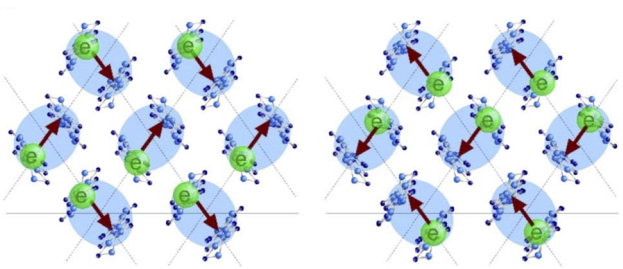

Fig. 32 Possible short-range domains of collectively fluctuating quantum electric dipoles (arrows) resulting from intra-dimer charge disproportionation. Figure adapted with permission from Ref. 127.

$\nu = 1/(2\pi\tau)$, again typical for relaxor ferroelectrics as discussed in Sect. "Dielectric response of ferroelectrics".[109,110,187] Here ν is the frequency, ν_0 a pre-exponential factor, and T_{max} is the position of the maximum in ε'. With $T_{VFT} \approx 6$ K, a good description of the data was achieved.

Moreover, as shown in Ref. 127, the high-temperature envelope curve of the ε' peaks for the various frequencies, representing the static dielectric constant, was found to follow a Curie–Weiss law with a Curie–Weiss temperature of $T_{CW} = 6$ K providing a rough estimate of the freezing temperature. It is interesting to note that at this temperature, anomalous behavior was observed in a variety of properties—commonly referred to as the "*6 K anomaly*" (see Ref. 212). This anomaly is particularly strongly pronounced in the thermal expansion,[214] indicating a strong coupling to the lattice degrees of freedom. While the thermal expansion results provided clear indications for a phase transition at 6 K, the size of the phase transition anomaly, rather than its position, revealed significant sample-to-sample variations[215] (cf. Fig. 31), highlighting the role of disorder.

The scenario put forward in Ref. 127, and also discussed by others,[51,56,216,217] involved fluctuating charges (holes) on the dimer site (see Fig. 32), corresponding to fluctuating dipoles which give rise to the observed relaxational response. The relaxor ferroelectricity revealed at low temperatures thus can be assigned to a finite intra-dimer charge disproportionation, driven by intermolecular Coulomb interactions, combined with the influence of disorder.

Optical and Raman Spectroscopy

Spectroscopic studies aiming to identify the origin of the ferroelectric signatures came to conflicting conclusions. Whereas infrared vibrational-spectroscopy studies failed to detect clear indications for a line splitting and therefore suggest the absence of charge disproportionation,[218] Raman scattering revealed a clear line broadening consistent with intra-dimer charge fluctuations.[219] Strong evidence for fluctuating intra-dimer charge and spin

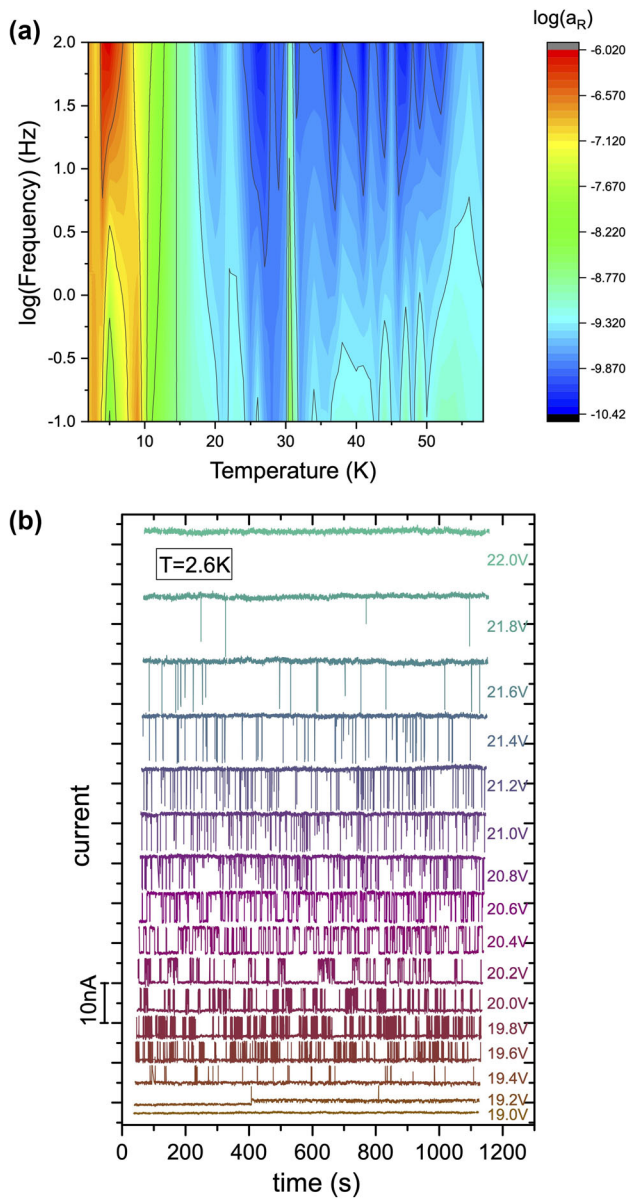

Fig. 33 (a) Relative conductance noise level $\log(a_R = f \times S_I/I^2)$ vs. T vs. $\log(f)$ for κ-$ET_2Cu_2(CN)_3$. (b) Two-terminal current fluctuations at $T = 2.6$ K for different applied voltages. Figure adapted with permission from Ref. 222.

fluctuations were found in recent inelastic neutron scattering experiments by taking advantage of the strong coupling of these fluctuations to certain intra-dimer vibrational modes.[220] In this study, a compilation of 47 co-aligned crystals of deuterated κ-$(D_8$-$ET)_2Cu_2(CN)_3$ were investigated, with particular focus on low-energy breathing modes of the ET dimers. A drastic change was observed in the phonon damping for a low-lying optical mode at an energy E = 4.7 meV, assigned to an intra-dimer breathing mode,[221] upon cooling below 6 K. It was argued that the drastic increase in the lifetime of this mode below 6 K can be attributed to a phase transition involving the lattice and its coupling to the charge and spin degrees of freedom.[220].

Fluctuation (Noise) Spectroscopy

Also for κ-$(ET)_2Cu_2(CN)_3$, strongly enhanced low-frequency fluctuations around 6 K and TLS coupled to the electric field have been observed. Figure 33a displays the dimensionless normalized relative conductance noise level $a_R(T,f) = f \times S_I/I^2(T,f)$ showing a strong increase in the $1/f$-type fluctuations upon cooling to temperatures below about 25 K, which can be roughly described by a model of variable-range hopping.[222] Note that there is a pronounced peak in the noise, most prominent at the higher end ($f > 10$ Hz) of the measured frequency range at 6 K, i.e., yet another anomaly at this temperature which is compatible with a phase transition at this temperature. A nearly frequency-independent sharp peak in the noise above 30 K coincides with a change in the activation energy of the conductivity in a Mott variable-range hopping model. Related to the dielectric properties is the time train of the measured current at different voltages for $T = 2.6$ K, i.e., deep in the relaxor ferroelectric state, shown in Fig. 33b. Interestingly, in a certain interval of the applied electric field $\mathcal{E}$, we observe distinct two-level fluctuations, where the relative lifetime of the states are found to be inverted with varying $\mathcal{E}$. Such behavior is in agreement with a thermally activated switching of polar clusters, found for β'-$(ET)_2ICl_2$, κ-$(ET)_2Cu[N(CN)_2]Cl$, and κ-$(BETS)_2Mn[N(CN)_2]_3$, which is described for the latter salts in detail in Sects. 4.4.2, 5.3.5, and 5.4, respectively.

κ-$(BEDT\text{-}TTF)_2Cu[N(CN)_2]Cl$

Dielectric Spectroscopy

This salt represents a particularly interesting case where strong indications for ferroelectricity were observed which occur simultaneously with the transition to antiferromagnetic order.[8] This finding was remarkable for two reasons: First, it establishes this material as another multiferroic CT salt alongside the above-mentioned $(TMTTF)_2SbF_6$ and β'-$(ET)_2ICl_2$. Second, and in contrast to the latter two cases, where the ferroelectric and magnetic order set in at distinctly different temperatures, here the simultaneous occurrence of both orders suggests an intimate coupling between ferroelectricity and magnetism, as reviewed in Sect. "Theoretical Phase Diagrams". The κ-$(ET)_2Cu[N(CN)_2]Cl$ salt was investigated intensively in the past due to its special character as a weak dimer-Mott insulator, featuring an anisotropic triangular lattice, in close proximity to unconventional

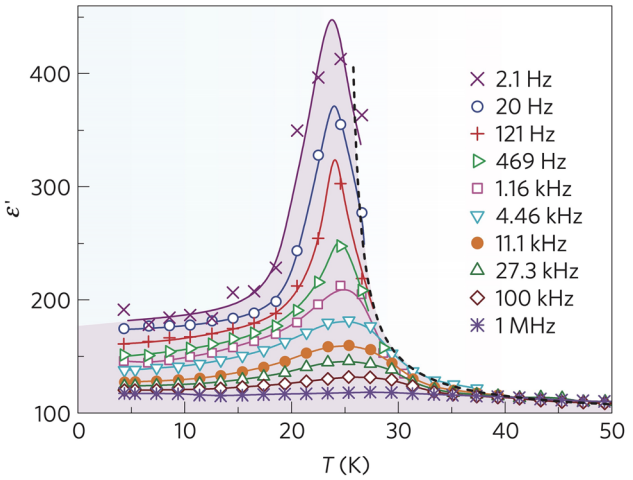

Fig. 34 Temperature dependence of the dielectric constant for electric fields aligned perpendicular to the ET planes of κ-$(ET)_2Cu[N(CN)_2]Cl$. Data were taken at varying frequencies. The dashed line indicates Curie–Weiss behavior with a Curie–Weiss temperature T_{CW} = 25 K. Figure reprinted with permission from Ref. 8.

superconductivity.[2,3,22,34] The system shows long-range antiferromagnetic order below $T_N = 27$ K,[37] consistent with the material's moderate degree of frustration $t'/t \approx 0.46$[40,45] (see Table I). The pressure–temperature phase diagram (Fig. 4) has been studied in great detail by numerous groups,[23–25,29,38] especially with regard to the Mott transition and its critical behavior, justifying the notion of this material representing a good realization of the dimer-Mott scenario. In fact, the degree of dimerization here amounts to $t_1/t' = 6.2$,[40] exceeding the values of $t_1/t' = 4.3$ for κ-$(ET)_2Cu_2(CN)_3$ and $t_1/t' = 3.1$ for κ-$(ET)_2Hg(SCN)_2Cl$ (cf. Table I).

It therefore came as a surprise that measurements of the dielectric constant on this salt, performed for electric fields perpendicular to the ET planes, revealed strong indications for ferroelectricity.[8] As seen in Fig. 34, the $\varepsilon'(T)$ data exhibit a peak around 25 K which is most strongly pronounced at the lowest frequency. It decreases in size with increasing frequency, whereas its position remains practically unaffected. The signatures revealed in these investigations bear the characteristics of an order–disorder-type ferroelectric (cf. Fig. 7b). In Ref. 8, the polar state realized here has been assigned to CO within the ET dimers,[8] although alternative interpretations have been proposed[223–225] (see Ref. 13 for a critical discussion). It should be mentioned that, so far, attempts to experimentally resolve the intra-dimer charge disproportionation have remained unsuccessful,[218] indicating that CO, if present, is rather weak.

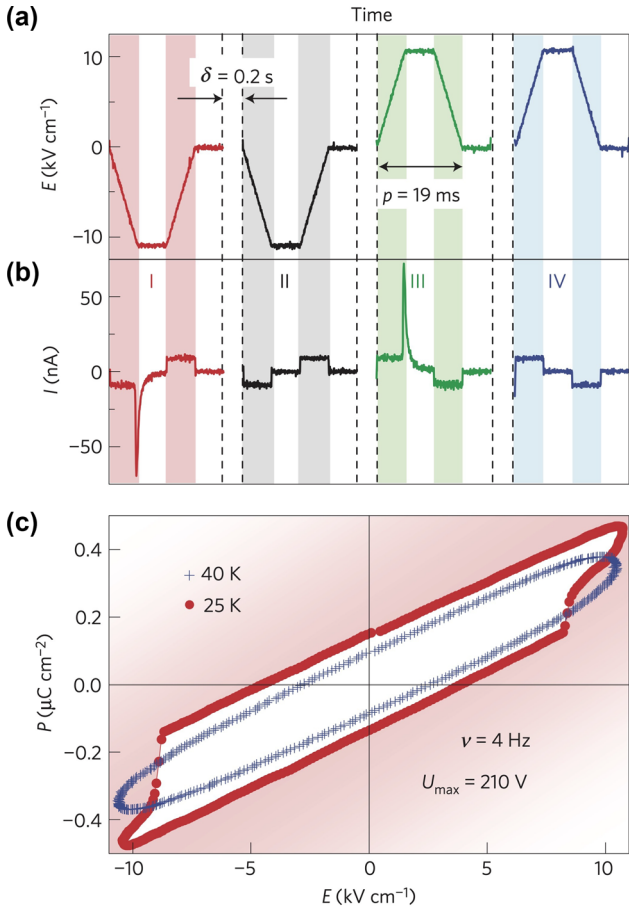

Fig. 35 (a) Time-dependent excitation signal with electric field perpendicular to the ET planes of the PUND measurements for κ-$(ET)_2Cu[N(CN)_2]Cl$. The data were taken at 25 K. (b) Resulting time-dependent current with spikes in response to the pulses I and III. (c) Polarization-field hysteresis curves taken at temperatures above (crosses) and just below (red spheres) the occurrence of ferroelectric order. Figure reprinted with permission from Ref. 8 (Color figure online).

Polarization Measurements

Further strong evidence for ferroelectricity was provided by PUND measurements (see Sect. "Polarization Measurements"), where a peak-like current response was observed when the electric field $|E|$ exceeded a threshold field of about 10 kV/cm for the first and third pulse, indicating the switching of ferroelectric domains (see Fig. 35b).[8] These peaks were absent for the second and fourth pulse, as the domains were already switched by the proceeding pulse. Moreover, measurements of the field-dependent polarization $P(E)$ (Fig. 35c)[8] revealed an elliptical curve at 40 K, i.e., above T_{FE}, consistent with a linear polarization response (paraelectricity), with some loss contributions from charge transport. In contrast, at lower temperatures, just below the temperature at which ferroelectric order sets in, nonlinear behavior was observed

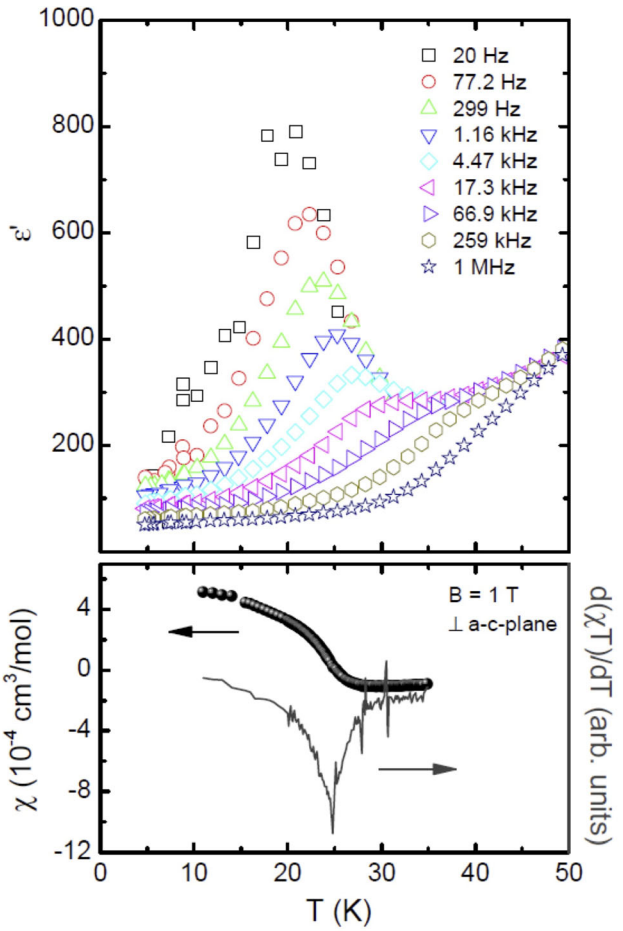

Fig. 36 Temperature dependence of the out-of-plane dielectric constant of single-crystalline κ-$(ET)_2Cu[N(CN)_2]Cl$ (different sample than in Fig. 34) measured at various frequencies. The lower panel shows the magnetic susceptibility (left scale) together with the derivative $d(\chi \cdot T)/dT$ (right scale) on the same crystal. The susceptibility was taken at a field of 1 T applied perpendicular to the ET planes. Figure adapted with permission from Ref. 49.

above about 8.5 kV/cm, with the tendency to saturation at highest fields, indicative of ferroelectric polarization switching (cf. Fig. 8a).

Influence of Extrinsic Effects: Sample-to-Sample Variations

In an attempt to look for sample-to-sample variations with regard to the dielectric response, overall eight κ-$(ET)_2Cu[N(CN)_2]Cl$ single crystals from different sources were investigated.[49] The dielectric response was measured for electric fields perpendicular to the ET planes. The crystals were also subjected to magnetic characterization using a SQUID (superconducting quantum interference device) magnetometer for identifying the transition into antiferromagnetic order. Two different types of dielectric response were revealed. One group of crystals (five out of eight) showed the order–disorder-type dielectric response (cf. Fig. 7b) as, e.g., seen in Fig. 34 discussed above, characterized by a pronounced peak in $\varepsilon'(T)$, the position of which is practically independent of the frequency. The second group of crystals (three out of eight) revealed a significant shift of the peak position to higher temperatures with increasing frequency, typical for relaxor-type ferroelectricity (Fig. 7c), as examplarily shown in the upper panel of Fig. 36. Despite their different dielectric response, very similar magnetic behavior was found, yielding a steplike anomaly in the magnetic susceptibility, corresponding to a spike in $d(\chi \cdot T)/dT$ around 25 K (cf. lower panel of Fig. 36), consistent with literature results on the magnetic order in this salt.[37] The study showed that in all cases, clear ferroelectric signatures occur around the magnetic transition, while sample-specific effects, likely originating from different crystal growth conditions, affect the dielectric properties more than the magnetic ones,[49] changing the order–disorder type ferroelectric response into a relaxor-type one.

Inelastic Neutron Scattering

The scenario that has been put forward based on the above phenomenology[8,49] involves fluctuating charges on the ET dimers above T_{FE}, corresponding to fluctuating dipoles, and the polar ordering (long-range or short-range, depending on sample) of these fluctuations below T_{FE}. In light of significant electron–lattice coupling characterizing these salts, the different dynamics of the charge should also be reflected in the dynamics of certain lattice modes, in particular the intra-dimer breathing modes, which can be sensitively probed by inelastic neutron scattering. By using a collection of co-aligned deuterated single crystals κ-$(D_8\text{-}ET)_2Cu[N(CN)_2]Cl$ with a total mass of 9 mg, the dynamics of low-lying vibrational modes were investigated.[160] In fact, strong renormalization effects could be observed for the low-lying mode at an energy $E = 2.6$ meV, which was assigned to an intra-dimer breathing mode (cf. Fig. 13). Figure 37 shows characteristic phonon parameters, obtained from fitting the phonon peak at $E = 2.6$ meV by a damped-harmonic oscillator function (cf. Eq. 6), and their variation with temperature. The data reveal a strong increase in the damping factor Γ_q, the inverse of the phonon lifetime, when the charge carriers become localized on the dimer site below T_{ins}, reflected by the rapid increase in the resistivity (cf. Fig. 37d). The damping is decreased once static order develops below $T_N = T_{FE} = 25$ K. The phonon anomaly and its peculiar temperature dependence becomes clearly visible in the scattering intensity taken at an energy $E = 1.5$ meV (Fig. 37c), which strongly increases around T_{ins} and decrease near $T_N = T_{FE}$. It was argued in Ref. 160 that such a phonon renormalization effect reflects the strong coupling to some relaxational mode. This

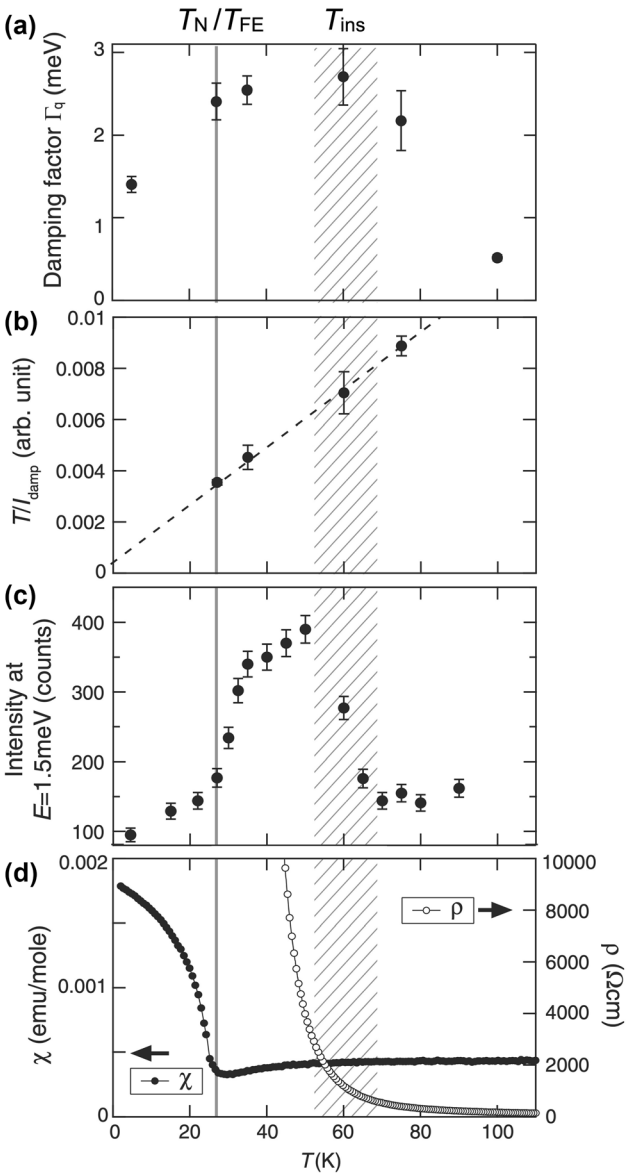

Fig. 37 Temperature dependence of the damping factor Γ_q (a) for a low-lying intra-dimer breathing mode at E = 2.6 meV of κ-(D_8-ET)$_2$Cu[N(CN)$_2$]Cl measured at a momentum transfer **Q** = (603), (b) T/I_{damp}, with I_{damp} the integrated intensity of the overdamped mode. The finite T/I_{damp} at $T_N = T_{FE}$ indicates that a structural change is not the primary order parameter for the phase transition at this temperature. (c) Scattering intensity measured at an energy E = 1.5 meV at (603), (d) the out-of-plane electrical resistivity $\rho(T)$ (right scale) and magnetic susceptibility $\chi(T)$ (left scale). The hatched area marks the crossover temperature T_{ins}, corresponding to the opening of the charge gap, and $T_N = T_{FE}$ marks the temperature of orderings in the spin and charge channel. Figure reprinted with permission from Ref. 160.

is the case when the characteristic frequency and wave vector of this relaxational mode matches with the corresponding figures of those phonon modes. The coincidence of the phonon anomaly and T_{ins}, below which the charge gap opens,[226,227] strongly suggests a coupling between the

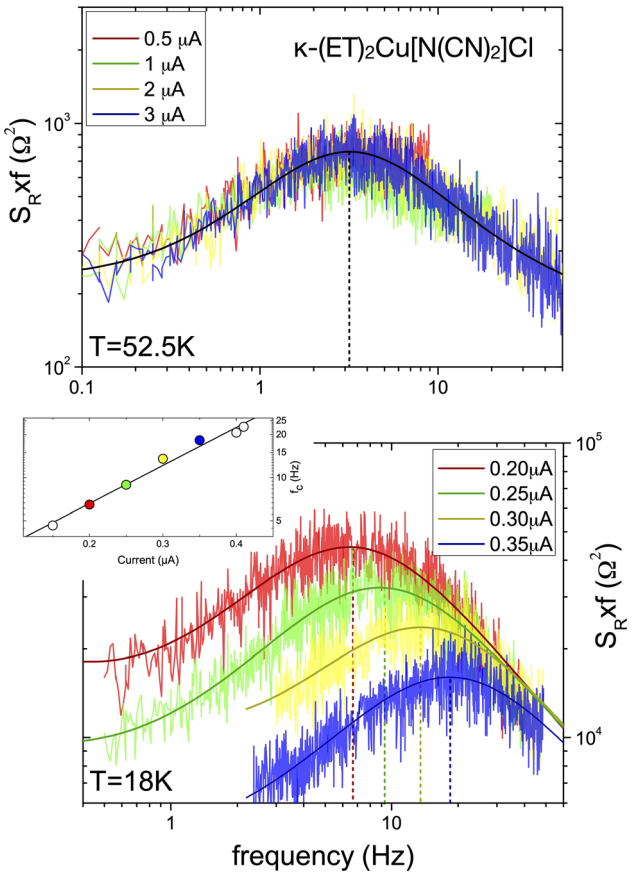

Fig. 38 Current dependence of the resistance noise PSD of κ-(ET)$_2$Cu[N(CN)$_2$]Cl, showing a characteristic Lorentzian contribution due to changes in the charge carrier dynamics, above (upper panel) and below (lower panel) the Néel temperature T_N, which—for samples showing long-range ferroelectric order—coincides with the ferroelectric transition at T_{FE}. The sample shown here is the same as the one discussed in Ref. 209, exhibiting relaxor-type ferroelectricity similar to β'-(ET)$_2$ICl$_2$. Figure reprinted with permission from Ref. 190.

breathing mode and the intra-dimer charge degrees of freedom. This is consistent with the drop in the intensity (Fig. 37c) and the decrease in the damping (Fig. 37a) below $T_N = T_{FE}$ = 25 K, as a decoupling of the modes is expected due to the critical slowing of the charge and spin fluctuations.

Fluctuation Spectroscopy

As outlined above, long-range ferroelectric order (suggested to be caused by charge ordering) of both order–disorder type[8] and relaxor-type ferroelectricity are observed for different samples.[49,209] Very similar to the behavior observed for β'-(ET)$_2$ICl$_2$ (Fig. 23 in Sect. "Conductance fluctuation (noise) spectroscopy"), Fig. 38 displays two-level fluctuations in κ-(ET)$_2$Cu[N(CN)$_2$]Cl, exhibiting a clear shift of the characteristic corner frequency f_c of a Lorentzian contribution superimposed on the

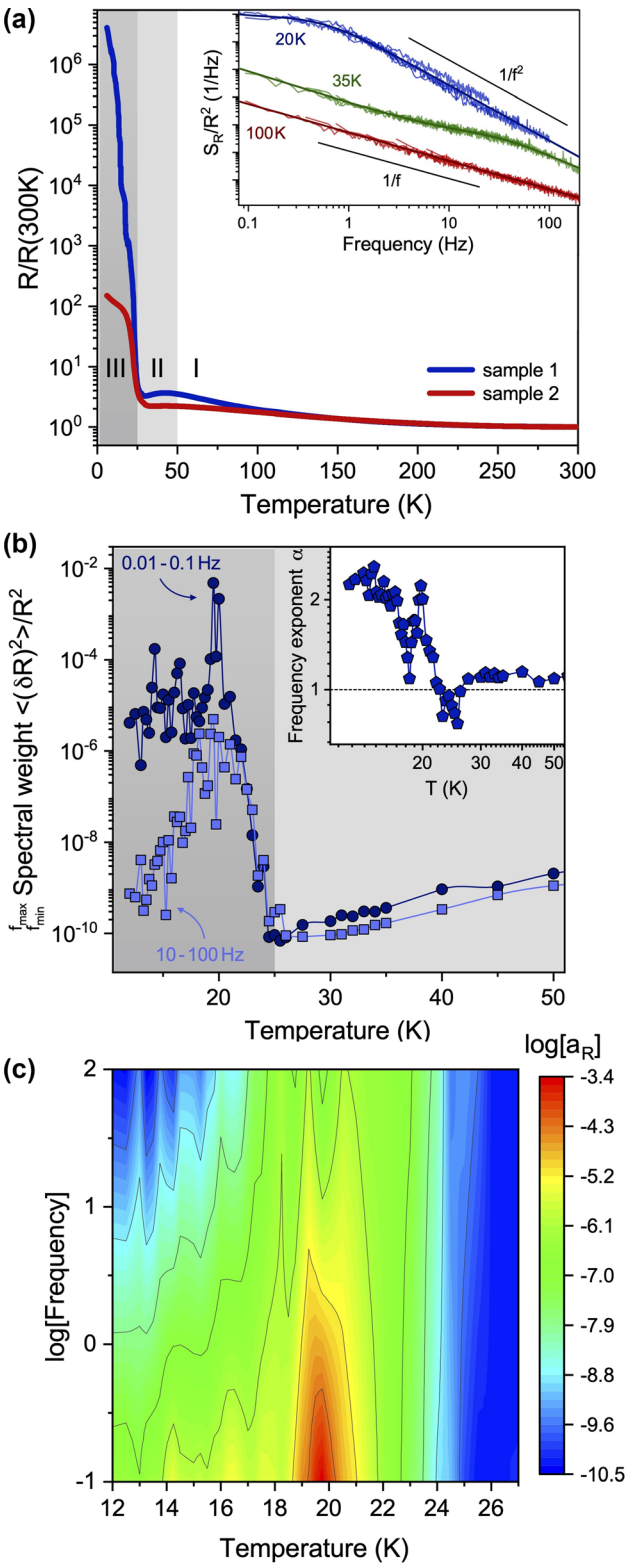

◀**Fig. 39** (a) Normalized $R(T)$ of two κ-BETS-Mn samples. The gray shaded regions correspond to the temperature regimes where pure $1/f$-type spectra (region I), $1/f$-type and superimposed Lorentzian spectra (region II) and spectra of $1/f^2$-type with a strong time dependence (region III) were observed. Inset: Typical fluctuation spectra (sample #1), shown as normalized resistance noise PSD, $S_R/R^2(f)$, in a double-logarithmic plot for selected temperatures representing regimes I, II, and III. Spectra are shifted for clarity. Different lines shown for each temperature are due to subsequent measurements of different frequency spans. Slopes $S_R/R^2 \propto 1/f$ and $\propto 1/f^2$ are indicated. Solid lines are fits to Eq. 5. (b) Spectral weight for different frequency ranges of sample 1 vs. T around the MI transition (light gray: regime II; dark gray: III). Inset: Frequency exponent α vs. temperature. (c) Contour plot of the relative noise level $a_R = f \times S_R/R^2$ in log scale vs. T vs. $\log f$. Figure adapted with permission from Ref. 107.

underlying $1/f$-type noise which is only seen for temperatures below T_{FE}. Similar to β'-$(ET)_2ICl_2$, from the shift of f_c with the electric field measured across the sample, a nanoscale size of the switching entity has been deduced, where at this temperature the threshold electric field (cf. Eq. 8) seems to be very small. Thus, the concept of PNR as precursors of relaxor-type electronic ferroelectricity, which can be probed by resistance or conductance noise spectroscopy, may be common to the organic CT salts prone to electronic ferroelectricity.

On the Nature of Relaxor-Type Ferroelectricity: The Case of κ-$(BETS)_2X$

A good candidate for electronic ferroelectricity is the system κ-$(BETS)_2Mn[N(CN)_2]_3$ (in short, κ-BETS-Mn). Although the compound hosts magnetic Mn^{2+} ions in the acceptor molecules, it has been inferred from different experiments[43,228,229] that the coupling between the BETS π- and the Mn d-electron spins is rather negligible. In theoretical *ab initio* calculations and modeling of magnetic torque and NMR measurements,[228,230] a spin-vortex-crystal order highlighting the importance of magnetic ring exchange[43] has been discussed. The system undergoes a transition from a metallic high-temperature phase to an insulating ground state at $T_{MI} \sim 20-25$ K caused by strong electron–electron interactions, consistent with band structure calculations,[231] revealing a narrow bandwidth and relatively strong dimerization of the BETS molecules. Quantum oscillation measurements under pressure[229,232] indicate strong electronic correlations suggesting a Mott instability as the origin of the metal–insulator (MI) transition. As for κ-$(ET)_2Cu[N(CN)_2]Cl$ (see Fig. 4 above), hydrostatic pressure induces a superconducting state, with $T_c = 5.7$ K at $p = 0.6$ kbar.[231] The metal–insulator transition in single crystals of κ-$(BETS)_2Mn[N(CN)_2]_3$ and the dynamics related to possible electronic ferroelectricity have recently been characterized in detail by studies of

thermal expansion, resistance fluctuation (noise) spectroscopy, and dielectric spectroscopy.[107] The combination of these spectroscopic methods is particularly useful in this compound exhibiting metallic behavior down to about 25 K such that the relatively high conductivity leads to pronounced non-intrinsic effects in the dielectric spectra (so-called Maxwell–Wagner relaxations).[233,234] Therefore, measurements of the dielectric constant are restricted to temperatures $T \lesssim T_{\mathrm{MI}}$ and are complemented by noise measurements performed at temperatures below and above T_{MI}. Due to the coupling of dielectric fluctuations to the sample's resistance, fluctuation spectroscopy is capable of detecting fluctuating polar entities on the nano-/mesoscopic scale.[157,190,191] The two complementary spectroscopies then reveal distinct low-frequency dynamics on different length scales, namely (i) an intrinsic relaxation that is typical for relaxor ferroelectrics which classifies the system as a possible new multiferroic, and (ii) two-level processes which we have identified as fluctuating PNR, i.e., clusters of quantum electric dipoles that fluctuate collectively.

Electrical Resistivity

Figure 39 shows the normalized resistance $R(T)/R(300\,\mathrm{K})$ of two κ-BETS-Mn samples, where sample 1 seems of better quality in terms of the magnitude of resistance change upon entering the insulating phase. Below a small local hump at about $T \sim 42\,\mathrm{K}$, the resistivity decreases upon cooling before it displays an abrupt increase by six orders of magnitude, marking the MI transition at $T_{\mathrm{MI}} \approx 22.5$ K defined by a peak in $\mathrm{d}\ln R/\mathrm{d}T$[235] (with the onset of the resistance increase at about 25 K). This coincides with the occurrence of AFM order at 21–23 K in NMR and specific heat measurements.[15,230,236]

Fluctuation (Noise) Spectroscopy

The inset of Fig. 39a presents resistance noise spectra across three distinct temperature regimes, each illustrating unique charge carrier dynamics. In the high-temperature regime (region I), the PSD of resistance noise displays pure 1/*f*-type behavior (red spectrum), which correlates with increased structural dynamics, which we will not discuss here. More complex charge carrier behavior becomes evident in the temperature range surrounding the MI transition. For temperatures above T_{MI} (region II, shown as a light gray shaded area), the resistance noise spectra exhibit Lorentzian profiles superimposed on the underlying 1/*f*-type noise (green spectrum). These two-level fluctuations are observed to strongly couple to the applied electric field and are therefore interpreted as fluctuating PNR.

In contrast, for temperatures below T_{MI} (region III, dark gray shaded area), enhanced Lorentzian profiles with a

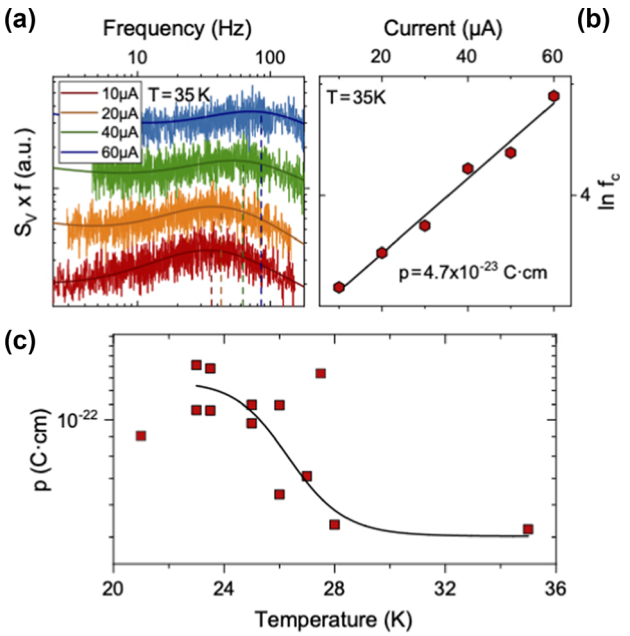

Fig. 40 (a) Lorentzian contribution in κ-$(BETS)_2Mn[N(CN)_2]_3$ shown as $S_V \times f$ vs. f for $T = 35$ K and different currents, revealing a shift of the corner frequency as illustrated in (b). The dipole moment, which is extracted from the slope of the linear fits according to Eq. 10 shown in (b), is displayed in (c) versus temperature. The black line is a guide to the eye. Figure adapted with permission from Ref. 107.

PSD scaling of $S_R/R^2 \propto 1/f^2$ for frequencies $f > 1$ Hz (blue spectrum) are observed. These profiles show dependence on both current and time, which suggests (1) a nonlinear coupling with the electric field and (2) nonequilibrium dynamics with spatial correlations, indicating the metastable nature of charge carrier dynamics. This metastability is further supported by second-spectrum measurements, $S^{(2)}(f_1,f_2)$, which reveal ergodicity breaking, as discussed in the following section.

Focusing initially on the 1/*f*-type component of the fluctuation spectra, without the Lorentzian contribution observed in regime III, Fig. 39b shows the spectral weight $\int_{f_{\min}}^{f_{\max}} S_R(f)/R^2 \mathrm{d}f$, representing the variance in the signal across two frequency bandwidths, $[0.01, 0.1\,\mathrm{Hz}]$ and $[10, 100\,\mathrm{Hz}]$, as a function of temperature. At these lower frequencies, the MI transition is marked by a dramatic increase in the noise PSD's spectral weight by several orders of magnitude, peaking sharply at approximately $T \sim 20\,\mathrm{K}$, especially pronounced for the lower frequency range $[0.01, 0.1\,\mathrm{Hz}]$. A striking observation is that upon further cooling, after a drastic increase by more than seven orders of magnitude, the noise level at these low frequencies saturates at a high level below the peak (about five orders of magnitude higher than at the onset of the transition), whereas the spectral weight for the

higher-frequency window [10, 100 Hz] decreases upon further cooling to a value comparable to that above the transition. Thus, the charge carrier dynamics below T_{MI} are dominated by rather slow fluctuations. The spectral weight of fluctuations with $S_R \propto 1/f^{\alpha}$ is reflected by the frequency exponent $\alpha(T) = -\partial \ln S_R(T)/\partial \ln f$, shown in the inset of Fig. 39b, where $\alpha = 1$ corresponds to a homogeneous distribution of the energies of fluctuators contributing to the 1/*f*-type noise, and $\alpha > 1$ and $\alpha < 1$ correspond to slower and faster fluctuations in comparison, respectively.[143] α strongly increases upon cooling through the MI transition, with a peak value $\alpha \sim 2$ at 20 K, indicating a strong shift of spectral weight to lower frequencies and a drastic slowing of the dynamics. A spectrum with $\alpha = 2$ indicates nonequilibrium dynamics and is typically associated with the high-frequency tail of a single Lorentzian (see the blue curve in the inset of Fig. 39a). This Lorentzian feature dominates fluctuations across the entire measured frequency range, suggesting that the system primarily switches between two states. The overall trend of increased noise levels and significant slowing of charge carrier dynamics is illustrated in a contour plot of the relative noise level $a_R = S_R/R^2 \times f$ (see Fig. 39c), shown as a function of temperature and frequency. The dimensionless parameter a_R, which reflects the intensity of fluctuations, begins to increase notably as the system is cooled below the MI transition onset at $T = 25$ K across all frequencies, peaking around T = 19–20 K. This noise peak is more prominent at lower frequencies (note the logarithmic scale for both a_R and *f*). At low temperatures, slow fluctuations dominate, whereas at higher frequencies, the noise level nearly returns to values observed above $T > T_{MI}$.

We now discuss the observed systematic nonlinear current dependence of the fluctuations for temperature regime II. Analyzing the observed Lorentzian spectra superimposed on the 1/*f*-type noise, we describe the fluctuations by Eq. 5 introduced above, at temperatures from 50 K down to the temperature of the noise peak below the onset of the MIT (regime II), shown exemplarily for spectra at $T = 35$ K in Fig. 40. In Fig. 40a we show $S_R/R^2 \times f$, thereby emphasizing the Lorentzian contribution with its maximum at the corner frequency f_c, versus the applied current representing the electric field $\mathcal{E}$ for a fixed temperature. For fixed current/electric field, the corner frequency versus temperature (not shown) exhibits an Arrhenius behavior with temperature, i.e., a thermally activated switching behavior with characteristic energies on the order of 20–90 meV at temperatures of 25–50 K.[107] We assign these two-level processes to clusters of quantum electric dipoles fluctuating collectively, i.e., PNR with a distribution of cluster sizes causing the range of activation energies observed at different temperatures.

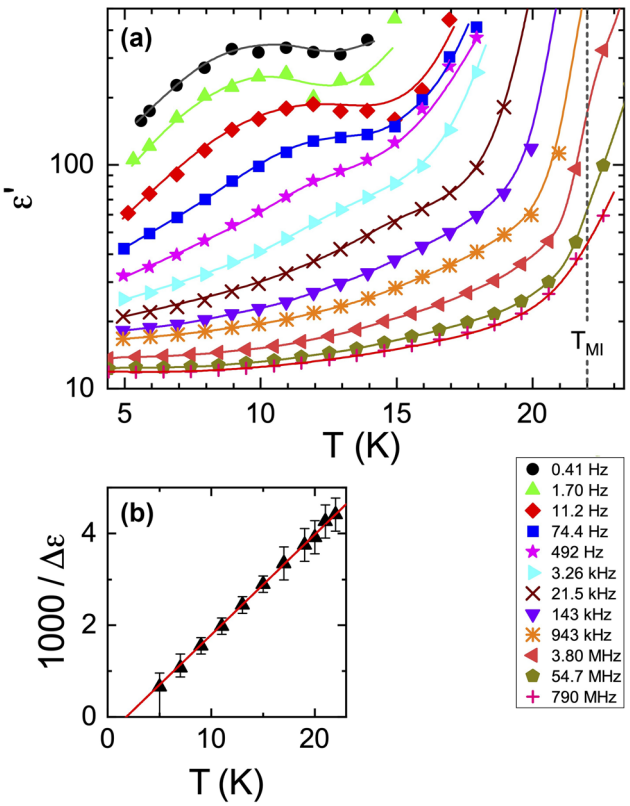

Fig. 41 (a) Temperature dependence of ε' of κ-$(BETS)_2Mn[N(CN)_2]_3$ measured at various frequencies. The onset temperature of the metal–insulator transition (22 K for this sample) is indicated by the vertical dashed line. The lines are guides for the eye. (b) Inverse relaxation strength of the intrinsic process at $T < T_{MI}$. The line indicates a Curie–Weiss law with $T_{CW} = 1.8$ K. Figure adapted with permission from Ref. 107.

The two-level (Lorentzian) fluctuations with characteristic frequency f_c shown in Fig. 39a and b at fixed temperature, however, strongly shift with the applied current to higher values, whereas their magnitude $b(T)$ is suppressed, very similar to previous observations in the square- and triangular-lattice Mott insulators and relaxor ferroelectrics β'-$(ET)_2ICl_2$[190] (Fig. 23), and κ-$(ET)_2Cu[N(CN)_2]Cl$ (Fig. 38), respectively. The linear increase observed in a plot $\ln f_c$ versus current (Fig. 39b) suggests that the thermally activated two-level processes depend on the dipole energy $E_{dipole} = p\mathcal{E}$ according to[190,191]

$$f_c = f_0 \exp\left(\frac{p\mathcal{E} - E_a}{k_B T}\right). \quad (10)$$

As for the compounds discussed above, the dipole moment p at a fixed temperature can be determined from the slope, yielding $p = 4.7 \cdot 10^{-23}$ C · cm at $T = 35$ K, where the electric field is calculated from the applied current, the temperature-dependent resistance, and the sample thickness.

Recent vibrational infrared spectroscopy measurements indeed revealed a splitting seen in $\nu_{27}(b_{1u})$ at very low temperatures as a signature of charge disproportionation in κ-$(BETS)_2Mn[N(CN)_2]_3$.[237] Although smaller than that observed for typical charge-ordering compounds of the BEDT-TTF family, the charge imbalance is significant and has been evaluated to $2\delta_\rho \approx 0.02\,e$. This corresponds to a fluctuating nanoscale polar region of radius ~ 3 nm for spherical PNR or ~ 5 nm for cylindrical PNR with the height of the unit cell (one molecular layer), which is comparable to though somewhat smaller than the PNR size estimated for β'-$(ET)_2ICl_2$ with $\delta \leq 0.1\,e$[126,190] (see Sect. "Quasi-1D $(TMTTF)_2X$"). The temperature evolution of p is displayed in Fig. 40c, revealing increasing values for decreasing temperatures, which appears to saturate below T_{MI}. The similarity to the temperature-dependent correlation length for PNR in the conventional displacive relaxor $Pb(Mg_{1/3}Nb_{2/3})O_3$ as determined from elastic diffuse neutron-scattering studies[238] is rather striking.

Dielectric Spectroscopy

Dielectric measurements have been performed in a broad frequency range $0.1\,\text{Hz} < \nu < 1.8$ GHz and at temperatures $T = 5$–300 K. However, above the MI transition, the rather high conductivity of κ-BETS-Mn gives rise to pronounced non-intrinsic contributions (so-called Maxwell–Wagner relaxations),[233,234] likely due to the generation of Schottky diodes at the electrode–sample interfaces (see Ref. 107 for a detailed discussion). These measurements provide complementary information to the resistance noise spectroscopy in several ways: Dielectric spectroscopy covers a broader frequency range and detects the dynamics of individual electric dipoles fluctuating in an AC electric field. Fluctuation spectroscopy is sensitive to the dynamics of larger-scale polar objects like PNR or domains, which couple to the resistivity. Moreover, dielectric spectroscopy requires a relatively insulating behavior of the measured material, whereas resistance noise spectroscopy works for sufficiently conducting samples.

Figure 41a shows the temperature dependence of the dielectric constant ε' at various frequencies for temperatures $T \lesssim T_{MI}$ (the pronounced increase in ε' at the highest temperatures arises from the onset of the Maxwell–Wagner relaxations mentioned above). The sigmoidal curve shape can be ascribed to an intrinsic relaxation process, shifting to lower temperatures with decreasing frequency. At the lowest frequencies, $\varepsilon'(T)$ exhibits a peak and reaches rather high values of several hundred. Aside from the mentioned non-intrinsic contributions, the overall behavior in Fig. 41a reveals the typical signatures of relaxor ferroelectricity (cf. Fig. 7c)[109,110]. Therefore, κ-$(BETS)_2Mn[N(CN)_2]_3$ can be regarded as another possible example of an organic multiferroic.

As discussed above, relaxor ferroelectricity, believed to arise from short-range, cluster-like ferroelectric order,[129,187,239] was also reported for various other CT salts.[13,49,102,103,116,127,197] For κ-BETS-Mn, the intrinsic nature of the detected relaxor behavior was checked by measuring several samples using two different experimental setups and different contact materials.[107] For further confirmation of relaxor ferroelectricity in κ-BETS-Mn polarization measurements as reported, e.g., in Refs. 103, 116, and 240, and as shown in Fig. 21 for β'-$(ET)_2ICl_2$,[126] would be desirable. However, due to the relatively high conductivity of this material[231,235] such measurements are impracticable.

In Ref. 107, the dielectric spectra of κ-BETS-Mn were fitted using an equivalent-circuit approach accounting for the aforementioned Maxwell–Wagner contributions. This enabled, e.g., the deduction of the relaxation strength $\Delta\varepsilon$ of the intrinsic, relaxor-like relaxation process. In Fig. 41b, the inverse of the obtained $\Delta\varepsilon(T)$ is shown. Its linear increase evidences Curie–Weiss behavior, $\Delta\varepsilon \propto 1/(T - T_{CW})$ with $T_{CW} = 1.8$ K. The latter provides an estimate of the quasi-static dipolar freezing temperature. It is even lower than the relatively low $T_{CW} = 6$ K reported for κ-$(ET)_2Cu_2(CN)_3$,[127] and it is significantly lower than the T_{CW} values between 35 K and 206 K found for other CT salts revealing relaxor ferroelectricity.[102,103,116,126]

We want to point out again that the relaxation processes detected by dielectric spectroscopy and resistance fluctuation mirror different microscopic processes, although their frequency and temperature ranges overlap. The latter can be ascribed to PNR switching, involving rather large effective energy barriers, which leads to relatively slow dynamics. The former reflect much faster, reorientational processes, occurring on smaller length scales than the dynamics of the whole PNR. Interestingly, the theoretical treatment in Ref. 241 assumes local polarization dynamics *inside* the PNR of relaxor ferroelectrics. Alternatively, faster dynamics in relaxor ferroelectrics may also be explained by motions of PNR boundaries as discussed by the breathing model.[242] Overall, the application of these complementary experimental methods to electronic ferroelectrics leads to a more comprehensive picture of the relaxation dynamics in these systems, which reveal emergent electronic phase separation due to disorder and/or competing interactions. Notably, the PNR are fluctuating units that an electric field can stabilize already above the MI transition. Thus, they can be regarded as precursors of the relaxor ferroelectricity observed below T_{MI}.

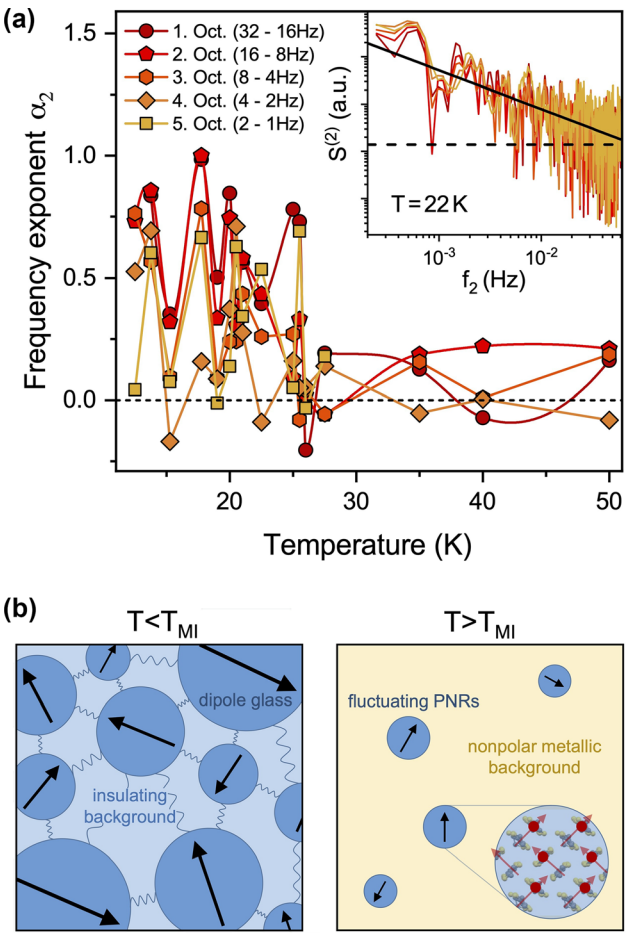

Fig. 42 (a) Frequency exponent α_2 of the second spectrum $S^{(2)} \propto 1/f_2^{\alpha_2}$ of κ-(BETS)$_2$Mn[N(CN)$_2$]$_3$ against temperature, which is extracted from a linear fit of the PSD in a double-logarithmic plot, as shown in the inset. Different red to orange colors mark different octaves. (b) Schematic illustration of the dipolar dynamics that lead to the observed behavior in the resistance noise and dielectric properties. Left: Frozen dipole-glass state below T_{MI} exhibiting relaxor-type ferroelectricity and strong nonequilibrium dynamics. Right: Polar nano-regions (PNR) preformed in the metallic phase above T_{MI}. Whereas above T_{MI}, the PNR are independently fluctuating, they exhibit spatial correlations in the insulating/ferroelectric regime (indicated by wavy lines). Figure reprinted with permission from Ref. 107.

Finally, we point out the unusual nonequilibrium dynamics and ergodicity breaking in the relaxor-ferroelectric phase. A sudden onset of a strong time dependence of the resistance/conductance noise PSD in the insulating state occurs below T_{MI}, which results in fluctuations that are no longer statistically stationary, i.e., variations in the spectral weight for repeated measurements at the same temperature. This so-called spectral wandering is reflected by a non-Gaussian probability distribution of the time signal, often caused by spatially correlated fluctuators.[151–154,243]

Probing Higher-Order Correlations by Measurements of the Second Spectrum

Below T_{MI}, we observe deviations from a Gaussian distribution (not shown) very similar to the dynamics of the first-order electronic phase transition in complex transition metal oxides,[244] which was ascribed to electronic phase separation. To identify interacting or spatially correlated fluctuators, we examined the higher-order correlation function by measuring the second spectrum $S^{(2)}(f_2, f_1, T)$, which represents the PSD of the fluctuating first spectrum. For a detailed explanation, refer to Refs. 148–150 and 245–247. Here, $f_1 \equiv f$ and f_2 denote the frequencies associated with the first and second spectra, respectively, where f_2 arises from the time dependence of $S(f, T) \equiv S^{(1)}(f_1, t)$ at fixed frequency f_1. In systems with correlated fluctuators, the second spectrum often displays a frequency dependence following $S^{(2)} \propto 1/f_2^{\alpha_2}$, with $\alpha_2 > 0$, while for statistically stationary Gaussian fluctuations, $\alpha_2 = 0$.[145] The inset of Fig. 42a shows a typical $S^{(2)}(f_2)$ spectrum at $T = 22$ K, exhibiting a $S^{(2)} \propto 1/f_2$ behavior (black line).

The second spectrum, analyzed across different octave bands (highlighted in red to orange in Fig. 42a), corresponds to varying frequency ranges of the first spectrum.[107] Notably, $S^{(2)}$ remains largely frequency-independent ($\alpha_2 \sim 0$) above the MI transition. However, a sharp increase in the frequency exponent, reaching $\alpha_2 \sim 1$, is observed as the sample is cooled through T_{MI}, which coincides with the strong increase in slow fluctuations, $S^{(1)}(f_1)$, shown in Fig. 39 above. These observations suggest that the MI transition is accompanied by the emergence of pronounced nonequilibrium charge dynamics, indicative of spatially correlated fluctuators and dipolar glass behavior.

Proposed Scenario for the Dynamics of Electric Dipoles

The following tentative scenario is proposed to describe the dynamics of the electric dipoles on the (BETS)$_2$ dimers. As the temperature approaches T_{MI} from above, strong electron–electron interactions cause the π-holes to localize on the dimers, driving the system into a Mott insulating state. This localization leads to a sharp rise in both resistance and resistance noise. Nevertheless, within each dimer, the holes remain delocalized between the two molecules, and their hopping between these molecules causes the reorientation of an associated dipole moment, which is observed through dielectric spectroscopy.

As the temperature decreases, this local motion begins to slow, and simultaneously, local ferroelectric correlations—which have already partially developed above T_{MI}—give rise to a cluster-like ferroelectric order characteristic of relaxor ferroelectrics. Upon cooling through the

metal–insulator transition, the polar nano-regions, which dominate the resistance noise and preexist as fluctuating entities above T_{MI}, transition into a system of interacting two-level systems. The sudden and significant change in the statistical properties of these fluctuations, along with the onset of nonequilibrium dynamics—an indicator of spatial correlations[151–154,243]—appears precisely at the onset of the MI transition. This can be attributed to a transformation in the background matrix: above T_{MI}, the matrix is metallic, providing screening for the dipole moments; below T_{MI}, however, the insulating background allows the PNR to interact (see Fig. 42b for a schematic illustration).

The pronounced increase in noise magnitude S_R/R^2 at low frequencies (below approximately 1 kHz), as shown in Fig. 39b and c, is indicative of a first-order phase transition, accompanied by emerging electronic phase separation.[244,248,249] The enhancement of the frequency exponent α, reflecting a significant shift in spectral weight towards lower frequencies and a slowing in charge carrier dynamics that persists at low temperatures, aligns with the localization of charge carriers and the onset of the freezing of PNR switching.

In contrast to typical relaxors, where correlated dipolar dynamics result from ionic motion and display glass-like freezing upon further cooling,[109,110,129] in κ-BETS-Mn, tunneling starts to dominate at low temperatures,[107] preventing the further slowing and final arrest of the essentially electronic dynamics. This tunneling effect likely explains the saturation in noise level and the persistence of slow dynamics at low frequencies and temperatures.

Epilogue

In this review, we have discussed the ferroelectric and multiferroic properties of organic CT salts. The main focus has been on the more recent developments in the field, covering the quasi-2D systems of the (BEDT-TTF)$_2X$ and (BETS)$_2X$ varieties. These studies have followed the seminal work on the quasi-1D (TMTTF)$_2X$ systems where ferroelectricity was well established. The charge-order-driven polar state observed in the latter systems represents a prime example for electronic ferroelectricity which is controlled by electronic degrees of freedom, instead of the shifts of atomic positions as in conventional displacive ferroelectrics.

It has turned out that due to their molecular degrees of freedom, involving electronic states extending over arrays of molecules, correlated 2D organic CT salts close to a Mott- or charge-order metal–insulator transition are prone to a particular type of electronic ferroelectricity, where the polar state is caused by charge disproportionation in a modulated or bond-alternated dimerized lattice of organic donor molecules. Here the centrosymmetric dimer-Mott state features a single π-hole with spin 1/2, whose center of gravity is localized at the midpoint of the molecular dimer unit $(ET)_2$, representing a charge-centered or charge-averaged phase. However, if the charge shifts toward one of the molecules within the dimer, resulting in a charge-ordered phase, this imbalance gives rise to a quantum electric dipole. Unlike canonical ferroelectrics, where ions are involved, the much lighter mass of electrons in charge-driven ferroelectrics can enable significantly faster switching processes.

The proof of ferroelectricity in the various classes of organic CT salts has been based on a combination of different experimental probes often initiated and accompanied by theoretical considerations.

On the experimental side, dielectric spectroscopy, although often experimentally challenging to apply to organic CT salts, has become a most successful tool for studying the response to AC electric fields and exploring the ferroelectric properties. Clear evidence for order–disorder-type electronic ferroelectricity has been revealed for κ-$(ET)_2Cu[N(CN)_2]Cl$ and κ-$(ET)_2Hg(SCN)_2Cl$. Whereas the polar order in both cases is driven by CO, in the former compound the CO is weaker in magnitude and emerges within the Mott insulating state, remarkably occurring simultaneously with long-range antiferromagnetic order. In the latter compound, CO and ferroelectricity coincide with the metal–insulator transition. A similar strong charge-order-based scenario was found for θ-$(BEDT\text{-}TTF)_2RbZn(SCN)_4$.

A relaxor-type ferroelectric response, indicative of interacting electric dipoles in the presence of a random potential or competing interactions, is more prevalent and was first observed in κ-$(ET)_2Cu_2(CN)_3$. Similarly, relaxor-type ferroelectricity occurs in other κ-$(ET)_2X$ compounds, such as $X = Ag_2(CN)_3$, as well as in systems with different packing motifs or donor molecules, like β'-$(ET)_2ICl_2$, α-$(ET)_2I_3$, and various $Pd(dmit)_2$ systems.

Structural aspects like lattice deformation accompanying the ferroelectric transition as well as the lattice dynamics coupled to the charge and/or spin degrees of freedom have been investigated by thermal expansion measurements and inelastic neutron scattering, respectively. Infrared spectroscopy and Raman scattering have played an important role in determining possible charge disproportionations on the molecules.

From theoretical considerations, it is expected that the intra-dimer electron mobility leads to large temporal and spatial dielectric fluctuations, which may play a critical role in the dielectric and optical properties, as well as in the

ferroelectric phase transition. In this context, resistance or conductance fluctuation (noise) spectroscopy are an ideal complement to dielectric spectroscopy, since the former measurements reveal additional information on fluctuating polar entities of different length and time scales and thus the physics underlying electronic ferroelectricity, and at temperatures where samples are too conductive for dielectric measurements. Comparing the results of different organic CT salts reveals striking similarities regarding the formation of PNR or fluctuating mesoscopic domains and their interaction with electric fields. These results suggest that fluctuating PNR, sometimes stabilized in electric fields at temperatures above the coherent localization/ordering of charges, may be a common characteristic of electronic ferroelectricity of relaxor type in molecular materials. Likewise, strong nonequilibrium dynamics and ergodicity breaking at low temperatures consistent with droplet models in spin glasses[107] have been observed in different systems.

Multiferroicity, the simultaneous ordering of both electric and magnetic dipoles, is observed in a few organic salts with weak magnitudes of CO, including κ-$(ET)_2Cu[N(CN)_2]Cl$. Microscopically, the primary mechanism for the interplay between charge and spin orders is the modification of the effective magnetic couplings by charge disproportionation between different molecules. This mechanism differs from other multiferroics, often based on displacive ferroelectricity where distortions of the ions themselves lead to electric polarization and modification of the magnetic couplings. As such, mechanisms such as the inverse Dzyaloshinskii–Moriya are not relevant in organic CT salts. Instead, it is the modification of the magnitudes of isotropic couplings that serves as the primary mechanism of magnetoelectric coupling. For strong CO, the resulting magnetic couplings typically become increasingly one-dimensional, likely leading to competition between charge and magnetic orders. For weak CO, the reduction of symmetry may lead to a relief of magnetic frustration, promoting magnetic order. The coupling of the charge and spin degrees of freedom leads to a variety of effects, such as inhomogeneous magnetic responses in charge glass states.

Outlook

Clearly, the observation of ferroelectric order driven by electronic degrees of freedom has added another dimension to the research on molecular systems in general and organic CT salts in particular. Salts with quarter-filled conduction bands, by their design, are prone to ordering phenomena in the charge sector, and clear signatures of electronic ferroelectricity have been found in numerous salts. Surprisingly, as illustrated in this review article, this happens to be true also for various dimerized salts, often considered as half-filled dimer-Mott systems, where the polar order is assigned to intra-dimer charge degrees of freedom. While this notion has now been widely accepted, detailed investigations of this peculiar electronic type of ferroelectricity and its properties are still in their infancy. Future work has to explore in more detail the static and dynamical properties of the polar state that is formed by a system of correlated electrons. Of particular interest will be the high-frequency response of the polar order, especially the possibility of fast switching and phase control. Moreover, it will be of great importance to study the coupling to the lattice degrees of freedom, and the influence of geometrical frustration, which thanks to the advent of experiments under uniaxial strain can be varied deliberately. In this regard it is also crucial to better understand the character and properties of polar nano-regions and their role in the formation of relaxor-type ferroelectricity. Likewise, future research should focus on a better understanding of the multiferroic properties revealed in a few salts. The peculiar magnetoelectric coupling proposed to be at work here—the modification of the materials' magnetic couplings via charge disproportionation—should be explored in more depth. It is of fundamental interest to investigate to what extent one type of order can be manipulated by the application of the conjugated field of the other type. While the research activities along these lines are primarily driven by basic science, the wish for transitioning the ferroelectric and multiferroic properties into technical applications is obvious. The challenge here will be to design and synthesize a proper CT salt where the charge disproportionation and accompanying ferroelectricity occur at room temperature, ideally in coexistence with magnetic order.

Acknowledgements We acknowledge support from the Deutsche Forschungsgemeinschaft (DFG, German Research Foundation) through the Transregional Collaborative Research Center TRR 288-422213477 (projects A06 and B02). Work in Augsburg was supported by the DFG through TRR 80.

Funding Open Access funding enabled and organized by Projekt DEAL.

Conflict of interest The authors declare that they have no conflict of interest.

References

1. Seo, H., C. Hotta, and H. Fukuyama. 2004. Toward systematic understanding of diversity of electronic properties in low-dimensional molecular solids. *Chem. Rev.* 104(11): 5005.
2. Toyota, N., M. Lang, and J. Müller. 2007. *Low-dimensional molecular metals: solid state science*. Berlin: Springer.
3. Powell, B.J. and R.H. McKenzie. 2011. Quantum frustration in organic Mott insulators: from spin liquids to unconventional superconductors. *Rep. Prog. Phys.* 74: 056501.
4. Kanoda, K. and R. Kato. 2011. Mott physics in organic conductors with triangular lattices. *Annu. Rev. Condens. Matter Phys.* 2(1): 167.
5. Clay, R.T. and S. Mazumdar. From charge- and spin-ordering to superconductivity in the organic charge-transfer solids. *Physics Reports*, pages 1–89.
6. van den Brink, J. and D.I. Khomskii. 2008. Multiferroicity due to charge ordering. *J. Phys. Condens. Matter* 20(43): 434217.
7. Ishihara, S. 2010. Electronic ferroelectricity and frustration. *J. Phys. Soc. Jpn.* 79(1): 011010.
8. Lunkenheimer, P., J. Müller, S. Krohns, F. Schrettle, A. Loidl, B. Hartmann, R. Rommel, M. de Souza, C. Hotta, J.A. Schlueter, and M. Lang. 2012. Multiferroicity in an organic charge-transfer salt that is suggestive of electric-dipole-driven magnetism. *Nat. Mater.* 11(9): 755.
9. Ikeda, N., H. Ohsumi, K. Ohwada, K. Ishii, T. Inami, K. Kakurai, Y. Murakami, K. Yoshii, S. Mori, Y. Horibe, and H. Kitô. 2005. Ferroelectricity from iron valence ordering in the charge-frustrated system $LuFe_2O_4$. *Nature* 436(7054): 1136.
10. Spaldin, N.A. and R. Ramesh. 2019. Advances in magnetoelectric multiferroics. *Nat. Mater.* 18(3): 203.
11. Nad, F., P. Monceau, C. Carcel, and J.M. Fabre. 2000. Dielectric response of the charge-induced correlated state in the quasi-one-dimensional conductor $(TMTTF)_2PF_6$. *Phys. Rev. B* 62(3): 1753.
12. Monceau, P., F. Nad, and S. Brazovskii. 2001. Ferroelectric Mott–Hubbard phase of organic $(TMTTF)_2X$ conductors. *Phys. Rev. Lett.* 86(18): 4080.
13. Lunkenheimer, P. and A. Loidl. 2015. Dielectric spectroscopy on organic charge-transfer salts. *J. Phys. Condens. Matter* 27(37): 373001.
14. Tomić, S. and M. Dressel. 2015. Ferroelectricity in molecular solids: a review of electrodynamic properties. *Rep. Prog. Phys.* 78(9): 096501.
15. Riedl, K., E. Gati, and R. Valentí. 2022. Ingredients for generalized models of κ-phase organic charge-transfer salts: a review. *Crystals* 12(12): 1689.
16. Su, S.-Q., S.-Q. Wu, S. Kanegawa, K. Yamamoto, and O. Sato. 2023. Control of electronic polarization via charge ordering and electron transfer: electronic ferroelectrics and electronic pyroelectrics. *Chem. Sci.* 14: 10631.
17. Fujiwara, K., Y. Fukada, Y. Okuda, R. Seimiya, N. Ikeda, K. Yokoyama, H. Yu, S. Koshihara, and Y. Okimoto. 2021. Direct evidence of electronic ferroelectricity in $YbFe_2O_4$ using neutron diffraction and nonlinear spectroscopy. *Sci. Rep.* 1: 4277.
18. Konishi, S., D. Urushihara, T. Hayakawa, K. Fukuda, T. Asaka, K. Ishii, N. Naoda, M. Okada, H. Akamatsu, H. Hojo, M. Azuma, and K. Tanaka. 2023. Confirmation of ferroelectricity, piezoelectricity, and crystal structure of the electronic dielectric $TmFe_2O_4$. *Phys. Rev. B* 108: 014105.
19. Gui, Z., W. Li, and L. Huang. 2024. The dynamics of charge-density waves. *Nano Lett.* 24: 3231.
20. Sadhukhan, P., S.-Q. Wu, S. Kanegawa, S.-Q. Su, X. Zhang, T. Nakanishi, J.I. Long, K. Gao, R. Shimada, H. Okajima, A. Sakamoto, J.G. Chiappella, M.S. Huzan, T. Kroll, D. Sokaras, M.L. Baker, and O. Sato. 2023. Energy conversion and storage via photoinduced polarization change in non-ferroelectric molecular [coga] crystals. *Nat. Commun.* 14(1): 3394.
21. Huang, Y.-B., J.-Q. Li, W.-H. Xu, W. Zheng, X. Zhang, K.-G. Gao, T. Ji, T. Ikeda, T. Nakanishi, S. Kanegawa, S.-Q. Wu, S.-Q. Su, and O. Sato. 2024. Electrically detectable photoinduced polarization switching in a molecular Prussian blue analogue. *J. Am. Chem. Soc.* 146(1): 201.
22. Kanoda, K. 1997. Recent progress in NMR studies on organic conductors. *Hyperfine Interact.* 104(1–4): 235.
23. Limelette, P., P. Wzietek, S. Florens, A. Georges, T.A. Costi, C. Pasquier, D. Jérome, C. Mézière, and P. Batail. 2003. Mott transition and transport crossovers in the organic compound κ-$(BEDT\text{-}TTF)_2Cu[N(CN)_2]Cl$. *Phys. Rev. Lett.* 91(1): 016401.
24. Fournier, D., M. Poirier, M. Castonguay, and K.D. Truong. 2003. Mott transition, compressibility divergence, and the *P-T* phase diagram of layered organic superconductors: an ultrasonic investigation. *Phys. Rev. Lett.* 90(12): 127002.
25. Kagawa, F., K. Miyagawa, and K. Kanoda. 2005. Unconventional critical behaviour in a quasi-two-dimensional organic conductor. *Nature* 436(7050): 534.
26. Kagawa, F., K. Miyagawa, and K. Kanoda. 2009. Magnetic Mott criticality in a κ-type organic salt probed by NMR. *Nat. Phys.* 5(12): 880.
27. Furukawa, T., K. Miyagawa, H. Taniguchi, R. Kato, and K. Kanoda. 2015. Quantum criticality of Mott transition in organic materials. *Nat. Phys.* 11(3): 221.
28. Isono, T., T. Terashima, K. Miyagawa, K. Kanoda, and S. Uji. 2016. Quantum criticality in an organic spin-liquid insulator κ-$(BEDT\text{-}TTF)_2Cu_2(CN)_3$. *Nat. Commun.* 7: 13494.
29. Gati, E., M. Garst, R.S. Manna, U. Tutsch, B. Wolf, L. Bartosch, H. Schubert, T. Sasaki, J.A. Schlueter, and M. Lang. 2016. Breakdown of Hooke's law of elasticity at the Mott critical endpoint in an organic conductor. *Sci. Adv.* 2(12): e1601646.
30. Guterding, D., S. Diehl, M. Altmeyer, T. Methfessel, U. Tutsch, H. Schubert, M. Lang, J. Müller, M. Huth, H.O. Jeschke, R. Valentí, M. Jourdan, and H.-J. Elmers. 2016. Evidence for eight-node mixed-symmetry superconductivity in a correlated organic metal. *Phys. Rev. Lett.* 116(23): 237001.
31. Wosnitza, J. 2019. Superconductivity of organic charge-transfer salts. *J. Low Temp. Phys.* 197(3–4): 250–271.
32. Furukawa, T., K. Miyagawa, M. Matsumoto, T. Sasaki, and K. Kanoda. 2023. Microscopic evidence for preformed cooper pairs in pressure-tuned organic superconductors near the Mott transition. *Phys. Rev. Res.* 5: 023165.
33. Shimizu, Y., K. Miyagawa, K. Kanoda, M. Maesato, and G. Saito. 2003. Spin liquid state in an organic Mott insulator with a triangular lattice. *Phys. Rev. Lett.* 91: 107001.
34. Riedl, K., R. Valentí, and S.M. Winter. 2019. Critical spin liquid versus valence-bond glass in a triangular-lattice organic antiferromagnet. *Nat. Commun.* 10(1): 2561.
35. Pustogow, A., E. Zhukova, B. Gorshunov, M. Pinterić, S. Tomić, J. A. Schlueter, and M. Dressel. 2014. Low-Energy Excitations in the Quantum Spin-Liquid κ-$(BEDT\text{-}TTF)_2Cu_2(CN)_3$. arXiv:1412.4581.
36. Gati, E., J.K.H. Fischer, P. Lunkenheimer, D. Zielke, S. Köhler, F. Kolb, H.-A. Krug, S.M. von Nidda, H.S. Winter, J.A. Schlueter, H.O. Jeschke, R. Valentí, and M. Lang. 2018. Evidence for electronically driven ferroelectricity in a strongly correlated dimerized BEDT-TTF molecular conductor. *Phys. Rev. Lett.* 120: 247601.

37. Miyagawa, K., A. Kawamoto, Y. Nakazawa, and K. Kanoda. 1995. Antiferromagnetic ordering and spin structure in the organic conductor κ-(BEDT-TTF)$_2$Cu[N(CN)$_2$]Cl. *Phys. Rev. Lett.* 75(6): 1174.
38. Lefebvre, S., P. Wzietek, S. Brown, C. Bourbonnais, D. Jérome, C. Mézière, M. Fourmigué, and P. Batail. 2000. Mott transition, antiferromagnetism, and unconventional superconductivity in layered organic superconductors. *Phys. Rev. Lett.* 85(25): 5420.
39. Kagawa, F., T. Itou, K. Miyagawa, and K. Kanoda. 2004. Transport criticality of the first-order Mott transition in the quasi-two-dimensional organic conductor κ-(BEDT-TTF)$_2$Cu[N(CN)$_2$]Cl. *Phys. Rev. B* 69(6): 064511.
40. Koretsune, T. and C. Hotta. 2014. Evaluating model parameters of the κ- and β'-type Mott insulating organic solids. *Phys. Rev. B* 89(4): 045102.
41. Guterding, D., R. Valentí, and H.O. Jeschke. 2015. Influence of molecular conformations on the electronic structure of organic charge transfer salts. *Phys. Rev. B* 92: 081109.
42. Gati, E., S.M. Winter, J.A. Schlueter, H. Schubert, J. Müller, and M. Lang. 2018. Insights from experiment and ab initio calculations into the glasslike transition in the molecular conductor κ-(BEDT-TTF)$_2$Hg(SCN)$_2$Cl. *Phys. Rev. B* 7: 075115.
43. Riedl, K., E. Gati, D. Zielke, S. Hartmann, O.M. Vyaselev, N.D. Kushch, H.O. Jeschke, M. Lang, R. Valentí, M.V. Kartsovnik, and S.M. Winter. 2021. Spin vortex crystal order in organic triangular lattice compound. *Phys. Rev. Lett.* 127: 147204.
44. Komatsu, T., N. Matsukawa, T. Inoue, and G. Saito. 1996. Realization of superconductivity at ambient pressure by band-filling control in κ-(BEDT-TTF)$_2$Cu$_2$(CN)$_3$. *J. Phys. Soc. Jpn.* 65(5): 1340.
45. Kandpal, H.C., I. Opahle, Y.-Z. Zhang, H.O. Jeschke, and R. Valentí. 2009. Revision of model parameters for κ-type charge transfer salts: an ab initio study. *Phys. Rev. Lett.* 103(6): 067004.
46. Toledano, P., H. Schmid, M. Clin, and J.P. Rivera. 1985. Theory of the low-temperature phases in boracites: latent antiferromagnetism, weak ferromagnetism, and improper magnetostructural couplings. *Phys. Rev. B* 32(9): 6006.
47. Mostovoy, M. 2006. Ferroelectricity in spiral magnets. *Phys. Rev. Lett.* 96(6): 067601.
48. Eerenstein, W., N.D. Mathur, and J.F. Scott. 2006. Multiferroic and magnetoelectric materials. *Nature* 442(7104): 759.
49. Lang, M., P. Lunkenheimer, J. Müller, A. Loidl, B. Hartmann, N.H. Hoang, E. Gati, H. Schubert, and J.A. Schlueter. 2014. Multiferroicity in the Mott insulating charge-transfer salt κ-(BEFT-TTF)$_2$Cu[N(CN)$_2$]Cl. *IEEE Trans. Magn.* 50(6): 1.
50. Hassan, N.M., K. Thirunavukkuarasu, Z. Lu, D. Smirnov, E.I. Zhilyaeva, S. Torunova, R.N. Lyubovskaya, and N. Drichko. 2020. Melting of charge order in the low-temperature state of an electronic ferroelectric-like system. *NPJ Quantum Mater.* 5(1): 15.
51. Naka, M. and S. Ishihara. 2010. Electronic ferroelectricity in a Dimer Mott insulator. *J. Phys. Soc. Jpn.* 79(6): 063707.
52. Shinaoka, H., T. Misawa, K. Nakamura, and M. Imada. 2012. Mott transition and phase diagram of κ-(BEFT-TTF)$_2$Cu(NCS)$_2$ studied by two-dimensional model derived from ab initio method. *J. Phys. Soc. Jpn.* 81(3): 034701.
53. Kaneko, R., L.F. Tocchio, R. Valentí, and F. Becca. 2017. Charge orders in organic charge-transfer salts. *New J. Phys.* 19(10): 103033.
54. Watanabe, H., H. Seo, and S. Yunoki. 2017. Phase competition and superconductivity in κ-(BEDT-TTF)$_2$X: importance of intermolecular Coulomb interactions. *J. Phys. Soc. Jpn.* 86(3): 033703.
55. Ueda, A., S. Yamada, T. Isono, H. Kamo, A. Nakao, R. Kumai, H. Nakao, Y. Murakami, K. Yamamoto, Y. Nishio, et al. 2014. Hydrogen-bond-dynamics-based switching of conductivity and magnetism: a phase transition caused by deuterium and electron transfer in a hydrogen-bonded purely organic conductor crystal. *J. Am. Chem. Soc.* 136(34): 12184.
56. Hotta, C. 2010. Quantum electric dipoles in spin-liquid dimer Mott insulator κ-(ET)$_2$Cu$_2$(CN)$_3$. *Phys. Rev. B* 82(24): 241104(R).
57. Hotta, C. 2012. Theories on frustrated electrons in two-dimensional organic solids. *Crystals* 2: 1155.
58. Naka, M. and S. Ishihara. 2016. Quantum melting of magnetic order in an organic dimer Mott-insulating system. *Phys. Rev. B* 93(19): 195114.
59. Jacko, A.C., E.P. Kenny, and B.J. Powell. 2020. Interplay of dipoles and spins in κ-(BEDT-TTF)$_2$X, where X = Hg(SCN)$_2$Cl, Hg(SCN)$_2$Br, Cu[N(CN)$_2$]Cl, Cu[N(CN)$_2$]Br, and Ag$_2$(CN)$_3$. *Phys. Rev. B* 101(12): 125110.
60. Ishihara, S. 2014. Electronic ferroelectricity in molecular organic crystals. *J. Phys. Condens. Matter* 26(49): 493201.
61. Hotta, C., T. Yoshida, and K. Harada. 2023. Quantum critical dynamics in the two-dimensional transverse Ising model. *Phys. Rev. Res.* 5: 013186.
62. Le, T., A. Pustogow, J. Wang, A. Henderson, T. Siegrist, J.A. Schlueter, and S.E. Brown. 2020. Disorder and slowing magnetic dynamics in κ-(BEDT-TTF)$_2$Hg(SCN)Br. *Phys. Rev. B* 102(18): 184417.
63. Pustogow, A., T. Le, H.-H. Wang, E. Yongkang Luo, H. Schubert Gati, M. Lang, and S.E. Brown. 2020. Impurity moments conceal low-energy relaxation of quantum spin liquids. *Phys. Rev. B* 101(14): 140401.
64. Urai, M., K. Miyagawa, Y. Watanabe, E.I. Zhilyaeva, S.A. Torunova, R.N. Lyubovskaya, N. Drichko, and K. Kanoda. 2022. Anomalously field-susceptible spin clusters emerging in the electric-dipole liquid candidate κ-(ET)$_2$Hg(SCN)$_2$Br. *Sci. Adv.* 8(51): eabn1680.
65. Hemmida, M., H.-A. Krug von Nidda, B. Miksch, L.L. Samoilenko, A. Pustogow, S. Widmann, A. Henderson, T. Siegrist, J.A. Schlueter, A. Loidl, and M. Dressel. 2018. Weak ferromagnetism and glassy state in κ-(BEDT-TTF)$_2$Hg(SCN)Br. *Phys. Rev. B* 98(24): 241202.
66. Yamashita, M., S. Sugiura, A. Ueda, S. Dekura, T. Terashima, S. Uji, Y. Sunairi, H. Mori, E.I. Zhilyaeva, S.A. Torunova, et al. 2021. Ferromagnetism out of charge fluctuation of strongly correlated electrons in κ-(BEDT-TTF)$_2$Hg(SCN)Br. *NPJ Quantum Mater.* 6(1): 87.
67. Drichko, N., S. Sugiura, M. Yamashita, A. Ueda, S. Uji, N. Hassan, Y. Sunairi, H. Mori, E.I. Zhilyaeva, S. Torunova, et al. 2022. Charge and spin interplay in a molecular-dimer-based organic Mott insulator. *Phys. Rev. B* 106(6): 064202.
68. Deglint, M.B., K. Akella, and M.P. Kennett. 2022. Charge glass in an extended dimer Hubbard model. *Phys. Rev. B* 106: 085123.
69. Seo, H. 2000. Charge ordering in organic ET compounds. *J. Phys. Soc. Jpn.* 69(3): 805.
70. Kaneko, M. and M. Ogata. 2006. Mean-field study of charge order with long periodicity in θ-(BEDT-TTF)$_2$X. *J. Phys. Soc. Jpn.* 75(1): 014710.
71. McKenzie, R.H., J. Merino, J.B. Marston, and O.P. Sushkov. 2001. Charge ordering and antiferromagnetic exchange in layered molecular crystals of the θ type. *Phys. Rev. B* 64(8): 085109.
72. Kuroki, K. 2006. The origin of the charge ordering and its relevance to superconductivity in θ-(BEDT-TTF)$_2$X: the effect of the Fermi surface nesting and the distant electron–electron interactions. *J. Phys. Soc. Jpn.* 75(11): 114716.
73. Watanabe, H. and M. Ogata. 2006. Novel charge order and superconductivity in two-dimensional frustrated lattice at quarter filling. *J. Phys. Soc. Jpn.* 75(6): 063702.

74. Merino, J., H. Seo, and M. Ogata. 2005. Quantum melting of charge order due to frustration in two-dimensional quarter-filled systems. *Phys. Rev. B* 71(12): 125111.
75. Nishimoto, S., M. Shingai, and Y. Ohta. 2008. Coexistence of distinct charge fluctuations in θ-(BEDT-TTF)$_2$X. *Phys. Rev. B* 78(3): 035113.
76. Hotta, C. and N. Furukawa. 2006. Strong coupling theory of the spinless charges on triangular lattices: possible formation of a gapless charge-ordered liquid. *Phys. Rev. B* 74(19): 193107.
77. Hotta, C., N. Furukawa, A. Nakagawa, and K. Kubo. 2006. Phase diagram of spinless fermions on an anisotropic triangular lattice at half-filling. *J. Phys. Soc. Jpn.* 75(12): 123704.
78. Seo, H., K. Tsutsui, M. Ogata, and J. Merino. 2006. Charge fluctuations in geometrically frustrated charge ordering system. *J. Phys. Soc. Jpn.* 75(11): 114707.
79. Udagawa, M. and Y. Motome. 2007. Charge ordering and coexistence of charge fluctuations in quasi-two-dimensional organic conductors θ-(BEDT-TTF)$_2$X. *Phys. Rev. Lett.* 98(20): 206405.
80. Tanaka, Y. and K. Yonemitsu. 2007. Effects of electron-lattice coupling on charge order in θ-(ET)$_2$X. *J. Phys. Soc. Jpn.* 76(5): 053708.
81. Miyashita, S. and K. Yonemitsu. 2007. Charge ordering in θ-(BEDT-TTF)$_2$RbZn(SCN)$_4$: cooperative effects of electron correlations and lattice distortions. *Phys. Rev. B* 75(24): 245112.
82. Naka, M. and H. Seo. 2014. Long-period charge correlations in charge-frustrated molecular θ-(BEDT-TTF)$_2$X. *J. Phys. Soc. Jpn.* 83(5): 053706.
83. Yoshimi, K., M. Naka, and H. Seo. 2020. Finite temperature properties of geometrically charge frustrated systems. *J. Phys. Soc. Jpn.* 89(3): 034003.
84. Yoshimi, K. and H. Maebashi. 2012. Coulomb frustrated phase separation in quasi-two-dimensional organic conductors on the verge of charge ordering. *J. Phys. Soc. Jpn.* 81(6): 063003.
85. Mahmoudian, S., L. Rademaker, A. Ralko, S. Fratini, and V. Dobrosavljević. 2015. Glassy dynamics in geometrically frustrated coulomb liquids without disorder. *Phys. Rev. Lett.* 115(2): 025701.
86. Sasaki, S., K. Hashimoto, R. Kobayashi, K. Itoh, S. Iguchi, Y. Nishio, Y. Ikemoto, T. Moriwaki, N. Yoneyama, M. Watanabe, A. Ueda, H. Mori, K. Kobayashi, R. Kumai, Y. Murakami, J. Müller, and T. Sasaki. 2017. Crystallization and vitrification of electrons in a glass-forming charge liquid. *Science* 357(6358): 1381.
87. Sato, T., K. Miyagawa, and K. Kanoda. 2017. Electronic crystal growth. *Science* 357(6358): 1378.
88. Mori, H., S. Tanaka, and T. Mori. 1998. Systematic study of the electronic state in θ-type BEDT-TTF organic conductors by changing the electronic correlation. *Phys. Rev. B* 57(19): 12023.
89. Mori, H., T. Okano, S. Tanaka, M. Tamura, Y. Nishio, K. Kajita, and T. Mori. 2000. Discontinuous change of metal-insulator transition in the alloyed θ-system: θ-(BEDT-TTF)$_2$(Rb$_{1-x}$Cs$_x$)Zn(SCN)$_4$. *J. Phys. Soc. Jpn.* 69(6): 1751.
90. Nakamura, T., W. Minagawa, R. Kinami, and T. Takahashi. 2000. Possible charge disproportionation and new type charge localization in θ-(BEDT-TTF)$_2$CsZn(SCN)$_4$. *J. Phys. Soc. Jpn.* 69(2): 504.
91. Miyagawa, K., A. Kawamoto, and K. Kanoda. 2000. Charge ordering in a quasi-two-dimensional organic conductor. *Phys. Rev. B* 62(12): R7679.
92. Chiba, R., K. Hiraki, T. Takahashi, H.M. Yamamoto, and T. Nakamura. 2008. Charge disproportionation and dynamics in θ-(BEDT-TTF)$_2$CsZn(SCN)$_4$. *Phys. Rev. B* 77(11): 115113.
93. Emmert, S., M. Wolf, R. Gulich, S. Krohns, S. Kastner, P. Lunkenheimer, and A. Loidl. 2011. Electrode polarization effects in broadband dielectric spectroscopy. *Eur. Phys. J. B* 83(2): 157.
94. Jonscher, A.K. 1983. *Dielectric relaxations in solids*. London: Chelsea Dielectrics Press.
95. Lunkenheimer, P., S. Krohns, S. Riegg, S.G. Ebbinghaus, A. Reller, and A. Loidl. 2010. Colossal dielectric constants in transition-metal oxides. *Eur. Phys. J. Spec. Top.* 180: 61.
96. Böhmer, R., M. Maglione, P. Lunkenheimer, and A. Loidl. 1989. Radio-frequency dielectric measurements at temperatures from 10 to 450 K. *J. Appl. Phys.* 65(3): 901.
97. Klein, O., S. Donovan, M. Dressel, and G. Grüner. 1993. Microwave cavity perturbation technique: part I: principles. *Int. J. Infrared Millimeter Waves* 14(12): 2423.
98. Schneider, U., P. Lunkenheimer, A. Pimenov, R. Brand, and A. Loidl. 2001. Wide range dielectric spectroscopy on glass-forming materials: an experimental overview. *Ferroelectrics* 249: 89.
99. Kremer, F.P. and A. Schönhals. 2002. Broadband dielectric measurement techniques. In *Broadband dielectric spectroscopy, chapter 2*, ed. F. Kremer and A. Schönhals. Berlin: Springer.
100. Scheffler, M. and M. Dressel. 2005. Broadband microwave spectroscopy in Corbino geometry for temperatures down to 1.7 K. *Rev. Sci. Instrum.* 76: 074702.
101. Scheffler, M., C. Fella, and M. Dressel. 2012. Stripline resonators for cryogenic microwave spectroscopy on metals and superconductors. *J. Phys. Conf. Ser.* 400(5): 052031.
102. Canossa, S., E. Ferrari, P. Sippel, J.K.H. Fischer, R. Pfattner, R. Frison, M. Masino, M. Mas-Torrent, P. Lunkenheimer, C. Rovira, and A. Girlando. 2021. Tetramethylbenzidine-tetrafluoroTCNQ (TMB-TCNQF$_4$): a narrow-gap semiconducting salt with room-temperature relaxor ferroelectric behavior. *J. Phys. Chem. C* 125(46): 25816.
103. Fischer, J.K.H., G. D'Avino, M. Masino, F. Mezzadri, P. Lunkenheimer, Z.G. Soos, and A. Girlando. 2021. Relaxor ferroelectricity in the polar M_2P-TCNQ charge-transfer crystal at the neutral-ionic interface. *Phys. Rev. B* 103(11): 115104.
104. D'Avino, G., M. Souto, M. Masino, J.K.H. Fischer, I. Ratera, X. Fontrodona, G. Giovannetti, M.J. Verstraete, A. Painelli, P. Lunkenheimer, J. Veciana, and A. Girlando. 2017. Conflicting evidence for ferroelectricity. *Nature* 547(7662): E9–E10.
105. Fischer, J.K.H., P. Lunkenheimer, C. Leva, S.M. Winter, M. Lang, C. Mézière, P. Batail, A. Loidl, and R.S. Manna. 2018. Relaxation dynamics in the one-dimensional organic charge-transfer salt δ-(EDT-TTF-CONMe$_2$)$_2$Br. *Phys. Rev. B* 97: 235156.
106. Lunkenheimer, P., V. Bobnar, A.V. Pronin, A.I. Ritus, A.A. Volkov, and A. Loidl. 2002. Origin of apparent colossal dielectric constants. *Phys. Rev. B* 66(5): 052105.
107. Thomas, T., Y. Agarmani, S. Hartmann, M. Kartsovnik, N. Kushch, S.M. Winter, S. Schmid, P. Lunkenheimer, M. Lang, and J. Müller. 2024. Slow and non-equilibrium dynamics due to electronic ferroelectricity in a strongly-correlated molecular conductor. *NPJ Spintronics* 2(1): 24.
108. Blinc, R. and B. Žekš. 1994. *Soft modes in ferroelectrics and antiferroelectrics*. Amsterdam: North-Holland.
109. Eric Cross, L. 1987. Relaxor ferroelectrics. *Ferroelectrics* 76(1): 241.
110. Samara, G.A. 2003. The relaxational properties of compositionally disordered ABO_3 perovskites. *J. Phys. Condens. Matter* 15(9): R367–R411.
111. Lines, M.E. and A.M. Glass. 2001. *Principles and applications of ferroelectrics and related materials*. Oxford: Oxford University Press.
112. Waser, R., U. Böttger, and S. Tiedke. 2005. *Polar oxides*, 1st edn. Hoboken: Wiley.

113. Krohns, S. and P. Lunkenheimer. 2019. Ferroelectric polarization in multiferroics. *Phys. Sci. Rev.* 4(9): 20190015.
114. Wiscons, R.A., N.R. Goud, J.T. Damron, and A.J. Matzger. 2018. Room-temperature ferroelectricity in an organic cocrystal. *Angew. Chem. Int. Ed.* 57(29): 9044.
115. Schrettle, F., S. Krohns, P. Lunkenheimer, J. Hemberger, N. Büttgen, H.-A. Krug von Nidda, A.V. Prokofiev, and A. Loidl. 2008. Switching the ferroelectric polarization in the S=1/2 chain cuprate $LiCuVO_4$ by external magnetic fields. *Phys. Rev. B* 77: 144101.
116. Lunkenheimer, P., B. Hartmann, M. Lang, J. Müller, D. Schweitzer, S. Krohns, and A. Loidl. 2015. Ferroelectric properties of charge-ordered α-(BEDT-TTF)$_2$I$_3$. *Phys. Rev. B* 91: 245132.
117. Bauer, T., M. Köhler, P. Lunkenheimer, A. Loidl, and C.A. Angell. 2010. Relaxation dynamics and ionic conductivity in a fragile plastic crystal. *J. Chem. Phys.* 133(14): 144509.
118. Kremer, F.P. and A. Schönhals. 2002. Analysis of dielectric spectra. In *Broadband dielectric spectroscopy, chapter 3*, ed. F. Kremer and A. Schönhals. Berlin: Springer.
119. Ediger, M.D. 2000. Spatially heterogeneous dynamics in supercooled liquids. *Annu. Rev. Phys. Chem.* 51: 99.
120. Lunkenheimer, P. and A. Loidl. 2018. *Glassy dynamics: from millihertz to terahertz*. Cham: Springer.
121. Lunkenheimer, P. and A. Loidl. 1996. Molecular reorientation in ortho-carborane studied by dielectric spectroscopy. *J. Chem. Phys.* 104(11): 4324.
122. Brand, R., P. Lunkenheimer, and A. Loidl. 2002. Relaxation dynamics in plastic crystals. *J. Chem. Phys.* 116: 10386.
123. Böttcher, C.J.F., O.C. van Belle, P. Bordewijk, A. Rip, and D.D. Yue. 1974. Theory of electric polarization. *J. Electrochem. Soc.* 121(6): 211C.
124. Wuttig, M., D. Viehland, and L.E. Cross. 1991. The glassy behavior of relaxor ferroelectrics. *Ferroelectrics* 120(1): 71.
125. Smolenskii, G.A., V.A. Isupov, A.I. Agranovskaya, and S.N. Popov. 1961. Ferroelectrics with diffuse phase transitions. *Sov. Phys. Solid State* 2(11): 2584.
126. Iguchi, S., S. Sasaki, N. Yoneyama, H. Taniguchi, T. Nishizaki, and T. Sasaki. 2013. Relaxor ferroelectricity induced by electron correlations in a molecular dimer Mott insulator. *Phys. Rev. B* 87(7): 075107.
127. Abdel-Jawad, M., I. Terasaki, T. Sasaki, N. Yoneyama, N. Kobayashi, Y. Uesu, and C. Hotta. 2010. Anomalous dielectric response in the dimer Mott insulator κ-(BEDT-TTF)$_2$Cu$_2$(CN)$_3$. *Phys. Rev. B* 82(12): 125119.
128. Matsui, H., H. Tsuchiya, T. Suzuki, E. Negishi, and N. Toyota. 2003. Relaxor ferroelectric behavior and collective modes in the π-d correlated anomalous metal λ-(BEDT-TSF)$_2$FeCl$_4$. *Phys. Rev. B* 68: 155105.
129. Viehland, D., S.J. Jang, L. Eric Cross, and M. Wuttig. 1990. Freezing of the polarization fluctuations in lead magnesium niobate relaxors. *J. Appl. Phys.* 68(6): 2916.
130. Levstik, A., Z. Kutnjak, C. Filipič, and R. Pirc. 1998. Glassy freezing in relaxor ferroelectric lead magnesium niobate. *Phys. Rev. B* 57(18): 11204.
131. Glazounov, A.E. and A.K. Tagantsev. 1998. Direct evidence for Vogel-Fulcher freezing in relaxor ferroelectrics. *Appl. Phys. Lett.* 73(6): 856.
132. Vogel, H. 1921. Das Temperaturabhängigkeitsgesetz der Viskositäten von Flüssigkeiten. *Z. Phys.* 22: 645.
133. Fulcher, G.S. 1925. Analysis of recent measurements of the viscosity of glasses. *J. Am. Ceram. Soc.* 8(6): 339.
134. Tammann, G. and W. Hesse. 1926. Die Abhängigkeit der Viscosität von der Temperatur bei unterkühlten Flüssigkeiten. *Zeitschrift für anorganische und allgemeine Chemie* 156(1): 245.
135. Lunkenheimer, P., U. Schneider, R. Brand, and A. Loid. 2000. Glassy dynamics. *Contemp. Phys.* 41(1): 15.
136. Ediger, M.D., C.A. Angell, and S.R. Nagel. 1996. Supercooled liquids and glasses. *J. Phys. Chem.* 100(31): 13200.
137. Scott, J.F. 2000. *Ferroelectric memories*. Berlin: Springer.
138. Loidl, A., S. Krohns, J. Hemberger, and P. Lunkenheimer. 2008. Bananas go paraelectric. *J. Phys. Condens. Matter* 20(19): 191001.
139. Müller, J., M. Lang, F. Steglich, J.A. Schlueter, A.M. Kini, and T. Sasaki. 2002. Evidence for structural and electronic instabilities at intermediate temperatures in κ-(BEDT-TTF)$_2$X for X=Cu[N(CN)$_2$]Cl, Cu[N(CN)$_2$]Br and Cu(NCS)$_2$: Implications for the phase diagram of these quasi-two-dimensional organic superconductors. *Phys. Rev. B* 65(14): 144521.
140. Müller, J., B. Hartmann, R. Rommel, J. Brandenburg, S.M. Winter, and J.A. Schlueter. 2015. Origin of the glass-like dynamics in molecular metals κ-(BEDT-TTF)$_2$X: implications from fluctuation spectroscopy and ab initio calculations. *New J. Phys.* 17(8): 083057.
141. Thomas, T., Y. Saito, Y. Agarmani, T. Thyzel, M. Lonsky, K. Hashimoto, T. Sasaki, M. Lang, and J. Müller. 2022. Involvement of structural dynamics in charge-glass formation in strongly frustrated molecular metals. *Phys. Rev. B* 105: L041114.
142. Müller, J. 2011. Fluctuation spectroscopy: a new approach for studying low-dimensional molecular metals. *ChemPhysChem* 12(7): 1222.
143. Müller, J. and T. Thomas. 2018. Low-frequency dynamics of strongly correlated electrons in (BEDT-TTF)$_2$X studied by fluctuation spectroscopy. *Crystals* 8: 166.
144. Kogan, S. 1996. *Electronic noise and fluctuations in solids*. Cambridge: Cambridge University Press.
145. Weissman, M.B. 1988. $1/f$ noise and other slow, nonexponential kinetics in condensed matter. *Rev. Mod. Phys.* 60(2): 537.
146. Raquet, B. 2001. *Spin electronics, chapter 11. Electronic noise in magnetic materials and devices*, 232. Berlin: Springer.
147. MacDonald, D.K.C. 1962. *Noise and fluctuations*. New York: Wiley.
148. Restle, P.J., M.B. Weissman, and R.D. Black. 1983. Tests of Gaussian statistical properties of $1/f$ noise. *J. Appl. Phys.* 54: 5844.
149. Seidler, G.T. and S.A. Solin. 1996. Non-Gaussian 1/f noise: experimental optimization and separation of high-order amplitude and phase correlations. *Phys. Rev. B* 53(15): 9753.
150. Weissman, M.B. 1993. What is a spin glass? A glimpse via mesoscopic noise. *Rev. Mod. Phys.* 65(3): 829.
151. Jaroszyński, J., D. Popović, and T.M. Klapwijk. 2002. Universal behavior of the resistance noise across the metal-insulator transition in silicon inversion layers. *Phys. Rev. Lett.* 89: 276401.
152. Jaroszyński, J., D. Popović, and T.M. Klapwijk. 2004. Magnetic-field dependence of the anomalous noise behavior in a two-dimensional electron system in silicon. *Phys. Rev. Lett.* 92(22): 226403.
153. Kar, S., A.K. Raychaudhuri, A. Ghosh, H.V. Löhneysen, and G. Weiss. 2003. Observation of non-Gaussian conductance fluctuations at low temperatures in Si:P(B) at the metal-insulator transition. *Phys. Rev. Lett.* 91: 216603.
154. Hartmann, B., D. Zielke, J. Polzin, T. Sasaki, and J. Müller. 2015. Critical slowing down of the charge carrier dynamics at the Mott metal-insulator transition. *Phys. Rev. Lett.* 114(21): 216403.
155. Thyzel, T., M. Kopp, J. Pieper, T. Stadler, and J. Müller. 2024. Methods in fluctuation (noise) spectroscopy and continuous analysis for high-throughput measurements. *Meas. Sci. Technol.* 36(1): 015501.

156. Raquet, B., J.M.D. Coey, S. Wirth, and S. von Molnár. 1999. $1/f$ noise in the half-metallic oxides CrO_2, Fe_3O_4, and $La_{2/3}Sr_{1/3}MnO_3$. *Phys. Rev. B* 59(19): 12435.
157. Müller, J., J. Brandenburg, and J.A. Schlueter. 2009. Magnetic-field induced crossover of superconducting percolation regimes in the layered organic Mott system κ-(BEDT-TTF)$_2$Cu[N(CN)$_2$]Cl. *Phys. Rev. Lett.* 102(4): 047004.
158. Pott, R. and R. Schefzyk. 1983. Apparatus for measuring the thermal expansion of solids between 1.5 and 380K. *J. Phys. E Sci. Instrum.* 16(5): 444.
159. Hartmann, S. 2022. *Thermische Ausdehnung an Materialien mit Hinweisen auf Spinflüssigkeitsverhalten und magnetischen Polaronen*. PhD thesis, Goethe-Universität Frankfurt am Main.
160. Matsuura, M., T. Sasaki, S. Iguchi, E. Gati, J. Müller, O. Stockert, A. Piovano, M. Böhm, J.T. Park, S. Biswas, S.M. Winter, R. Valentí, A. Nakao, and M. Lang. 2019. Lattice dynamics coupled to charge and spin degrees of freedom in the molecular Dimer-Mott insulator κ-(BEDT-TTF)$_2$Cu[N(CN)$_2$]Cl. *Phys. Rev. Lett.* 123: 027601.
161. Nad, F. and P. Monceau. 2006. Dielectric response of the charge ordered state in quasi-one-dimensional organic conductors. *J. Phys. Soc. Jpn.* 75(5): 051005.
162. Takahashi, T., Y. Nogami, and K. Yakushi. 2006. Charge ordering in organic conductors. *J. Phys. Soc. Jpn.* 75(5): 051008.
163. Chow, D.S., F. Zamborszky, B. Alavi, D.J. Tantillo, A. Baur, C.A. Merlic, and S.E. Brown. 2000. Charge ordering in the TMTTF family of molecular conductors. *Phys. Rev. Lett.* 85(8): 1698.
164. Matsunaga, N., S. Hirose, T. Satoh, T. Isome, Y. Yamomoto, M. Liu, A. Kawamoto, and K. Nomura. 2013. Charge ordering and antiferromagnetism in (TMTTF)$_2$SbF$_6$. *Phys. Rev. B* 87: 144415.
165. Dumm, M., B. Salameh, L.K. Montgomery, and M. Dressel. 2004. Magnetic and optical studies of spin and charge ordering in (TMTTF)$_2$AsF$_6$. *J. Phys. IV France* 114: 57.
166. Dressel, M., M. Dumm, T. Knoblauch, and M. Masino. 2012. Comprehensive optical investigations of charge order in organic chain compounds (TMTTF)$_2$X. *Crystals* 2(2): 528.
167. Starešinić, D., K. Biljaković, P. Lunkenheimer, and A. Loidl. 2006. Slowing down of the relaxational dynamics at the ferroelectric phase transition in one-dimensional (TMTTF)$_2$AsF$_6$. *Solid State Commun.* 137(5): 241–245.
168. de Souza, M., P. Foury-Leylekian, J.P. Pouget, and M. Lang. 2008. Evidence for lattice effects at the charge-ordering transition in (TMTTF)$_2$X. *Phys. Rev. Lett.* 101: 216403.
169. Seo, H. and H. Fukuyama. 1997. Antiferromagnetic phases of one-dimensional quarter-filled organic conductors. *J. Phys. Soc. Jpn.* 66(5): 1249.
170. Bender, K., I. Hennig, D. Schweitzer, K. Dietz, H. Endres, and H.J. Keller. 1984. Synthesis, structure and physical properties of a two-dimensional organic metal, di[bis(ethylenedithiolo)tetrathiofulvalene] triiodide, (BEDT-TTF)$_2$I$_3$. *Mol. Cryst. Liq. Cryst.* 108(3–4): 359.
171. Takano, Y., K. Hiraki, H.M. Yamamoto, T. Nakamura, and T. Takahashi. 2001. Charge disproportionation in the organic conductor, α-(BEDT-TTF)$_2$I$_3$. *J. Phys. Chem. Solids* 62(1–2): 393.
172. Kakiuchi, T., Y. Wakabayashi, H. Sawa, T. Takahashi, and T. Nakamura. 2007. Charge ordering in α-(BEDT-TTF)$_2$I$_3$ by synchrotron X-ray diffraction. *J. Phys. Soc. Jpn.* 76(11): 113702.
173. Yue, Y., K. Yamamoto, M. Uruichi, C. Nakano, K. Yakushi, S. Yamada, T. Hiejima, and A. Kawamoto. 2010. Nonuniform site-charge distribution and fluctuations of charge order in the metallic state of α-(BEDT-TTF)$_2$I$_3$. *Phys. Rev. B* 82(7): 075134.
174. Yamamoto, K., S. Iwai, S. Boyko, A. Kashiwazaki, F. Hiramatsu, C. Okabe, N. Nishi, and K. Yakushi. 2008. Strong optical nonlinearity and its ultrafast response associated with electron ferroelectricity in an organic conductor. *J. Phys. Soc. Jpn.* 77(7): 074709.
175. Yamamoto, K., A.A. Kowalska, and K. Yakushi. 2010. Direct observation of ferroelectric domains created by Wigner crystallization of electrons in α-[bis(ethylenedithio)tetrathiafulvalene]$_2$I$_3$. *Appl. Phys. Lett.* 96(12): 122901.
176. Ivek, T., B. Korin-Hamzić, O. Milat, S. Tomić, C. Clauss, N. Drichko, D. Schweitzer, and M. Dressel. 2010. Collective excitations in the charge-ordered phase of α-(BEDT-TTF)$_2$I$_3$. *Phys. Rev. Lett.* 104(20): 206406.
177. Ivek, T., B. Korin-Hamzić, O. Milat, S. Tomić, C. Clauss, N. Drichko, D. Schweitzer, and M. Dressel. 2011. Electrodynamic response of the charge ordering phase: dielectric and optical studies of α-(BEDT-TTF)$_2$I$_3$. *Phys. Rev. B* 83(16): 165128.
178. Kino, H. and H. Fukuyama. 1996. Phase diagram of two-dimensional organic conductors: (BEDT-TTF)$_2$X. *J. Phys. Soc. Jpn.* 65: 2158.
179. Senthil, T. 2008. Theory of a continuous Mott transition in two dimensions. *Phys. Rev. B* 78(4): 045109.
180. Chiba, R., H. Yamamoto, K. Hiraki, T. Takahashi, and T. Nakamura. 2001. Charge disproportionation in (BEDT-TTF)$_2$RbZn(SCN)$_4$. *J. Phys. Chem. Solids* 62(1–2): 389.
181. Alemany, P., J.-P. Pouget, and E. Canadell. 2015. Structural and electronic control of the metal to insulator transition and local orderings in the θ-(BEDT-TTF)$_2$X organic conductors. *J. Phys. Condens. Matter* 27(46): 465702.
182. Hashimoto, K., R. Kobayashi, S. Ohkura, S. Sasaki, N. Yoneyama, M. Suda, H.M. Yamamoto, and T. Sasaki. 2022. Optical conductivity spectra of charge-crystal and charge-glass states in a series of θ-Type BEDT-TTF compounds. *Crystals* 12: 831.
183. Saito, Y., O. Ganter, K. Hashimoto, T. Sasaki, S.M. Winter, J. Müller, and M. Lang. 2024. Combined experimental and theoretical studies on glasslike transitions in the frustrated molecular conductors θ-(BEDT-TTF)$_2$MM'(SCN)$_4$. *Phys. Rev. Res.* 6(2): 023003.
184. Kagawa, F., T. Sato, K. Miyagawa, K. Kanoda, Y. Tokura, K. Kobayashi, R. Kumai, and Y. Murakami. 2013. Charge-cluster glass in an organic conductor. *Nat. Phys.* 9(7): 419.
185. Nad, F., P. Monceau, and H.M. Yamamoto. 2006. Dielectric response in the charge-ordered θ-(BEDT-TTF)$_2$RbZn(SCN)$_4$ organic compound. *J. Phys. Condens. Matter* 18(41): L509.
186. Takahashi, T., R. Chiba, K. Hiraki, H.M. Yamamota, and T. Nakamura. 2004. Dynamical charge disproportionation in metallic state in θ-(BEDT-TTF)$_2$RbZn(SCN)$_4$. *J. Phys. IV France* 114: 269.
187. Bokov, A.A. and Z.G. Ye. 2006. Recent progress in relaxor ferroelectrics with perovskite structure. *J. Mater. Sci.* 1: 31.
188. Yoneyama, N., A. Miyazaki, T. Enoki, and G. Saito. 1999. Magnetic properties of TTF-type charge transfer salts in the Mott insulator regime. *Bull. Chem. Soc. Jpn.* 72(4): 639.
189. Hattori, Y., S. Iguchi, T. Sasaki, S. Iwai, H. Taniguchi, and H. Kishida. 2017. Electric-field-induced intradimer charge disproportionation in the Dimer-Mott insulator β'- (BEDT-TTF)$_2$ICl$_2$. *Phys. Rev. B* 95: 085149.
190. Müller, J., S. Iguchi, H. Taniguchi, and T. Sasaki. 2020. Formation of nanoscale polarized clusters as precursors of electronic ferroelectricity probed by conductance noise spectroscopy. *Phys. Rev. B* 102: 100103.
191. Raquet, B., A. Anane, S. Wirth, P. Xiong, and S. von Molnár. 2000. Noise probe of the dynamic phase separation in $La_{2/3}Ca_{1/3}MnO_3$. *Phys. Rev. Lett.* 84(19): 4485.
192. Hashimoto, K., R. Kobayashi, H. Okamura, H. Taniguchi, Y. Ikemoto, T. Moriwaki, S. Iguchi, M. Naka, S. Ishihara, and T. Sasaki. 2015. Emergence of charge degrees of freedom under

high pressure in the organic dimer-Mott insulator β'-(BEDT-TTF)$_2$ICl$_2$. *Phys. Rev. B* 92(8): 174527.
193. Tajima, N., R. Kato, and H. Taniguchi. 2008. Transport properties of an organic Mott insulator β'-(BEDT-TTF)$_2$ICl$_2$. *EPL (Europhys. Lett.)* 83(2): 27008.
194. Shklovskii, B.I. 2003. $1/f$ noise in variable range hopping conduction. *Phys. Rev. B* 67(4): 045201.
195. Burin, A.L., B.I. Shklovskii, V.I. Kozub, Y.M. Galperin, and V. Vinokur. 2006. Many electron theory of 1/f noise in hopping conductivity. *Phys. Rev. B* 74(7): 075205.
196. Stauffer, D. and A. Aharony. 1994. *Introduction to percolation theory*. Revised 2. London: Taylor and Francis.
197. Abdel-Jawad, M., N. Tajima, R. Kato, and I. Terasaki. 2013. Disordered conduction in single-crystalline dimer Mott compounds. *Phys. Rev. B* 88(7): 075139.
198. Tamura, M. and R. Kato. 2009. Variety of valence bond states formed of frustrated spins on triangular lattices based on a two-level system Pd(dmit)$_2$. *Sci. Technol. Adv. Mater.* 10(2): 024304 ((**PMID: 27877277**)).
199. Watanabe, K., H. Kawamura, H. Nakano, and T. Sakai. 2014. Quantum spin-liquid behavior in the spin-1/2 random Heisenberg antiferromagnet on the triangular lattice. *J. Phys. Soc. Jpn.* 83(3): 034714.
200. Kino, H. and H. Fukuyama. 1995. Electronic states of conducting organic κ-(BEDT-TTF)$_2$X. *J. Phys. Soc. Jpn.* 64(8): 2726.
201. Aldoshina, M.Z., R.N. Lyubovskaya, S.V. Konovalikhin, O.A. Dyachenko, M.K. Makova, and R.B. Lyubovskii. 1993. New Organic Metals (ET)$_2$[Hg(SCN)Cl$_2$] and (ET)$_2$[Hg(SCN)$_2$Cl]. *Mol. Cryst. Liq. Cryst. Sci. Technol. Sect. A Mol. Cryst. Liq. Cryst.* 230(1): 185.
202. Yasin, S., D. Rose, M. Dumm, N. Drichko, M. Dressel, J.A. Schlueter, E.I. Zhilyaeva, S. Torunova, and R.N. Lyubovskaya. 2012. Electronic and magnetic studies of κ-(BEDT-TTF)$_2$Hg(SCN)$_2$Cl. *Physica B* 407: 1689.
203. Drichko, N., R. Beyer, E. Rose, M. Dressel, J.A. Schlueter, S.A. Turunova, E.I. Zhilyaeva, and R.N. Lyubovskaya. 2014. Metallic state and charge-order metal-insulator transition in the quasi-two-dimensional conductor κ-(BEDT-TTF)$_2$Hg(SCN)$_2$Cl. *Phys. Rev. B* 89: 075133.
204. Yamamoto, T., M. Uruichi, K. Yamamoto, K. Yakushi, A. Kawamoto, and H. Taniguchi. 2005. Examination of the charge-sensitive vibrational modes in bis(ethylenedithio)tetrathiafulvalene. *J. Phys. Chem. B* 109(32): 15226.
205. Mason, W.P. and B.T. Matthias. 1948. Theoretical model for explaining the ferroelectric effect in barium titanate. *Phys. Rev.* 74(11): 1622.
206. Ivek, T., R. Beyer, S. Badalov, M. Čulo, S. Tomić, J.A. Schlueter, E.I. Zhilyaeva, R.N. Lyubovskaya, and M. Dressel. 2017. Metal-insulator transition in the dimerized organic conductor κ-(BEDT-TTF)$_2$Hg(SCN)$_2$Br. *Phys. Rev. B* 96(8): 085116.
207. Hassan, N., S. Cunningham, M. Mourigal, E.I. Zhilyaeva, S.A. Torunova, R.N. Lyubovskaya, J.A. Schlueter, and N. Drichko. 2018. Evidence for a quantum dipole liquid state in an organic quasitwo-dimensional material. *Science* 360(6393): 1101.
208. Yamashita, M., S. Sugiura, A. Ueda, S. Dekura, T. Terashima, S. Uji, Y. Sunairi, H. Mori, E.I. Zhilyaeva, S.A. Torunova, R.N. Lyubovskaya, N. Drichko, and C. Hotta. 2021. Ferromagnetism out of charge fluctuation of strongly correlated electrons in κ-(BEDT-TTF)$_2$Hg(SCN)$_2$Br. *NPJ Quantum Mater.* 6(1): 87.
209. Thomas, T., B. Hartmann, P. Lunkenheimer, H. Schubert, J.A. Schlueter, and J. Müller. 2019. Low-frequency charge carrier dynamics in ferroelectric κ-(BEDT-TTF)$_2$X - a comparative study of X = Cu[N(CN)$_2$]Cl and X = Hg(SCN)$_2$Cl. *Physica status solidi (b)* 256(9): 1800746.
210. Jeschke, H.O., M. de Souza, R. Valentí, R.S. Manna, M. Lang, and J.A. Schlueter. 2012. Temperature dependence of structural and electronic properties of the spin-liquid candidate κ-(BEDT-TTF)$_2$Cu$_2$(CN)$_3$. *Phys. Rev. B* 85(3): 035125.
211. Miksch, B., A. Pustogow, M.J. Rahim, A.A. Bardin, K. Kanoda, J.A. Schlueter, R. Hübner, M. Scheffler, and M. Dressel. 2021. Gapped magnetic ground state in quantum spin liquid candidate κ-(BEDT-TTF)$_2$Cu$_2$(CN)$_3$. *Science* 372(6539): 276.
212. Pustogow, A. 2022. Thirty-year anniversary of κ-(BEDT-TTF)$_2$Cu$_2$(CN)$_3$: reconciling the spin gap in a spin-liquid candidate. *Solids* 3(1): 93.
213. Pinterič, M., M. Čulo, O. Milat, M. Basletič, B. Korin-Hamzič, E. Tafra, A. Hamzič, T. Ivek, T. Peterseim, and K. Miyagawa. 2014. Anisotropic charge dynamics in the quantum spin-liquid candidate κ-(BEDT-TTF)$_2$Cu$_2$(CN)$_3$. *Phys. Rev. B* 90(19): 195139.
214. Manna, R.S., M. de Souza, A. Brühl, J.A. Schlueter, and M. Lang. 2010. Lattice effects and entropy release at the low-temperature phase transition in the spin-liquid candidate κ-(BEDT-TTF)$_2$Cu$_2$(CN)$_3$. *Phys. Rev. Lett.* 104(1): 016403.
215. Manna, R., S. Hartmann, E. Gati, J. Schlueter, M. de Souza, and M. Lang. 2018. Low-temperature lattice effects in the spin-liquid candidate κ-(BEDT-TTF)$_2$Cu$_2$(CN)$_3$. *Crystals* 8: 87.
216. Clay, R.T., H. Li, and S. Mazumdar. 2010. Bipolaron density-wave driven by antiferromagnetic correlations and frustration in organic superconductors. *Physica B* 405(11): S253.
217. Gomi, H., M. Ikenaga, Y. Hiragi, D. Segawa, A. Takahashi, T.J. Inagaki, and M. Aihara. 2013. Ferroelectric states induced by dimer lattice disorder in dimer Mott insulators. *Phys. Rev. B* 87(19): 195126.
218. Sedlmeier, K., S. Elsässer, D. Neubauer, R. Beyer, D. Wu, T. Ivek, S. Tomic, J.A. Schlueter, and M. Dressel. 2012. Absence of charge order in the dimerized κ-phase BEDT-TTF salts. *Phys. Rev. B* 86(24): 245103.
219. Yakushi, K., K. Yamamoto, T. Yamamoto, Y. Saito, and A. Kawamoto. 2015. Raman spectroscopy study of charge fluctuation in the spin-liquid candidate κ-(BEDT-TTF)$_2$Cu$_2$(CN)$_3$. *J. Phys. Soc. Jpn.* 84(8): 084711.
220. Matsuura, M., T. Sasaki, M. Naka, J. Müller, O. Stockert, A. Piovano, N. Yoneyama, and M. Lang. 2022. Phonon renormalization effects accompanying the 6 K anomaly in the quantum spin liquid candidate κ-(BEDT-TTF)$_2$Cu$_2$(CN)$_3$. *Phys. Rev. Res.* 4(4): l042047.
221. Dressel, M., P. Lazić, A. Pustogow, E. Zhukova, B. Gorshunov, J. A. Schlueter, O. Milat, B. Gumhalter, and S. Tomić. 2016. Lattice vibrations of the charge-transfer salt κ-(BEDT-TTF)$_2$Cu$_2$(CN)$_3$: Comprehensive explanation of the electrodynamic response in a spin-liquid compound. *Phys. Rev. B*, 93(8).
222. Hartmann, B. 2017. *Ladungsträgerdynamik am Mott-Übergang*. PhD thesis, Goethe-Universität Frankfurt am Main.
223. Pinterić, M., M. Miljak, N. Biškup, O. Milat, I. Aviani, S. Tomić, D. Schweitzer, W. Strunz, and I. Heinen. 1999. Magnetic anisotropy and low-frequency dielectric response of weak ferromagnetic phase in κ-(BEDT-TTF)$_2$Cu[N(CN)$_2$]Cl, where BEDT-TTF is Bis(ethylenedithio)tetrathiafulvalene. *Eur. Phys. J. B* 11(2): 217.
224. Tomić, S., M. Pinterić, T. Ivek, K. Sedlmeier, R. Beyer, D. Wu, J.A. Schlueter, D. Schweitzer, and M. Dressel. 2013. Magnetic ordering and charge dynamics in κ-(BEDT-TTF)$_2$Cu[N(CN)$_2$]-Cl. *J. Phys. Condens. Matter* 25(43): 436004.
225. Pinterić, M., T. Ivek, M. Čulo, O. Milat, M. Basletić, B. Korin-Hamzić, E. Tafra, A. Hamzić, M. Dressel, and S. Tomić. 2015. What is the origin of anomalous dielectric response in 2D organic dimer Mott insulators κ-(BEDT-TTF)$_2$Cu[N(CN)$_2$]Cl and κ-(BEDT-TTF)$_2$Cu$_2$(CN)$_3$. *Physica B* 460: 202.

226. Kornelsen, K., J.E. Eldridge, H.H. Wang, H.A. Charlier, and J.M. Williams. 1992. Infrared study of the metal-insulator transition in the organic conductor κ-(BEDT-TTF)$_2$Cu[N(CN)$_2$]Cl. *Solid State Commun.* 81: 343.
227. Sasaki, T., I. Ito, N. Yoneyama, N. Kobayashi, N. Hanasaki, H. Tajima, T. Ito, and Y. Iwasa. 2004. Electronic correlation in the infrared optical properties of the quasi-two-dimensional κ-type BEDT-TTF dimer system. *Phys. Rev. B* 69(6): 064508.
228. Vyaselev, O.M., W. Biberacher, N.D. Kushch, and M.V. Kartsovnik. 2017. Interplay between the *d*- and π-electron systems in magnetic torque of the layered organic conductor κ-(BETS)$_2$Mn[N(CN)$_2$]$_3$. *Phys. Rev. B* 96: 205154.
229. Kartsovnik, M.V., V.N. Zverev, W. Biberacher, S.V. Simonov, I. Sheikin, N.D. Kushch, and E.B. Yagubskii. 2017. Shubnikov-de Haas oscillations and electronic correlations in the layered organic metal κ-(BETS)$_2$Mn[N(CN)$_2$]$_3$. *Low Temp. Phys.* 43(2): 239–243.
230. Vyaselev, O.M., R. Kato, H.M. Yamamoto, M. Kobayashi, L.V. Zorina, S.V. Simonov, N.D. Kushch, and E.B. Yagubskii. 2012. Properties of Mn^{2+} and π-Electron Spin Systems Probed by ^{1}H and ^{13}C NMR in the Organic Conductor κ-(BETS)$_2$Mn[N(CN)$_2$]$_3$. *Crystals* 2: 224.
231. Zverev, V.N., M.V. Kartsovnik, W. Biberacher, S.S. Khasanov, R.P. Shibaeva, L. Ouahab, L. Toupet, N.D. Kushch, E.B. Yagubskii, and E. Canadell. 2010. Temperature-pressure phase diagram and electronic properties of the organic metal κ-(BETS)$_2$Mn[N(CN)$_2$]$_3$. *Phys. Rev. B* 82: 155123.
232. Zverev, V.N., W. Biberacher, S. Oberbauer, I. Sheikin, P. Alemany, E. Canadell, and M.V. Kartsovnik. 2019. FFermi surface properties of the bifunctional organic metal κ-(BETS)$_2$Mn[N(CN)$_2$]$_3$ near the metal-insulator transition. *Phys. Rev. B* 99: 125136.
233. Lunkenheimer, P., S. Krohns, S. Riegg, S.G. Ebbinghaus, A. Reller, and A. Loidl. 2009. Colossal dielectric constants in transition-metal oxides. *Eur. Phys. J. Spec. Top.* 180(1): 61.
234. Bobnar, V., P. Lunkenheimer, M. Paraskevopoulos, and A. Loidl. 2002. Separation of grain boundary effects and intrinsic properties in perovskite-like $Gd_{0.6}Y_{0.4}BaCo_2O_{5.5}$ using high-frequency dielectric spectroscopy. *Phys. Rev. B* 65(18): 184403.
235. Kushch, N.D., E.B. Yagubskii, M.V. Kartsovnik, L.I. Buravov, A.D. Dubrovskii, A.N. Chekhlov, and W. Biberacher. 2008. π-Donor BETS Based bifunctional superconductor with polymeric dicyanamidomanganate(II) anion layer: κ-(BETS)$_2$Mn[N(CN)$_2$]$_3$. *J. Am. Chem. Soc.* 130(23): 7238.
236. Vyaselev, O.M., M.V. Kartsovnik, N.D. Kushch, and E.B. Yagubskii. 2012. Staggered spin order of localized π-electrons in the insulating state of the organic conductor κ-(BETS)$_2$Mn[N(CN)$_2$]$_3$. *JETP Lett.* 95: 565.
237. Schmidt, M., S. Priya, Z. Huang, M. Kartsovnik, N. Kushch, and M. Dressel. 2024. Electronic properties of the dimerized organic conductor κ-(BETS)$_2$Mn[N(CN)$_2$]$_3$.
238. Guangyong, X., G. Shirane, J.R.D. Copley, and P.M. Gehring. 2004. Neutron elastic diffuse scattering study of Pb($Mg_{1/3}Nb_{2/3}$)O_3. *Phys. Rev. B* 69: 064112.
239. Fu, D., H. Taniguchi, M. Itoh, S.Y. Koshihara, N. Yamamoto, and S. Mori. 2009. Relaxor Pb($Mg_{1/3}Nb_{2/3}$)O_3: a ferroelectric with multiple inhomogeneities. *Phys. Rev. Lett.* 103(20): 207601.
240. Thurn, C., P. Eibisch, A. Ata, M. Winkler, P. Lunkenheimer, I. Kézsmárki, U. Tutsch, Y. Saito, S. Hartmann, J. Zimmermann, R.N. Abanoub, A.T.M. Hanna, N. Islam, S. Chillal, B. Lake, B. Wolf, and M. Lang. 2021. Spin liquid and ferroelectricity close to a quantum critical point in $PbCuTe_2O_6$. *NPJ Quantum Mater.* 6(1): 95.
241. Vugmeister, B.E. 2006. Polarization dynamics and formation of polar nanoregions in relaxor ferroelectrics. *Phys. Rev. B* 73: 174117.
242. Glazounov, A.E. and A.K. Tagantsev. 1999. A breathing model for the polarization response of relaxor ferroelectrics. *Ferroelectrics* 221(1): 57.
243. Bogdanovich, S. and D. Popović. 2002. Onset of glassy dynamics in a two-dimensional electron system in silicon. *Phys. Rev. Lett.* 88(23): 236401.
244. Ward, T.Z., X.G. Zhang, L.F. Yin, X.Q. Zhang, P.C. Ming Liu, S. Snijders, E.W. Jesse, Z.H. Plummer, E.D. Cheng, and J. Shen. 2009. Time-resolved electronic phase transitions in manganites. *Phys. Rev. Lett.* 102: 087201.
245. Weissman, M.B., N.E. Israeloff, and G.B. Alers. 1992. Spin-glass fluctuation statistics: mesoscopic experiments in Mn. *J. Magn. Magn. Mater.* 114(1–2): 87.
246. Yu, C.C. 2004. Why study 1/f noise in Coulomb glasses. *Physica Status Solidi C Curr. Top.* 1: 25–28.
247. Yu, C.C. 2004. Why study noise due to two level systems: a suggestion for experimentalists. *J. Low Temp. Phys.* 137: 251–265.
248. Chen, Z. and Yu. Clare. 2007. Measurement-noise maximum as a signature of a phase transition. *Phys. Rev. Lett.* 98: 057204.
249. Daptary, G.N., M. Siddharth Kumar, J. Chakhalian, A.B. Kareev, and S. Middey. 2019. Conductivity noise across temperature-driven transitions of rare-earth nickelate heterostructures. *Phys. Rev. B* 100: 125105.